Fabrication and optical characterization of long-range plasmonic waveguide interconnects for Tb/s datacom links

Christian Vernoux

UNIVERSITÉ DE BOURGOGNE - FRANCHE COMTE

FACULTÉ DES SCIENCES

LABORATOIRE INTERDISCIPLINAIRE CARNOT DE BOURGOGNE

Département Nanociences

T H È S E

pour obtenir le titre de

Docteur en Sciences

Mention : Physique

Fabrication and optical characterization of long-range plasmonic waveguide interconnects for Tb/s datacom links

Présentée par

Christian VERNOUX

Thèse dirigée par Alain DEREUX et Laurent MARKEY

préparée au sein du Laboratoire Interdisciplinaire Carnot de Bourgogne,
Projet PHOXTROT

défendue le 30 Janvier 2019 devant la commission d'examen composée de:.

LETARTRE	X.	Directeur de Recherche, INL, Lyon	*Rapporteur*
DAGENS	B.	Directrice de Recherche, C2N, Saclay	*Rapporteur*
BAUDRION-BEAL	A.-L.	Maitre de conférence, UTT, Troyes	*Examinateur*
HAMMANI	K.	Maitre de conférence, UBFC, Dijon	*Examinateur*
DEREUX	A.	Professeur, UBFC, Dijon	*Directeur de thèse*
MARKEY	L.	Ingénieur de Recherche, UBFC, Dijon	*Co-encadrant de thèse*

I fear the day that technology will surpass our human interaction.
The world will have a generation of idiots.
Albert Einstein

Remerciements

Ce travail de thèse, financé par le projet européen "PhoXIroT", a été réalisé au sein de l'équipe d'Optique Submicronique et Nanocapteurs (OSNC) du laboratoire Interdisciplinaire Carnot de Bourgogne.

Je remercie tout particulièrement le Professeur Alain Dereux, pour avoir accepté de supervisé cette thèse, ainsi que pour ses diverses remarques judicieuses effectuées durant la correction de cette thèse.
Je tiens aussi à remercier très chaleureusement Laurent Markey, pour m'avoir apporté sa très GRANDE science des polymères, ainsi que de m'avoir fait confiance pendant toutes ces années et sans qui, ce travail n'aurait jamais pu voir le jour. Ses compétences, sa motivation, sa rigueur irréprochable et pour l'aide de proximité apportée dans la réalisation de ce travail ainsi que les discussions constructives que nous avons eues.

Je voudrais ensuite exprimer toute ma gratitude envers madame Béatrice Dagens et monsieur Xavier Letartre qui ont accepté la tâche d'être rapporteurs de cette thèse et dont leurs reconnaissances est un honneur. Je tiens aussi à remercier madame Anne-Laure Baudrion-Béal ainsi que monsieur Kamal Hammani qui ont accepté d'examiner mon travail et d'être présents dans mon jury.

Je souhaite remercier chaleureusement Juan-Miguel Arocas-Garcia, pour m'avoir fait partagé son expérience dans le domaine des dépôts sous vide, et pour toutes les discussions autour du café du matin. Ainsi que Jean Claude Weeber de m'avoir apporté sa très grande expérience pour la conception ainsi que pour les mesures sur le banc optique
Mes remerciements les plus amicaux vont à Gérard Colas des Francs, Kamal Hammani, Aymeric Leray, Eric Finot, Eric Lesniewska avec qui ce fut un plaisir de partager un café ou repas durant ces trois années.

Je tiens particulièrement à remercier deux personnes, Thibault Brulé, avec qui j'ai partagé plus d'un bon moment autour de notre café matinal ou d'un repas, et Andréea-Maria Crisbăşan, qui avec cette question récurrente, « quand est-ce que tu la soutiens cette thèse ? », bien qu'angoissante en période fréquente de doutes, m'ont permis de ne jamais dévier de mon objectif final.

Je tiens à saluer chaleureusement « les jeunes » qui ont occupé les postes de thésards, stagiaires ou post-doctorant lors de ma thèse au sein du laboratoire : Floriane Leroy, Delphine Sicard, Anthonin Ollagnier, Simon Debrand, Thomas Bernardin, Karim Hassan, Serkan Kaya, Ece Aybeke, Mickael Buret, Marie-Maxime Mennemanteuil, Jean-Emmanuel Clément, Régis Méjard, Sveltlana Viarbitskaya, Nicolas Cazier, Stéphane Derom.

Je voudrais aussi remercier les différents stagiaires que j'ai pu côtoyer, sur lesquelles j'ai pu exercer mes « talents » de professeur, et qui ont participé à cette thèse : Thomas Racine, Alexandre Deramecourt, et Nicolae-Cosmin Sparchez
Ainsi que les membres du consortium réunis au sein du projet « PhoXIroT »
Et pour finir, je remercie mes proches qui m'ont soutenu avant, pendant et qui continueront après cette thèse. Je remercie plus particulièrement : ma très précieuse maman, qui a toujours su me réconforter ses 10 dernières années, et sans qui je n'aurais jamais réussi à arriver là où je suis aujourd'hui.

Enfin, je voudrais remercier toutes les personnes que je n'ai pas citées par oubli. Qu'elles trouvent ici toute ma reconnaissance, qu'elles trouvent ici toute ma reconnaissance, ainsi que tous les membres du laboratoire pour leur accueil et leur gentillesse.

Contents

List of Figures

List of Tables

Abbreviations

ω	Width of waveguide
BOE	Buffered oxide etchant
DL-SPP	Dielectric-loaded surface plasmon-polariton
EIM	Effective index method
FEM	Finite element method
FSOI	Free-space optical interconnects
FWHM	Full width at half maximum
IP	Integrating project
$\mathbf{L}_{prop}$	Propagation length
LR-SPP	Long-range surface plasmon polariton
LR-SPPW	Long-range Surface plasmon polariton waveguide
MLA	MicroLens-Arrays
NMP	N-methyl pyrrolidone
oPCB	Optical printed circuit board
PGMEA	Propylene glycol methyl ether acetate
PWB	Photonic wire bond
RIE	Reactive-ion etching
SIP	System in packages
SM	Single mode
SPP	Surface plasmon polariton
t	Thickness of waveguide
$\mathbf{t}_{th}$	Threshold thickness
TE	Transverse electric
TIR	Total internal reflection
TM	Transverse magnetic

ULR-SPP ..... Ultra long-range surface plasmon polariton

VCSEL ..... Vertical cavity surface emitting laser

Chapter 0

General introduction

This work received financial support from the European project : **"PhoxTroT"**, which is the abbreviation of "Photonics for High-Performance, Low-Cost and Low- Energy Data Centers and High Performance Computing Systems: Terabit/s Optical Interconnect Technologies for On-Board, Board-to-Board and Rack-to-Rack data links [2]. This work was realized in the Laboratoire Interdisciplinaire Carnot de Bourgogne (**ICB**), jointly operated by Centre National de la Recherche Scientifique (**CNRS**) and Université de Bourgogne (**UB**). PhoxTroT is a large-scale integrating project (IP) accepted in Europe's ICT Call 8 [FP7-ICT-2011-8]

The European Project "**PhoxTroT**" is a large-scale European research effort focusing on high-performance, low energy, low cost and small size optical interconnects across the different hierarchy levels in data center and high-performance computing systems: on-board, board-to-board and rack-to-rack. This project is tackling optical interconnects in a holistic way, synergizing the different fabrication platforms in order to deploy the optimal "mix & match" technology and tailor this to each interconnect layer.

The PhoxTroT consortium regroups 20 European partners in 11 different countries:

- Fraunhofer-**I**nstitut für **Z**uverlässigkeit und **M**ikrointegration (**IZM**) (Germany)
- Fraunhofer-Institut für Nachrichtentechnik, **H**einrich-**H**ertz-**I**nstitut (**HHI**) (Germany)
- Vertilas GmbH (Germany)
- Xyratex Technology Ltd. (United Kingdom)
- **A**ustria **M**ikro **S**ysteme (**AMS**) (Austria)
- **TTM** Technologies, Inc. (Finland)
- **A**utomatisierung **M**esstechnik **O**ptik GmbH (**AMO**) (Germany)
- **I**nstitute of **C**ommunications & **C**omputer **S**ystems and **N**ational **T**echnical **U**niversity of **A**thens (**ICCS/NTUA**) (Greece)
- **DAS** Photonics SL (Spain)
- **Phoenix** BV (The Netherlands)
- **Ce**ntre for **R**esearch and **T**echnology **H**ellas / **I**nformatics and **T**elematics **I**nstitute (**CERTH-ITI**) (Greece)

- Compass **E**lectro **O**ptical **S**ystems Ltd. (**Compass EOS**) (Israel)
- Bright Photonics BV (The Netherlands)
- **C**omputer **T**echnology **I**nstitute and Press "Diophantus" (**CTI**) (Greece)
- **C**entre **N**ational de **R**echerche **S**cientifique - **L**aboratoire de **P**hotonique et de **N**anostructures (**CNRS-LPN**) (France)
- **C**entre **N**ational de **R**echerche **S**cientifique - **U**niversité de **B**ourgogne (**CNRS-UB**) (France)
- **K**arlsruher **I**nstitut für **T**echnologie (**KIT**) (Germany)
- **S**yddansk **D**enmark **U**niversity (**SDU**) (Denmark)
- **U**niversity **P**olitecnica **V**alencia (**UPV**) (Spain)
- **I**nteruniversitair **M**icro-**E**lektronica **C**entrum (**IMEC**) (Belgium)
- **T**yco **E**lectronics **Connectivity** (The Netherlands)

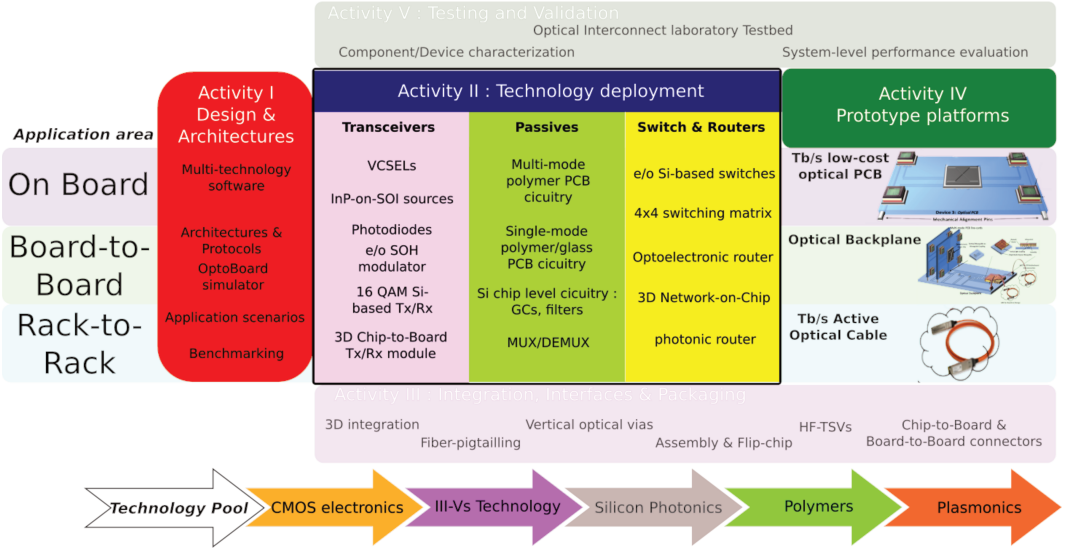

Figure 0.1 *– Various activities within the PhoxTroT project.*

One main objective of the "PhoxTroT" project is the deployment of generic building blocks that can be used for a broad range of applications, as extending performance beyond terabits per second and reducing energy by more than 50 %. Another objective would be an unified integration/packaging methodology as a cost/energy-reduction factor for board-adaptable 3D System in Packages (**SIP**) transceiver and router optochip fabrication.

Figure 0.2 shows the operating speeds and critical dimensions of different chip-scale device technologies, and it presents the plasmonic devices as a good compromise between a very small device and high transfer rate for the data communication broadband between components. The plasmonics devices are the next generation for coupling of light to charges like electrons in metals, and allow breaking the diffraction limit for the localization of light into sub-wavelength dimensions enabling strong field enhancements (Figure 0.2).

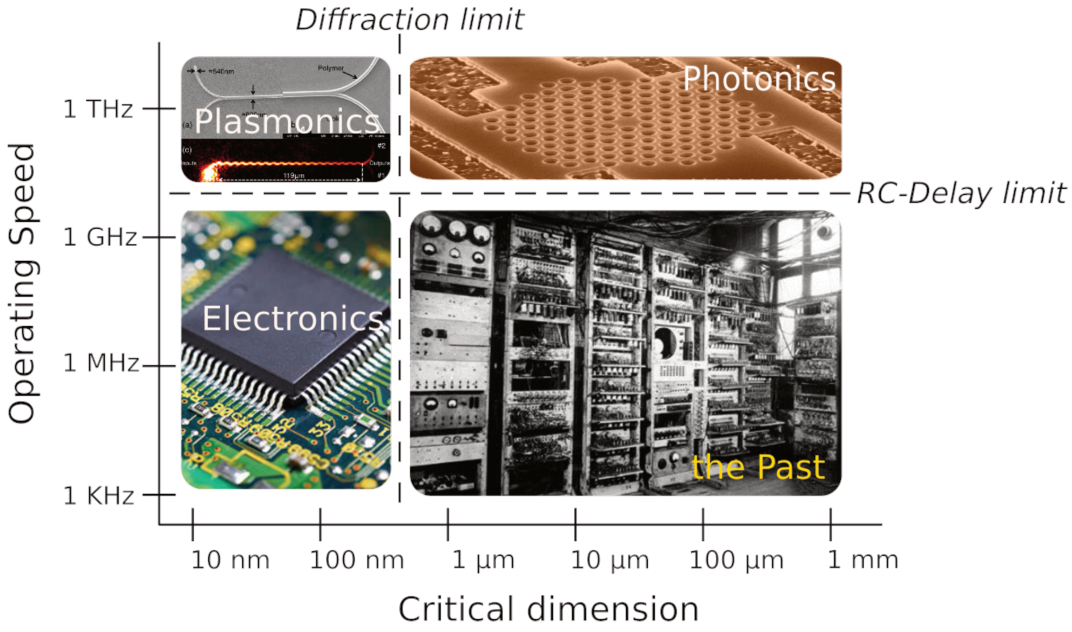

Figure 0.2 – *Operating speeds and critical dimensions of various chip-scale device technologies, highlighting the strengths of the different technologies. (Adapted from [3])*

This technology is already in development in different research fields including, nonlinear plasmonics [4], plasmons on graphene [5] and biosensor applications [6], with different materials [7].

The PhoxTroT workplan is divided in five major activity areas as shown in Figure 0.1. The first demonstrator is based on the multi-mode technology concept, where the optical interconnexion is realized by a micro-component inserted inside the optical Printed Circuit Board (**oPCB**). The wavelength range of the multi-mode interconnexions is situated in the near and middle infra-red range ($0.8\ \mu m < \lambda < 2.5\ \mu$m). The multi-mode waveguide shows a limit for a complex signal or very fast communications. A second demonstrator, also without plasmonic elements, is being developed but it is designed to work in single-mode communication. At last, PhoxTroT aimed to develop a single-mode platform integrating plasmonic interfaces. The task of the University of Burgundy was devoted to the development of new concepts of interconnects based on plasmonics.

The first PhoxTroT demonstrator is mostly an assembly of known technological building blocks, in particular in the field of on-board interconnexion by coupling in multi-mode optical PCBs based on dual-MicroLens-Arrays (**MLA**) with Vertical-cavity surface-emitting laser (**VCSEL**) or photodiode (shown in Figure 0.5a). Oppositely, the plasmonics task of the project is still at the research level, therefore more disruptive and more risky. Its first objective was to develop long-range plasmonic waveguides for broadband optical interconnections. This also corresponds to the objective of this thesis. In more details, the plasmonics task, which belongs to Activity II, "Passives" (Figure 0.1, green area) consists in the design, fabrication and characterization of plasmonic interfaces as individual building blocks for coupling optochips to embedded Single-Mode polymer or glass waveguide oPCBs.

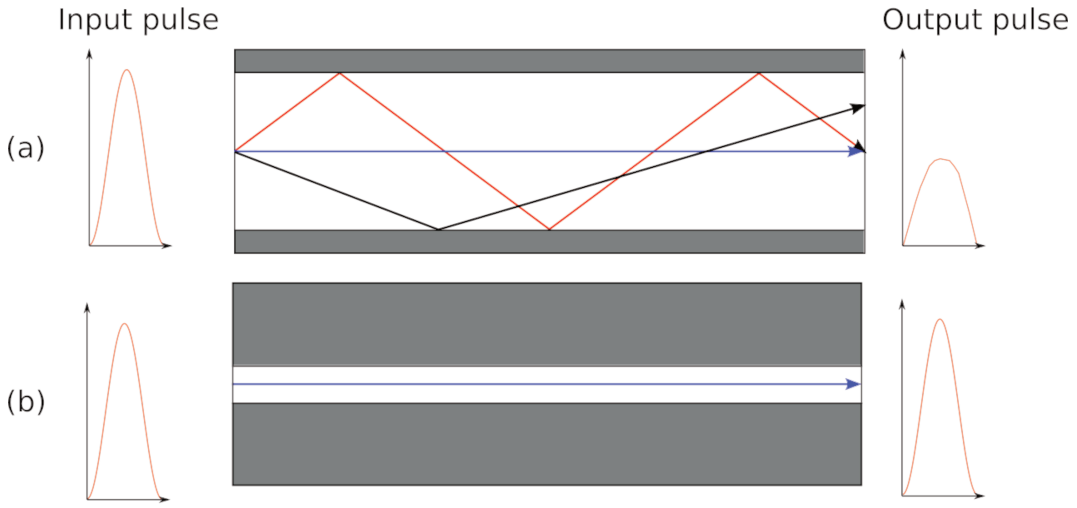

Figure 0.3 – *Differentiation between (a) multi-mode waveguide and (b) single mode waveguide.*

To make optical interconnections between components based on plasmonics, in which in-coupled and out-coupled light beams travel in different directions, different concepts can be considered, inspired from existing optical technologies, like : Free-Space Optical Interconnects (**FSOI**) [8], Photonic Wire Bond (**PWB**) [9], or plasmonic technologies like gold waveguide curved in polymer matrix [10]. During the last decade, the research on SPP progressed very fast [11–17]. The Figure 0.7 shows that the SPP is associated with a continuously increasing number of publications (Figure 0.7(a)) and citations (Figure 0.7(b)) during the last twenty years. The plasmonic arc initially demonstrated by a korean group [18] can be defined as a free-standing mechanically flexible waveguide supporting a propagating plasmon mode and it is the main concept we have studied. Its structure consists of a thin metal slab embedded between two claddings made of flexible polymer. The end-fire coupling of the plasmonic arcs with a VCSEL and a single-mode polymer or glass waveguide, is depicted in Figure 0.4. This way, the plasmonic mode will be guided until reaching the embedded waveguide, without needing micro-lens arrangements in order to re-focus light onto the waveguide as in mirror-based coupling schemes. These arcs need to be developed with the aim of reducing the losses. (Figure 0.5b)

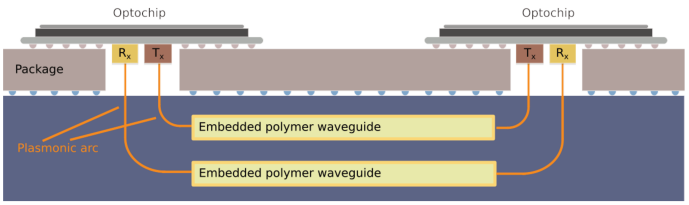

Figure 0.4 – *The Long-Range plasmonic arc interface concept.*

Long-range surface plasmon polariton (**LR-SPP**) strip waveguides are characterized by the geometrical cross section of a metal (usually gold) strip, i.e. by its width w and thickness t, and the dielectric properties of the homogeneous environment (Figure 0.8 (a)).

The strip cross section parameters determine both the propagation loss (due to ab-

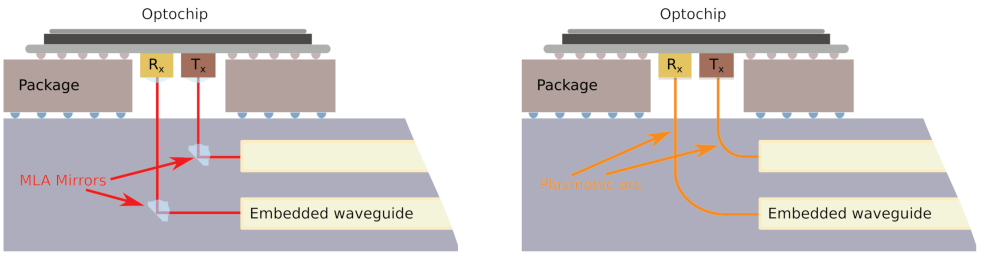

(a) dual-MLA mirror designs for chip-to-board coupling in multi-mode electro-optical PCBs.

(b) plasmonic arc waveguide coupling for chip-to-board interfacing in single-mode PCBs

Figure 0.5 *– Chip-to-Board coupling for optical PCB waveguide*

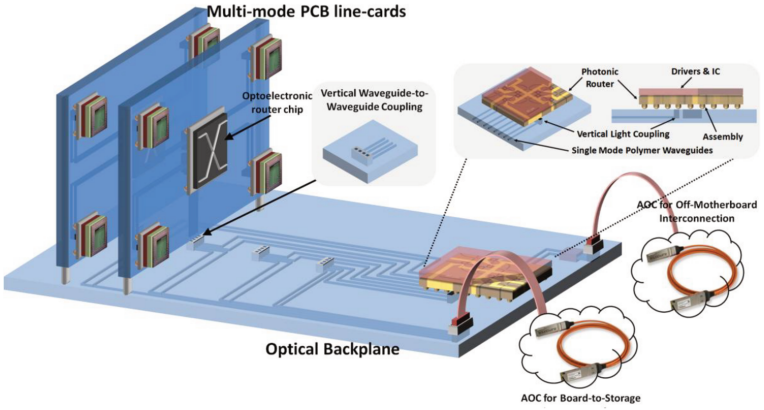

Figure 0.6 *– The board-to-board interconnect platform prototype, employing an optical Backplane hosting a 3D SiP photonic router chip and board-to-board connector sockets utilizing waveguide-to-waveguide coupling.*

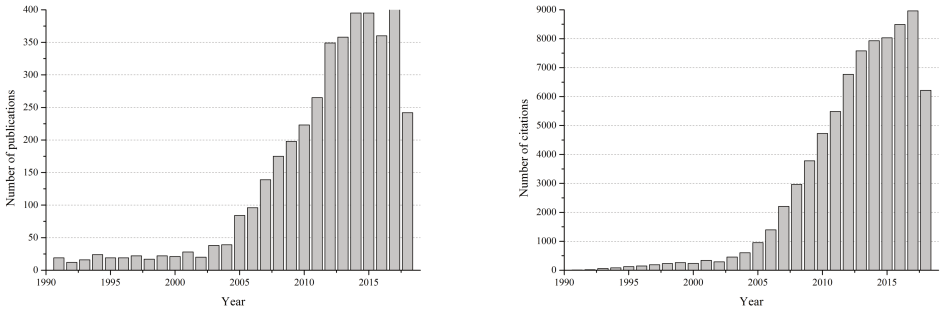

(a) Bibliographic statistics on published items per year

(b) Bibliographic statistics on citations per year.

Figure 0.7 *– Statistics provided by Web of Knowledge for "Surface Plasmon Polariton" as entry (data of Mid September 2018)*

sorption in metal) and the mode size that influences the bend and coupling (to other waveguides or radiation sources) losses. The work of Korean groups [18] shows that a 8 μm-wide and 15 nm-thin gold strip embedded in a polymer results in a LR-SPP waveguide mode (propagation loss $\sim$ 0.5 dB/mm) with a 12 μm-wide spot size that is suitable for low-loss ($<$ 0.5 dB) coupling to a single-mode optical fiber at telecom

wavelengths, while the bend loss remains insignificant down to the bend radii of > 2 mm.

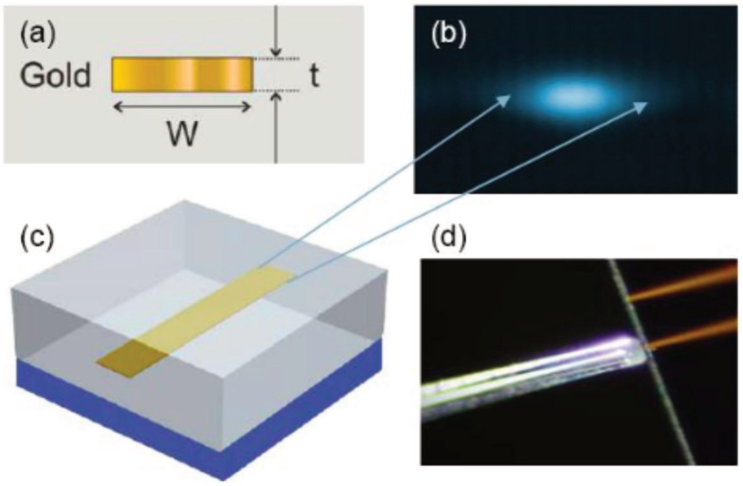

Figure 0.8 *– LR-SPP strip waveguide: (a) cross section geometry, (b) output intensity distribution, (c) 3D-view of the waveguide, and (d) optical image of LR-SPP strip waveguide coupling a single-mode optical fiber (loss < 0.5 dB). (Adapted from [19, 20])*

The second concept we have developed is a rigid chip in which the light mode is redirected at the desired angle; the plasmon is reflected inside the chip, in another direction. Both concepts are expected to show very low loss in the single mode case. This plasmon reflector concept is based on the Total Internal Reflection (**TIR**) of the SPP at the polymer/air interface, this interface being creating by carving through the layers of the plasmonic device, as depicted in Figure 0.9. The plasmon can be reflected with an angle "θ" by this interface plane [21]. The 90^o angle was chosen in this work but any other angle respecting the TIR condition could be chosen in the design. (Figure 0.9). The advantage of this approach compared to the flexible plasmonic arc is less requirements on the polymer's specifications. This waveguide could be used in a vertical position to interconnect the oPCB waveguides and the optochips. With this right angle, we can expect to obtain a redirection loss lower than about 4-5 dB [22–25]. This concept was initially proposed by J.C. Weeber but never demonstrated experimentally.

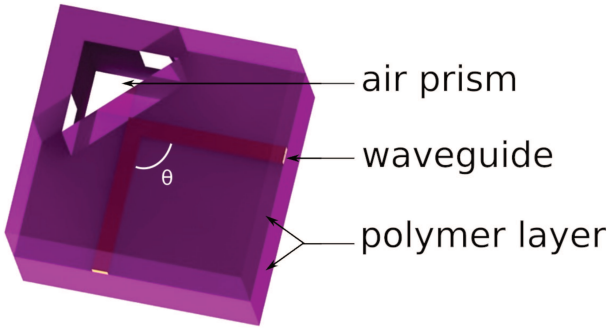

Figure 0.9 *– The Ultra-Long-Range plasmonic arc interface concept.*

Chapter I

Plasmonic Waveguides Interconnects: Introduction and State of the Art.

Contents

Introduction

In order to understand the surface plasmons, we will first study the dielectric function for the case of a noble metal, then recall the phenomena of collective electron oscillation within thin and smooth films. Then, we will study stratified (infinite) layers, which will allow us to approach the plasmon phenomenon. More complex structures will be created in order to reach the surface plasmon case on nanostructured layers.

1 Dielectric function of metals

To investigate the surface plasmon polariton physical concept, the "Drude model" [26] applied to metals can be used to explain the transport properties of electrons in materials. The "Drude model" considers the metal as a gas made up of free conduction electrons. The free electron gas can collectively oscillate and this longitudinal displacement of the density of charges is called a plasmon. The basic view of SPP properties gives a well-known relation between metal permittivity and plasma frequencies, which does not take into account the notion of optical energy band gap and the quantum effects. In metals, most electrons are free because they are not bound to a nucleus. For this reason, the restoring force is negligible and there is no natural frequency. The sum of force applied on free electrons can be described by the Lorentz model:

$$\sum \vec{F} = m.\vec{a} \tag{I.1}$$

$$\vec{F}_{restoring\ force} + \vec{F}_{Lorentz} + \vec{F}_{friction} = m.\vec{a} \tag{I.2}$$

$$-k.\vec{r} + q\vec{E} - \gamma.\vec{v} = m.\vec{a} \tag{I.3}$$

$$m.\ddot{\vec{r}} + \gamma.\dot{\vec{r}} + k.\vec{r} = q.\vec{E}(r,t) \tag{I.4}$$

It assumes that "q" represents electron charge (q≡-e), $\vec{E}(r,t) = \vec{E}_0(r).e^{-i\omega t}$, and $\vec{r}(t) = \vec{r}_0(t).e^{-i\omega t}$.

$$-m\omega^2\vec{r}_0.e^{-i\omega t} - i\omega\gamma\vec{r}_0.e^{-i\omega t} + k\vec{r}_0.e^{-i\omega t} = -e.\vec{E}_0(\vec{r}).e^{-i\omega t} \tag{I.5}$$

$$\vec{r}_0(-\omega^2 - i\frac{\gamma}{m}\omega + \frac{k}{m}) = -e.\vec{E}_0(\vec{r}) \tag{I.6}$$

If $\omega_0^2 = \frac{k}{m}$, where "ω_0" is also called the resonant frequencies.

$$\vec{r}_0 = -e\frac{\vec{E}_0}{m}.\frac{1}{\omega_0^2 - \omega^2 - i\omega\frac{\gamma}{m}} \tag{I.7}$$

Hence the dipole vector:

$$\vec{p}(\omega) = -e.\vec{r} = \frac{e^2}{m(\omega_0^2 - \omega^2 - i\omega\frac{\gamma}{m})}.\vec{E}_0.e^{-i\omega t} \tag{I.8}$$

And polarization vector $\vec{P}$ is defined as a sum of dipole vector:

$$\vec{P}(\omega) = n.\vec{p}(\omega) \tag{I.9}$$

With "n" is the volume unit

$$\vec{P}(\omega) = \frac{n.e^2}{m}\frac{1}{\omega_0^2 - \omega^2 - i\omega\frac{\gamma}{m}}.\vec{E}_0.e^{-i\omega t} \tag{I.10}$$

The energy quantum is $\hbar\omega_p$, where "ω_p" is the plasma pulsation, hence ω_p=$\sqrt{\frac{n_c e^2}{\epsilon_0 m_e}}$, with "$n_c$" is the collision density, "e" is the electron charge, "ϵ_0" the dielectric constant of the vacuum and "m_e" the electron mass.

The electric displacement $\vec{D}$ is related to the polarization density $\vec{P}$ by:

$$\vec{D}(\omega) = \epsilon_0\vec{E}(\omega) + \vec{P}(\omega) \quad \text{(I.11)}$$
$$\vec{P}(\omega) = \vec{D}(\omega) - \epsilon_0\vec{E}(\omega) \quad \text{(I.12)}$$
$$\vec{P}(\omega) = \epsilon_0\epsilon_r(\omega)\vec{E}(\omega) - \epsilon_0\vec{E}(\omega) \quad \text{(I.13)}$$
$$\vec{P}(\omega) = \epsilon_0(\epsilon_r(\omega) - 1)\vec{E}(\omega) \quad \text{(I.14)}$$

The permittivity of material will be: (Lorentz formula)

$$\epsilon_r(\omega) = 1 + \frac{\omega_p^2}{\omega_0^2 - \omega^2 - i\omega\Gamma} \quad \text{(I.15)}$$

with $\Gamma = \frac{\gamma}{m}$

To obtain the Drude formula, it is necessary to assume "ω_0=0", because the Drude model is based on free electron.

$$\epsilon_r(\omega) = 1 - \frac{\omega_p^2}{\omega^2 + i\omega\Gamma} = 1 - \frac{\omega_p^2}{\omega(\omega + i\Gamma)} \quad \text{(I.16)}$$
$$\text{(I.17)}$$

The dielectric function can be written as follows:

$$\epsilon_r(\omega) = \epsilon_r'(\omega) + i\ \epsilon_r"(\omega) \quad \text{(I.18)}$$
$$\text{(I.19)}$$

where

$$\epsilon_r'(\omega) = 1 - \frac{\omega_p^2}{\omega^2 + \Gamma^2} \quad \text{(I.20)}$$
$$\epsilon_r"(\omega) = \frac{\Gamma\omega_p^2}{\omega(\omega^2 + \Gamma^2)} \quad \text{(I.21)}$$

The Drude dielectric function can have different behaviours: if ω<ω_p, the real part of ϵ will be negative and the electrical field cannot penetrate into the metal. The layer becomes reflective. If ω=ω_p, the real part of the dielectric function is equal to 0, all electrons oscillate in phase throughout the material propagation length. And if ω>ω_p, the reflectivity of metal decreases and the metal becomes transparent at this excitation frequency.

2 Volume plasmon polariton

The propagation equation of electric field applied for a bulk metal gives:

$$(\Delta + \frac{\omega^2}{c^2}\epsilon(\omega))\vec{E}(\omega) = 0 \tag{I.22}$$

In complex notation, a plane monochromatic wave, of circular frequency "ω" and wave vector "k" is:

$$\vec{E}(\vec{r},\omega) = \vec{E}_0(\omega).e^{i(kr)} \tag{I.23}$$

$$\Delta\vec{E} = i\vec{k}.(i\vec{k}.\vec{E}) = -k^2.\vec{E} \tag{I.24}$$

$$(-k^2 + \frac{\omega^2}{c^2}.\epsilon(\omega))\vec{E} = 0 \tag{I.25}$$

Hence

$$\omega = \frac{kc}{\sqrt{\epsilon(\omega)}} \tag{I.26}$$

3 Metal reflectivity

The Snell's law for transmission is defined as : $n_1.sin(\theta_i) = n_2.sin(\theta_t)$, the law of reflection orders that $\theta_i = \theta_r$ and the reflectance is determined by $R = \left|\frac{n_2.cos(\theta_i) - n_1.cos(\theta_t)}{n_2.cos(\theta_i) + n_1.cos(\theta_t)}\right|^2$.

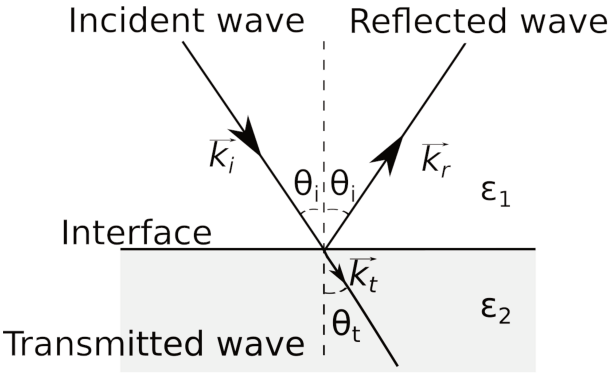

Figure I.1 – *Reflexion of optical waves on material.*

The Figure I.2 shows the shape of the reflectivity calculated at normal incidence angle (i = 0^0) determined by the reflectivity $R_{\theta=0^o}$ equation:

$$R_{\theta=0^o} = \left|\frac{\sqrt{\epsilon(\omega)} - 1}{\sqrt{\epsilon(\omega)} - 1}\right|^2 \tag{I.27}$$

A surface plasmon is excited if $\omega > \omega_p$

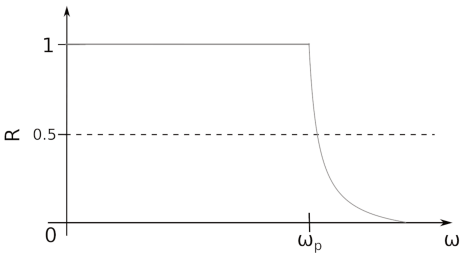

Figure I.2 – *Reflectivity "R" of material with loss*

4 Surface plasmon polariton at a planar interface

A Surface Plasmon Polariton (SPP or plasmon) is a bound electromagnetic (EM) wave propagating at the interface between a metal and a dielectric. The expression polariton is used because a plasmon consists of evanescent EM waves that are coupled to collective surface oscillations of free electrons in the metal. The Long-Range plasmonic propagation mode is a combination of a fundamental long-range surface plasmon polariton strip mode and a dual symmetric dielectric slab mode. The field of the guided mode is mainly distributed in the dielectric. Let us now derive the dispersion relation for plasmons [27]. We set the interface at z = 0. For z < 0 the material is a metal with dielectric constant $\epsilon = \epsilon_m$, and for z > 0 the material is a dielectric with $\epsilon = \epsilon_d$.

Due to the longitudinal character of the electron oscillations, transverse electric (TE) waves cannot couple to plasmons as they do not have an electric field component in the longitudinal direction. So only transverse magnetic (TM) waves can couple to plasmons at a single metal-dielectric interface. They are derived and discussed, closely following [28] and [29]. Having understood the simplest case, the more complex situation of a thin metal film with two interfaces (dielectric-metal-dielectric) is derived and discussed. (Figure I.3)

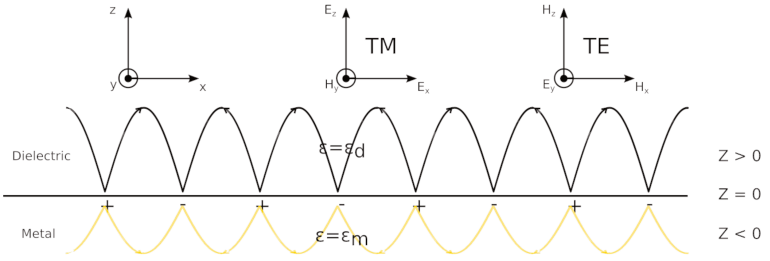

Figure I.3 – *Geometry of plasmon propagation at the interface. An indication of the electric field lines is shown. Also the orientation of the TE and TM waves is given*

As the dielectric constant of the metal is a complex quantity, also the plasmon wavenumber k_{spp} is a complex quantity. When a complex wavenumber is substituted into equation

$$\psi(x, z, t) = \Psi(z) \cdot e^{i(k_x x - \omega t)}$$

we see that these results in an exponential decaying wave in the propagation direction, where $k_x = k_0 * \sqrt{\frac{\epsilon_m \cdot \epsilon_d}{\epsilon_m + \epsilon_d}} = k_{spp}$. ϵ_d, ϵ_m are respectively permittivities of dielectric and

metal, and $k_{spp} \in \mathbb{C}$, since it can be written in the form:

$$\epsilon_\omega = \epsilon'_\omega + i \cdot \epsilon''_\omega \tag{I.28}$$

The relationship between the propagation length L_{prop} and the attenuation coefficient $Im(k_{spp})$ is [30]

$$L_{prop} = \frac{1}{2Im(k_{spp})} \tag{I.29}$$

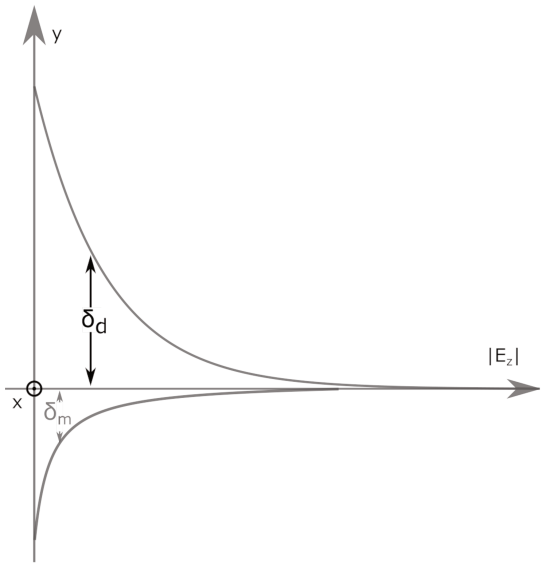

Figure I.4 *– The field in the perpendicular direction is evanescent, reflecting the bound, non-radiative nature of surface plasmon.*

In Figure I.4, the SPP fields decay exponentially into both media and reach a maximum at the interface, a condition that makes SPPs extremely sensitive to interface properties. This prevents power from propagating away from the surface. In the dielectric medium, the penetration depth is δ_d, whereas the penetration length into the metal is δ_m. The Figure I.5 shows the different physical behaviour: the bulk domain where Maxwell equations govern the propagation of light with $\omega > \omega_p$, the light line or free-space electromagnetic waves is conform to the classical model, and the surface plasmon domain where the SPP is the outcome of a collective oscillation of charge carriers in the conducting layer.

5 Observation of SPP at a planar interface

5.a ATR or prism coupling method

The most common experimental approach consists in the radiation of a plasmon polariton at the metal/air interface in the vicinity of a prism. This generates a total internal reflection, which will be sensitive to the evanescent electric field. The surface plasmon is a wave with exponential decrease on the two sides of the interface between the metal and the dielectric medium. In theory, the incident TM polarized wave crosses at first a glass prism with a high refraction index. Then it is reflected on the metal-coated interface at an angle of incidence greater than the critical angle. The photons of the incident ray then

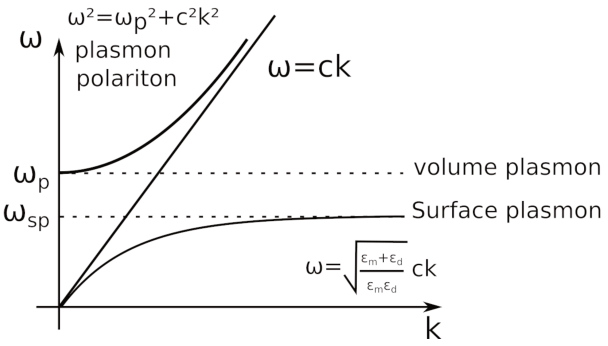

Figure I.5 – *Dispersion diagram for plasmon polariton, free-space electromagnetic waves, and surface plasmons.*

resonate with the free electrons. The prism acts as a coupling device of the incident wave with the surface wave (called "surface plasmon"). The air gap located between the prism and the metal acts as a dielectric layer. The total reflection is verified only if $n.sin(\theta) > 1$,

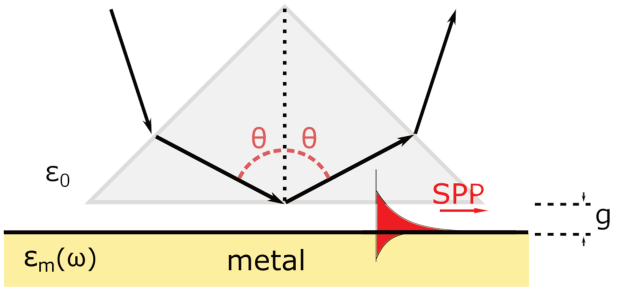

Figure I.6 – *Experimental configurations for propagation length with single prism ATR measurements*

and the sample is brought at close distance to the prism for the coupling of intensity from the evanescent wave of the prism into a surface mode. The gap thickness has to be of the order of, or less than, the wavelength of the exciting light. The first experimental result has been demonstrated by Otto on silver layer [31]. This type of configuration is also called Otto's configuration.

5.b Two-prism experiment by Schoenwald

Another type of setup has been proposed by Schoenwald [32], where the polariton propagation is localized between two prisms. The plasmon is generated by ATR with radiation incident angle on the prism-metal gap. This excitation angle creates an evanescent field on gold layer. A second prism allows the detection of the SPP wave. This technique is a very sensitive method to observe metal surfaces and coatings.

5.c Grating coupler and outcoupler

However, there is a technical difficulty in coupling light between optical fibers and integrated waveguides. Because the waveguide core layer is only a few hundred nanometers thick and the guided mode is strongly confined in the core, there is a large mismatch between the waveguide mode and a single-mode fiber mode with a lower coupling loss of

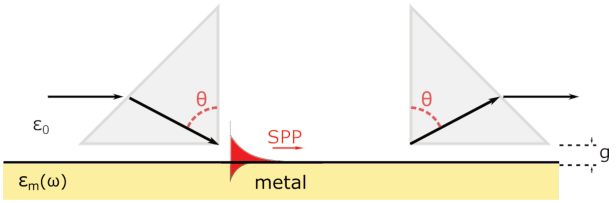

Figure I.7 – *Experimental configurations for propagation length with double prism measurement.*

1 dB. Although the grating coupler is a very elegant solution to the coupling problem, it is possible to design a grating at the beginning of the waveguide and observe a strong coupling between the injection beam and the SPP when $k_{//} = k_{in}.sin(\theta) \pm n\frac{2\pi}{a}$ with n $\in \mathbb{N}$ [33]

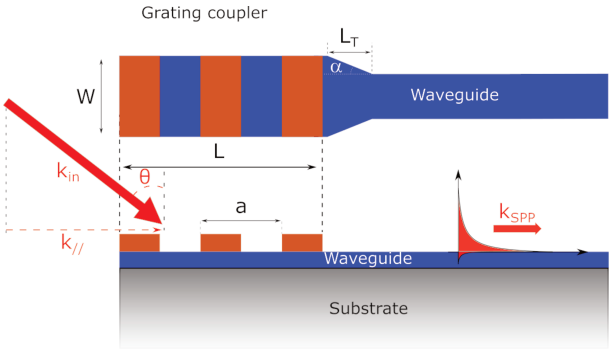

Figure I.8 – *Scheme of the grating coupler.*

6 SSP of a thin film

6.a General case

The basic study consists in depositing a metal layer between two polymer claddings in order to observe the plasmonic mode for a quasi-infinite metal layer [34]. To obtain a better confined plasmonic waveguide with single-mode operation, it is preferable to reduce the width of the metal slab. This way only the single mode can be observed, the other wavelength being removed. [35]

The space of Figure I.9 is divided into three homogeneous and isotropic media. We choose an orthonormal system (O, x, y, z) as the interface between the two media is in the plane (O, x, y) and the incidence plane is in the plane (O, x, z). The indices (I,1), (III,3) and (II,2) respectively correspond to the medium occupying the half-space z $> \frac{d}{2}$, z $< \frac{d}{2}$ and in the middle occupying the area limited by |z| $< \frac{d}{2}$. In a first step, we consider medium III as the substrate. We seek solutions like the Maxwell equations to a particular embodiment of the system that has the form of a surface wave. A surface wave is propagating along the interface and evanescent normally thereto, so we can describe the electric fields associated with this wave in each medium as

$$E_1 = (E_{x,1}; E_{y,1}; E_{z,1}).e^{i(k_x x + k_{z,1} z)} \ (z > \frac{d}{2}) \quad \text{(I.30)}$$

$$E_2 = (E_{x,2}; E_{y,2}; E_{z,2}).e^{i(k_x x + k_{z,2} z)} \ (|z| < \frac{d}{2}) \quad \text{(I.31)}$$

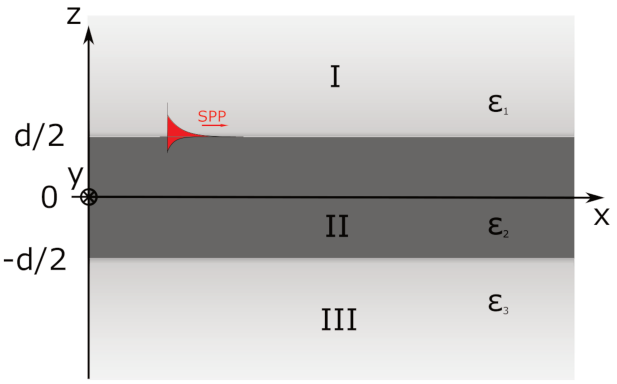

Figure I.9 *– Geometry of a three-medium system with a thin layer I sandwiched between two infinite half areas II and III.*

where k_x component common to the two media due to the conservation of the longitudinal component of wave vector, has a strictly positive real part in order to ensure propagating nature of the wave along the surface, while k_1 and k_2 components are pure imaginary corresponding to an evanescent nature of the field normally to the interface. The components are also interconnected by the conservation of the norm of the wave vector in each medium:

$$k_x^2 + k_{z,1}^2 = (\frac{\omega}{c})^2 \epsilon_1 \tag{I.32}$$

$$k_x^2 + k_{z,2}^2 = (\frac{\omega}{c})^2 \epsilon_2 \tag{I.33}$$

In such a system, each single interface can sustain bound SPP TM mode. For this polarization, the electric field components $E_{y,1}$ and $E_{y,2}$ in each layer are equal at 0 and the continuity of the tangential component of the electric field is required:

$$E_{x,1} = E_{x,2} \tag{I.34}$$

Hence the expression of the electric field is written as:

$$E_1 = (E_0; 0; E_{z,1}).e^{i(k_x x + k_{z,1} z)} (z > \frac{d}{2}) \tag{I.35}$$

$$E_2 = (E_0; 0; E_{z,2}).e^{i(k_x x + k_{z,2} z)} (|z| < \frac{d}{2}) \tag{I.36}$$

The media being homogeneous, the divergence of electric field is zero in each medium, hence :

$$k_x E_0 + k_{z,1} E_{z,1} = 0 \tag{I.37}$$

$$k_x E_0 - k_{z,2} k_{z,2} = 0 \tag{I.38}$$

and we deduce

$$k_{z,1} E_{z,1} + k_{z,2} k_{z,2} = 0 \tag{I.39}$$

Furthermore, the value of ϵE_z are continuous at the interface,

$$\epsilon_1 E_{z,1} = \epsilon_2 E_{z,2} \tag{I.40}$$

Hence, finally gives

$$\epsilon_1 E_{z,2} + \epsilon_2 E_{z,1} = 0 \tag{I.41}$$

This relationship gives the condition of existence of TM-polarized surface waves.

6.b Other type of SPP waveguides

A straight thin metal film of finite width surrounded by a dielectric has been theoretically characterized and proposed as the foundation waveguide for a new integrated optics propagation technology. [36]

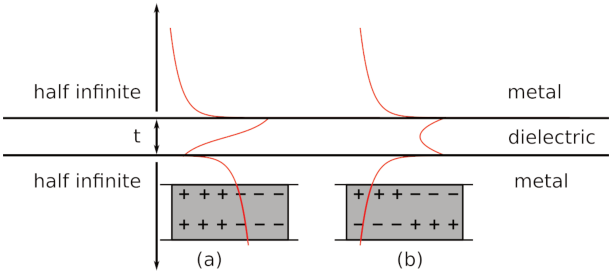

Figure I.10 *– The two modes supported in metal-insulator-metal waveguide, (a) anti-symmetric mode, (b) symmetric mode. (Adapted from [37])*

6.c Experimental observation

In the Kretschmann configuration [38], the metal film is located on the surface of a glass prism. The film is illuminated through the dielectric prism at an angle of incidence greater than the angle of total internal reflection. The light wavevector is increased in the optically dense medium. At a certain angle θ of incidence where the in-plane component of the photon wavevector in the prism coincides with the SPP wavevector on an air–metal surface, the SPP wave vector is defined as:

$$k_{spp} = \frac{\omega}{c}\sqrt{\epsilon_{glass}}.sin(\theta) \tag{I.42}$$

This technique is very used for the leakage radiation microscopy experiment. [39]

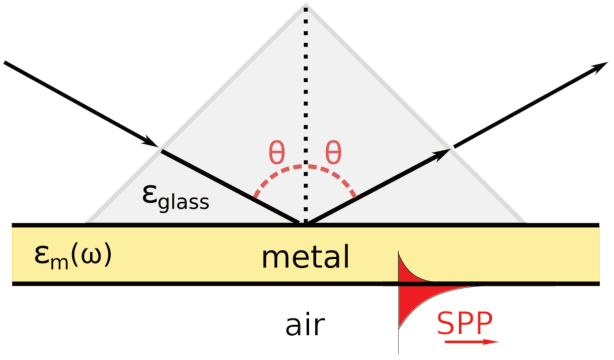

Figure I.11 *– Geometry of Kretschmann configuration*

7 LR-SPP and ULR-SPP

The Long Range surface plasmon polariton and Ultra-Long Range surface plasmon polariton are special cases of waveguides embedded into a polymer. For LR-SPP waveguide

the media I and III are the same, with $\epsilon_1 = \epsilon_3$, thus generating symmetric modes. The LR-SPP modes are known as an electron oscillation in the longitudinal direction. The length of propagation of the mode increases when the metal thickness is decreased [40]. The ultra-long range surface plasmon waves can be supported if dielectric layers with lower index of refraction than that of the dielectric cladding are placed on either side of the thin metal film [41, 42]. Guo and Adato proposed to introduce a thin polymer layer with low-refractive index on both sides of the metal waveguide to extend the distance of the long range surface plasmon polariton [43]. Durfee explored similar structures and, additionally, the case where only one low-index layer is placed alongside the metal film. [44]

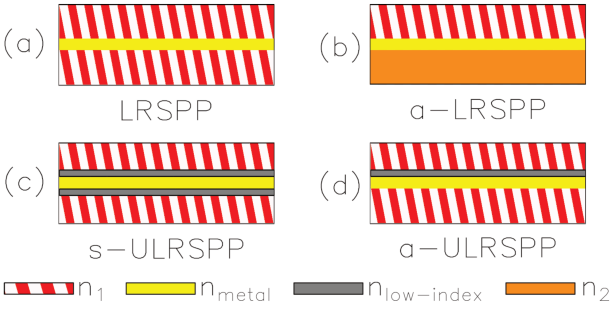

Figure I.12 – *Schematic of different layered structures. Central yellow line: metal layer, gray line: low-index dielectric, hatched area: high index. (Adapted from [44])*

The Figure I.12 shows four different structures of plasmonic waveguides. The two upper structures describe a metal core surrounded symmetrically or non-symmetrically by dielectric cladding layers designed for low-loss lightwave guiding (Figure I.12 (a)). In the second structure (Figure I.12 (b)), the refractive index of the lower cladding differs from that of the upper cladding. The two structures in the bottom of the figure show a metal waveguide embedded into respectively, a bi-layer polymer cladding (Figure I.12 (c)) and an asymmetric polymer cladding with a thin layer with lower refractive index between the metal and the upper cladding (Figure I.12 (d)). A complementary structure exists where the resin is wrapped by metal layer. These devices are named Metal-Insulator-Metal waveguides, alias MIM waveguides. [45]

8 SPP waveguide

8.a Metal stripe on glass substrate

The mode of a thin metal strip deposited directly on a glass substrate has been studied by Berini [46]. In this first theoretical study, the model of the metal film is completely studied and discriminated. The difference between the substrate and superstrate permittivities has been varied and the effects on the modes have been determined. It has been found that the modes may change dramatically in character as the dimensions of the metal film change and as the difference between the substrate and superstrate permittivities increases.

The observations of Berini have been confirmed by PSTM-experimental results [47], with a surface plasmon guided by laterally confined thin films deposited on a glass substrate. It

shows a good coupling between thin film SPP and the stripe modes at visible frequencies.

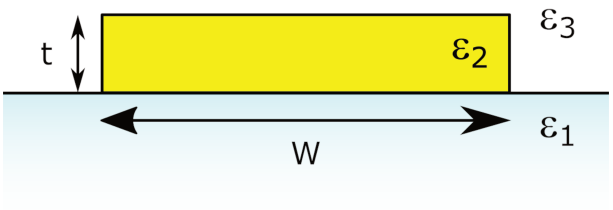

Figure I.13 – *Metal strip deposited on glass substrate (Adapted from [46])*

8.b DL-SPP waveguide

In 2006, a new class of waveguides called "Dielectric-Loaded Surface Plasmon-Polariton" (**DL-SPP**) waveguide was introduced. This waveguide consists of polymer strips deposited on a layer of gold (Figure I.14). They exhibit sub-wavelength optical confinement that can bridge the gap between the scale of optical components and integrated electronic circuits. Mostly it allows a better transverse confinement of the EM field. They are easily achievable by electron beam lithography and offer the possibility of using the dielectric tape as the active medium to functionalize the waveguide for example using the thermo-optic [48], electro-optics [49], or non-linear effects [50] . Finally, the use of a dielectric gain medium also allows to partially offset the losses caused by the metal.

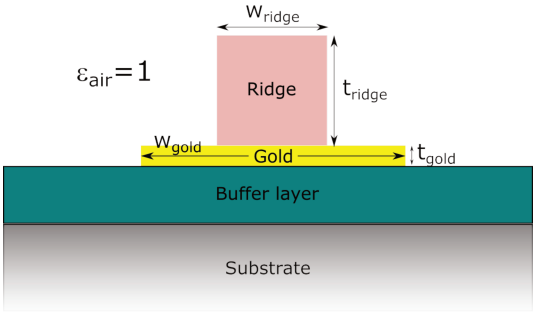

Figure I.14 – *Structure of DL-SPP waveguide*

Holmgaard [51] extends this waveguide category with an additional layer of dielectric called buffer that is added between the substrate and the metal and allows a symmetrical field from either side of the metal. The DL-SPP waveguide structure is appropriate for interfacing photonics and electronics [52] and it allows thermo-optically-induced switching phenomena. (European Project PLATON) [53]

8.c LR-SPP waveguides and bending application.

In [43], Guo and Adato investigated the action of high-index layers addition along the metal waveguide, finding that it increases the confinement as well as the attenuation of the LR-SPP (Figure I.15). The propagation loss experienced by long-range plasmon polaritons in ultrathin gold stripe waveguides embedded in different polymer cladding materials was studied by Jin tae Kim & *al.* [54–56] with multilayer cladding structure

(Figure I.17(b)) using commercial polymer Exguide FOWG from Korean company Chemoptics. In their work, the waveguide is made of a 8 nm thick, 4 μm wide, and 68 mm long silver strip that is embedded in a 10 μm thick clad of mixed FOWG grades FOWG-116 (n = 1.506) and FOWG-115 (n = 1.547) to get a refractive index of n = 1.524, and this layer itself is embedded in two claddings with a mixture of both grades in order to obtain a refractive index of 1.514. (Figure I.16)

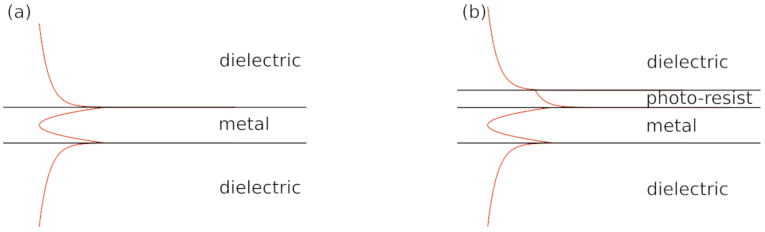

Figure I.15 – *Propagation decay for (a) LR-SPP and (b) ULR-SPP*

In an ideal straight LR-SPP waveguide bounded by semi-infinite dielectrics, the propagation is fundamentally limited by absorption losses in the metal only. However, there are

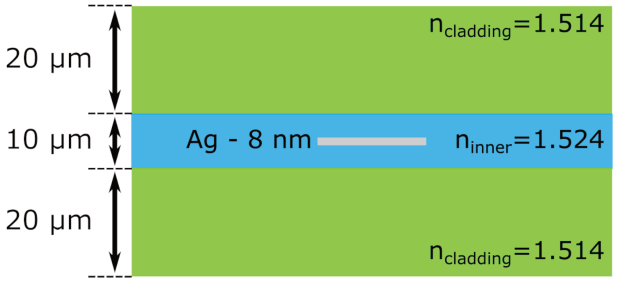

Figure I.16 – *LR-SPP waveguide based on multilayer cladding [54]*

many other factors influencing the propagation loss inside a waveguide, like the deviation from perfect symmetry in refractive index between top and bottom cladding layers, mode leakage in the case of finite cladding layer thickness, scattering losses from imperfect metal stripe edges, scattering [56–59]. Three configuration found in the literature have been studied by the Korean group as shown in Figure I.17. In the multilayer cladding configuration, the refractive indices of the cladding (lower index) and core layer are (higher index) will have to differ by about 0.01.

In the context of PhoxTroT and the important constraints on loss budget, it is very important for the structure to have the best possible symmetry of refractive index around the gold slab because the LR-SPP mode propagation length is very dependent of this symmetry.

8.d Bending loss

For the "multilayer" structure I.16, the bending loss was measured by [54] for a 180^o turn with bending radii from 1 mm to 12 mm, and for smaller angles with bending radii of 20, 25, and 30 mm by inserting the flexible LR-SPP waveguide into the slot of two sets of

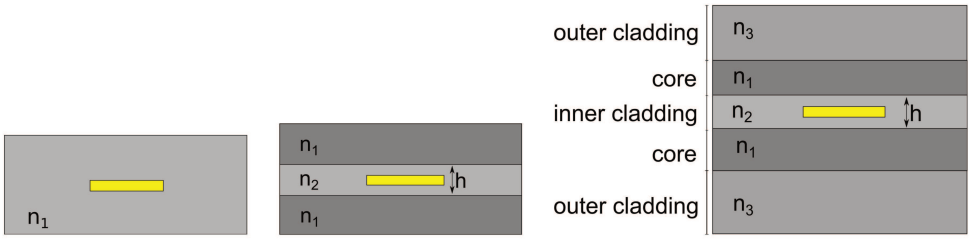

(a) single cladding *(b) multilayer cladding* *(c) dualcore cladding*

Figure I.17 – *The three cladding structures for LR-SPP waveguide*

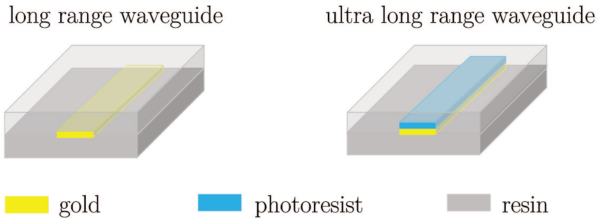

Figure I.18 – *Sketch of structures bearing the long range surface plasmon polariton (left) and ultra long range surface plasmon polariton (right)*

mechanical components and by having both ends of the waveguide fiber-pigtailed using single-mode fibers. The measured vertical bending loss is lower than 0.3 dB/180^o at a wavelength of 1310 nm for the bending radii down to 2 mm. The bending loss rapidly increases when the bending radius is further decreased below 2 mm. This result is in good accordance with the simulation study. The study also shows that the waveguide can be bent to 90^o with very limited increase in insertion loss for a radius of bends lower than 2 mm.

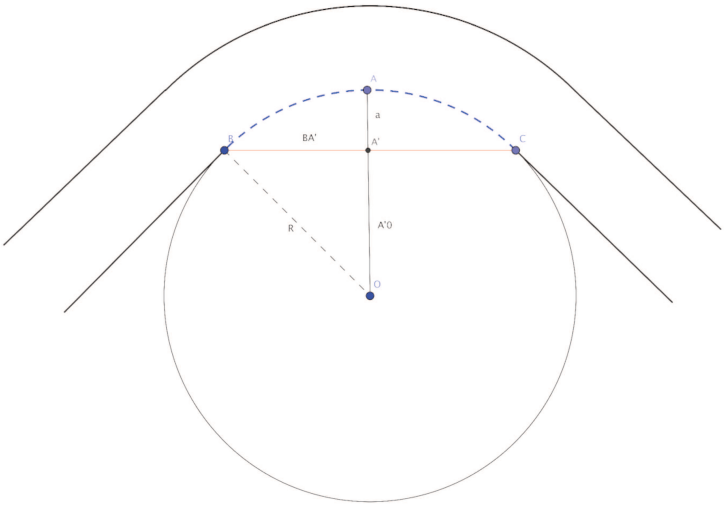

Figure I.19 – *Bending radius*

The bending radius is defined by:

$$R^2 = BA'^2 + A'0^2 \quad \text{(I.43)}$$
$$R^2 = BA'^2 + (R-a)^2 \quad \text{(I.44)}$$
$$R^2 = BA'^2 + R^2 + a^2 - 2aR \quad \text{(I.45)}$$
$$R = \frac{BA'^2 + a^2}{2a} \quad \text{(I.46)}$$

A dual core cladding structure as presented in Figure I.20 has been studied by the same research group [56]. This structure is composed of five resin layers. The metal waveguide is a 5 nm thick, 3.5 μm wide and 70 mm long gold strip which is embedded in a 5 μm inner cladding. This cladding is made of mixed FOWG grades (FOWG 116 with n=1.506 and FOWG 115 with n=1.547) in order to have a fixed refractive index at n_2=1.524. The whole structure is embedded in the FOWG outer cladding with a refractive index n_1=n_3=1.514. The outer-cladding, inner-cladding, and core measured respectively 20 μm, 1 μm and 5 μm (Figure I.20). The propagation loss (non-bended waveguides) is less than 1.0 dB/cm (at a wavelength of 1.31 μm) for Au stripes of width smaller than 5.0 μm. The lowest propagation loss of 0.25 dB/cm was achieved with a 2.5 μm-wide stripe. In comparison, the 3-layer and single-layer structures show much higher propagation losses for the same gold strip width. Therefore, the 5-layer configuration seems advantageous in this respect.[54]

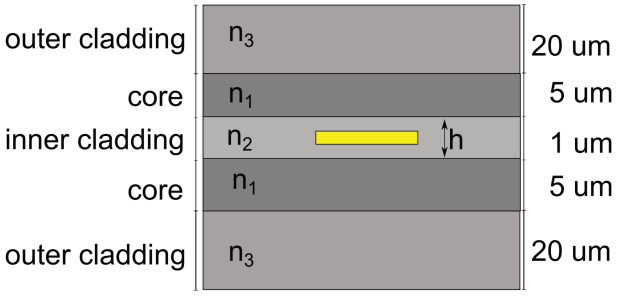

Figure I.20 – *Hybrid plasmonic waveguide based on dual core slab*

The fiber-to-fiber insertion loss of the straight 7 cm-long hybrid plasmonic waveguide was in the 10 to 15 dB range with gold. Down to R = 1.5 mm bending, the measured insertion loss did not increase significantly. For R < 10 mm, the insertion loss increased gradually and the additional insertion loss due to a 180^o bending of R = 2 mm was measured to be about 1 dB at a wavelength of 1310 nm. At the same wavelength, simulation of the waveguide made of a 5 nm thick gold stripe gives a bending loss lower than 1 dB/180^o for the bending radii down to 2 mm.

These results show that these Long-Range plasmonic waveguides are very effective for bending loss with gold stripes (Figure I.21). It was also shown that the careful choice of waveguide structural dimensions has a great importance for minimizing the propagation loss. [55]

Many studies [60–68] concur on the fact that the inhomogeneous metal structure generated by the unstable conditions in the fabrication procedure acts as a major

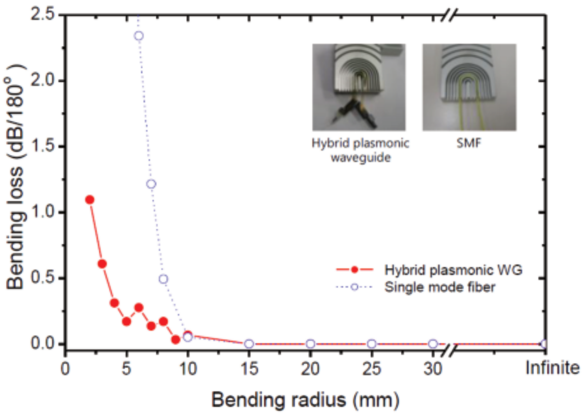

Figure I.21 *– Measured additional bending loss of the flexible hybrid plasmonic [55]*

loss-generating factor because the SPP mode is very sensitive to the surface condition of the metal.

A severe bending loss of the LR-SPP waveguide with a single layer of cladding (h=0) was predicted by simulation, and is a big problem that must be overcome for useful application of LR-SPP waveguides. For this reason, an LR-SPP waveguide with multilayer cladding or dual core cladding (h≠0) is often employed to reduce propagation losses, in particular in bending situation.

8.e In plane bending application

Long-range surface plasmon-polariton mode propagation, which occurs within a finite-width curved thin-film film embedded in a homogeneous dielectric medium, is described in numerous publications with different metals. Wang's study shows that the loss is dependent on the radius of the bending on Silver Nanowire [66] in visible spectrum. Similar studies have been regrouped by Berini [69] in the infrared spectrum for various passive elements of Au stripes. Astley [70] studies the impact of Terahertz-pulses propagation within nano-wires of steel in straight configuration as well as with an in-plane bend of 90^o with the help of an aluminium reflection mirror.

9 Conclusion of Chapter I

- A plasmon is a wave propagating at the interface between a metal and a dielectric
- The EM wave of the LR-SPP structure is mainly contained in the dielectric layer, the skin effect of metal limits the wave penetration. If the metal film is thin enough, the surface plasmon polariton modes of the two surfaces couple to a mode spanning across the two interfaces.
- The waveguide characteristics of being mono mode or multimode depends on its dimensions.
- The modes of a thin metal stripe (i.e. a thin film of finite width) are examined with

the help of numerical simulations [36]. Under the right circumstances the stripe exhibits a mode with low attenuation, called long-range surface plasmon polariton mode (LR-SPP mode), that can be used to guide light waves. (Figure I.22)

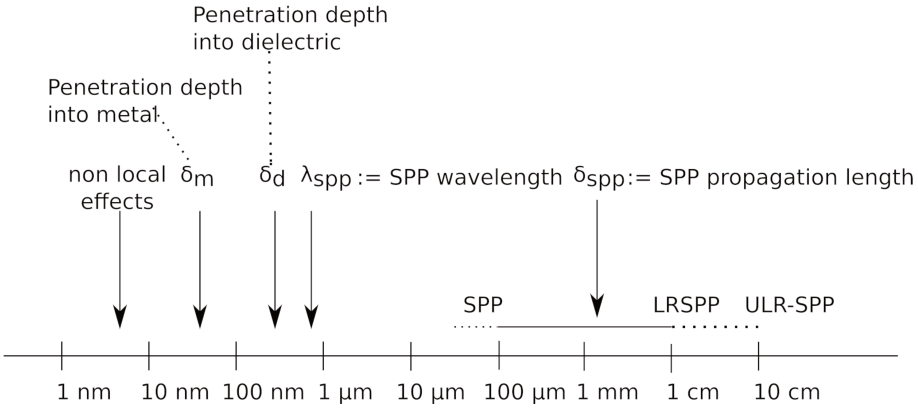

Figure I.22 – *The different length scales of surface plasmon polariton. (Adapted from [71])*

- There are many structures based on the concept of a gold waveguide embedded into two claddings of polymer : simple cladding, multilayer cladding, ultra long range, the more complex structures show improved bending loss.

Chapter II

Design and Simulation

Contents

Introduction

Prior to the fabrication of waveguides, it is needed to perform numerical simulation of the SPP modes sustained by our structures. The numerical simulation will help to find the better structures configurations in order to get the supported plasmon mode with the lowest losses.

1 Simulation methods

The two-dimensional eigenvalue problem has been solved by two different methods: the Effective Index Method (**EIM**), where the waveguide is replaced by an equivalent slab waveguide with an index profile derived from the geometric shape of the waveguide, and the Finite Element Method (**FEM**), as it is commonly used to numerically solve equations describing the dynamic behavior of physical systems.

1.a The Effective Index Method

The Effective Index Method was developed by the group of Bozhevolnyi [72]. It is based on an approximation that reduces a 2D index profile to an equivalent one-dimensional

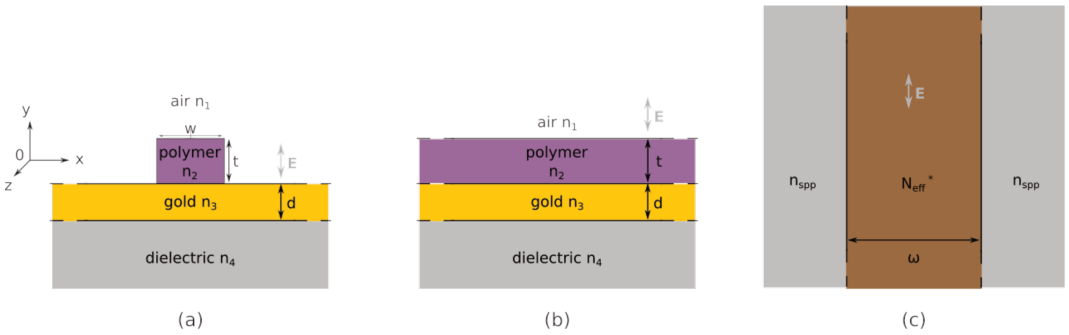

Figure II.1 *– Conventional EIM. (a) View of the cross section. (b) Slab waveguide approximation. (c) Equivalent-index profile slab waveguide. (Adapted from [73])*

(1D) planar slab model.

The Figure II.1 is characteristic of the case of DL-SPP[1]. To solve this 2D problem, it is necessary to proceed step by step. First, each of the four layers (dielectric/gold/photoresist/air) is considered of infinite lateral extension in the x-axis. The top (air) and bottom (dielectric) layers are considered as two semi-infinite in the (depth) y-axis. The gold layer is considered as an infinite and uniform layer in x-axis. This step is used to determine the effective index "N^*_{eff}" of guided modes in a planar stack waveguide structure observed by side view. (Figure II.1 (b))

Then, the stack is observed from the top view. From this point of view, the polymer-metal structure is similar to a single waveguide with a width "w" and refractive index "N^*_{eff}". (Figure II.1 (c)). This method, computed into Matlab is used to determine the complex effective index, number of modes and propagation lengths inside each layer of the stack.

1.b The Finite Element Method

The Finite Element Method [74], or **F.E.M.**, is based on a 2-step process applied in macroscopic systems. The first step consists in the division of the global domain in many sub-domains by an adequate meshing, where each sub-domain represents a part of the global. The second step is to merge all solutions of the complete system as an assembly of its elements following precisely the same rules as those applicable to standard discrete problems. This determination method by small area gives a good approximation for complex problems.

[1] Dielectric Loaded-Surface Plasmon Polariton

2 Design and simulation of the LR-SPP plasmonic arcs.

2.a Modal profile simulation.

Initial simulations were performed for Chemoptics polymer Exguide FOWG-115 ($n_{FOWG-115}$ = 1.506 at λ_{TC}[2] = 1550nm), FOWG-116 ($n_{FOWG-116}$ = 1.547 at λ_{TC}), three grades of Momentive resin ($n_{Momentive}$ = 1.41, 1.44, 1.47 at λ_{TC}), provided by Momentive Performance Materials GmbH.[3] and a new polymer "LIGHTLINK" sold by "MicroChem Corp.[4]" ($n_{LIGHTLINK}$ = 1,473 at λ_{TC}) in the single cladding configuration. Different width and thickness of the gold strip were considered.

2.a.1 Propagation loss simulation.

The propagation length is defined as the distance for the SPP intensity to decay by a factor of 1/e [69, 75]. The propagation loss is determined by the equation I.29 from chapter I with $k_{spp} = k_o n_{eff}$ [30] using it is imaginary part as :

$$L_{spp} = \frac{1}{2 \cdot Im(k_o n_{eff})}$$

.

2.a.2 FOWG-115 & FOWG-116 polymer.

To find the best configuration with the lowest propagation loss a structure of two 30 μm-thick claddings and a width of 100 μm was used. The gold waveguide is placed in the middle of the structure (shown in Figure II.2a).

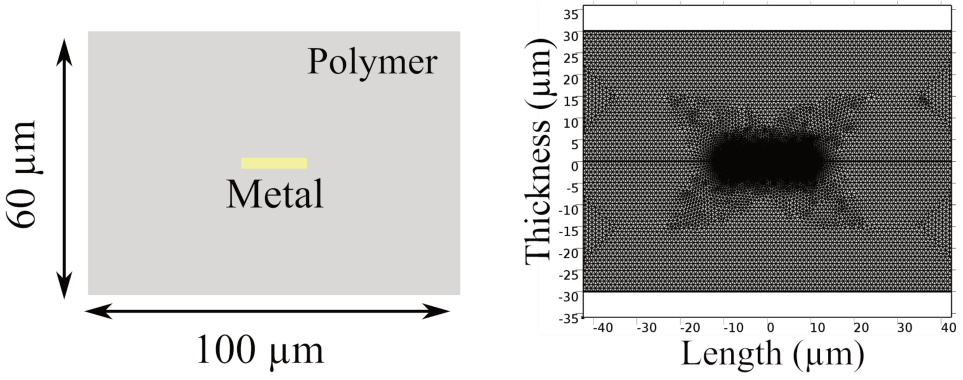

(a) Structure used in FEM on single waveguide.

(b) Mesh used in FEM for mode analysis study on single waveguide.

Figure II.2 *– Structure used for simulation*

We shall consider three waveguide widths (5 μm, 10 μm and 15 μm) and three gold thickness (10 nm, 15 nm, 20 nm) in order to deduce the propagation length as well as the mode size of each structure. In a first approach, we consider the polymers FOWG-115 ($n_{FOWG-115}$ = 1.506) and FOWG-116 ($n_{FOWG-116}$ = 1.547) at λ_{TC}, which are completely

[2] λ_{TC} = telecommunication wavelength

[3] `www.momentive.com`

[4] `http://www.microchem.com/Prod-LightLink.htm`

Polymer	grade	n	k
FOWG	115	1.507	0
	116	1.547	0
Momentive		1.41	0
		1.44	0
		1.47	0
LightLink		1,479	0
SU8	3035	1,57	8e-5

Table II.1 *– Cladding refractives index used for simulations*

transparent ($k_{FOWG-115} = 0$ and $k_{FOWG-116} = 0$). The propagation loss is defined as the proportional inverse of propagation length. Figure II.3 shows that for a reasonably low gold thickness, between 15 and 20 nm, the expected propagation loss lies in the 0.4—2 dB/mm range. The propagation loss decreases when the width ω is decreased from 15 to 5 μm. The profile mode of this simulation is placed in Annexe A, section 1.

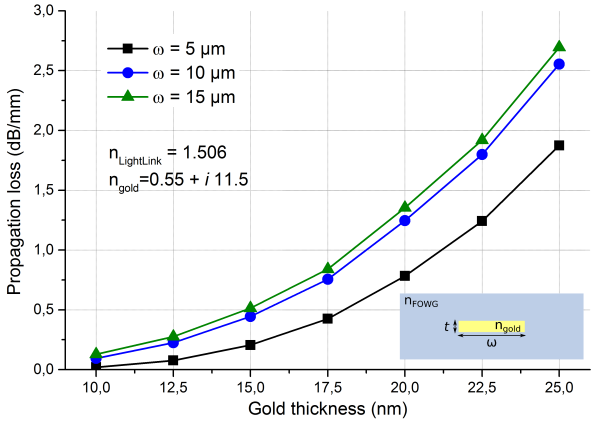

Figure II.3 *– Simulation of propagation losses for varied w and t for FOWG-115 polymer.*

From the fabrication point of view, it is actually not recommended to decrease the gold strip thickness below 15 nm. The main reason for this is to avoid having a film below the percolation limit and having a too large film roughness in comparison to the thickness.

As the purpose of the plasmonic waveguides is to be end-fire coupled with the core of a fiber optic, and because the fiber core diameter is 9 μm, the preferred cases are those where the plasmon longitudinal mode size FWHM is the closest to 9 μm. A 10 μm metal strip width happens to give a longitudinal FWHM close to this value for 15 nm gold thickness and will thus be the preferred one. Following these simulations shown in Figure II.4, the dimension of the gold strip was chosen to have a width of 10 μm, and a thickness of 15 nm for optimized single mode propagation. The profile mode of this simulation is placed in Annexe A, section 2.

2.a.3 Momentive and LightLink polymers

The same work was done on three different polymer grades from Momentive ($n_{Momentive} = 1.41, 1.44, 1.47$ at λ_{TC}) and "LIGHTLINK" polymer with refractive index $n_{LIGHTLINK} = 1.473$ at λ_{TC}. The extinction coefficient is assumed to be zero.

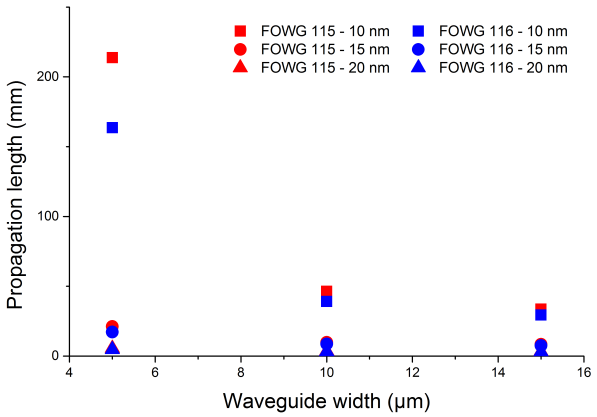

Figure II.4 *– Propagation length versus waveguide width determined for three thin gold thickness of Exguide FOWG polymers with* $k_{clad} = 0$.

Table II.2 shows the effective indexes and propagation lengths determined for five waveguides widths (5 μm, 7.5 μm, 10 μm, 12.5 μm, and 15 μm) and two gold thickness (15 nm and 20 nm).

The Figure II.5 shows that for any waveguide width the propagation length is much decreased when the metal thickness is increased (assuming no absorption, $k_{clad} = 0$). In addition the main trend of the plot is a quick decrease of the propagation length as the waveguide width increases.

Figure II.6 describes the propagation length reduction according to the increase of absorption part of the cladding. This phenomenon can be explained by the increase of the effective index imaginary part $k_{cladding}$.

Figure II.7 shows that for a reasonably low gold thickness, between 15 and 20 nm, the expected propagation loss lies in the 0.4—2 dB/mm range for Momentive polymer (Figure II.7a) and a similar propagation loss range is observed for LightLink polymer (Figure II.7b). The propagation loss decreases when the width ω is decreased from 15 to 5 μm. We obtain a better propagation loss for the last polymer compared to FOWG.

The longitudinal mode size seems to be linked with the waveguide width, whereas the transversal mode decrease would be linked with the thickness increase

3 Design and simulation of the ULR-SPP redirection component.

3.a Mode simulation.

The modal profile simulation for the "Ultra Long Range Surface Plasmon Polariton", or **ULR-SPP**, were calculated using EIM method. In this case, an additional layer of photoresist above the metal waveguide is introduced. The first step is to study the effect of the resist refraction index and thickness on the mode size. Then, the EIM is used to

n_{clad}	width (μm)	Au (nm)	n_{eff}	k_{eff}	L_{spp} (mm)
1.41	5	15	1.410131	3.30E-06	37.384
1.41	7.5	15	1.410360	6.89E-06	17.897
1.41	10	15	1.410560	8.97E-06	13.754
1.41	12.5	15	1.410708	1.01E-05	12.171
1.41	15	15	1.410817	1.08E-05	11.396
1.41	5	20	1.410452	1.43E-05	8.609
1.41	7.5	20	1.410914	2.22E-05	5.567
1.41	10	20	1.411234	2.59E-05	4.764
1.41	12.5	20	1.411447	2.78E-05	4.436
1.41	15	20	1.411593	2.89E-05	4.273
1.44	5	15	1.440159	3.99E-06	30.933
1.44	7.5	15	1.440415	7.83E-06	15.745
1.44	10	15	1.440628	9.97E-06	12.367
1.44	12.5	15	1.440784	1.12E-05	11.056
1.44	15	15	1.440896	1.18E-05	10.412
1.44	5	20	1.440531	1.64E-05	7.502
1.44	7.5	20	1.441028	2.46E-05	5.022
1.44	10	20	1.441363	2.83E-05	4.354
1.44	12.5	20	1.441583	3.02E-05	4.080
1.44	15	20	1.441737	3.13E-05	3.942
1.47	5	15	1.470192	4.76E-06	25.914
1.47	7.5	15	1.470475	8.85E-06	13.941
1.47	10	15	1.470702	1.10E-05	11.165
1.47	12.5	15	1.470864	1.22E-05	10.075
1.47	15	15	1.470980	1.29E-05	9.536
1.47	5	20	1.470617	1.87E-05	6.586
1.47	7.5	20	1.471151	2.71E-05	4.549
1.47	10	20	1.471500	3.09E-05	3.990
1.47	12.5	20	1.471725	3.28E-05	3.760
1.47	15	20	1.471876	3.38E-05	3.645

Table II.2 – *Effective index and propagation lengths for three Momentive resin grades with* $k_{clad} = 0$.

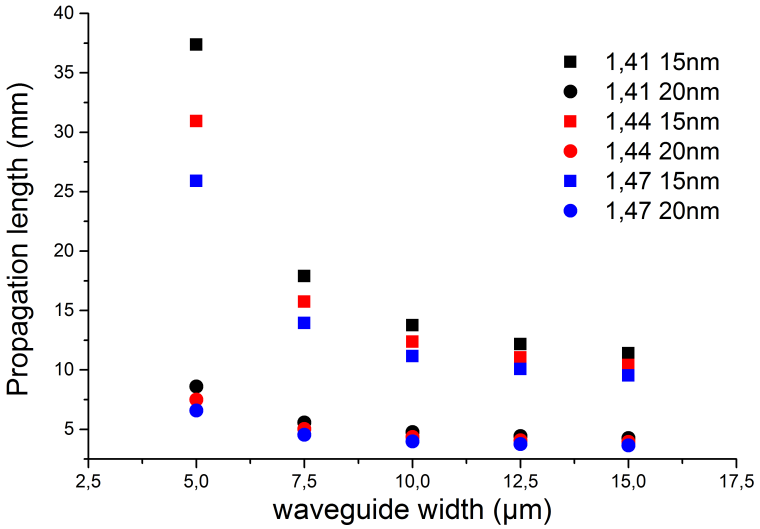

Figure II.5 – *Propagation length versus gold widths for three Momentive resin grades with* $k_{clad} = 0$.

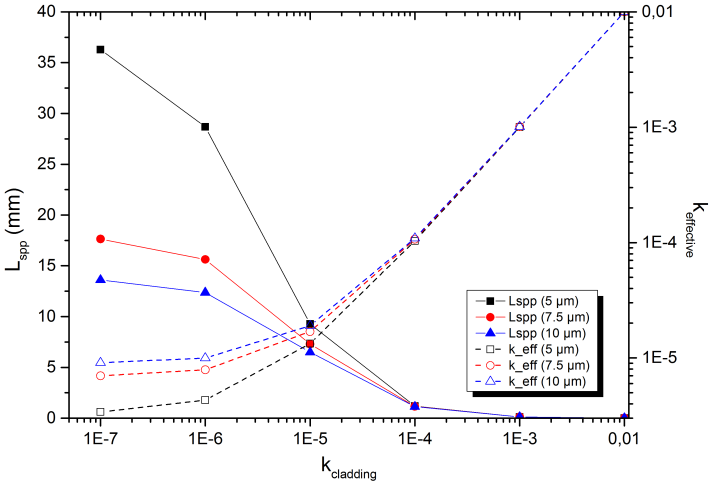

Figure II.6 – *Impact of variations of k on* L_{SPP} *for three smaller widths with Momentive* $n_{Momentive}$*=1,41 at* λ_{TC} *and gold thickness of 15 nm.*

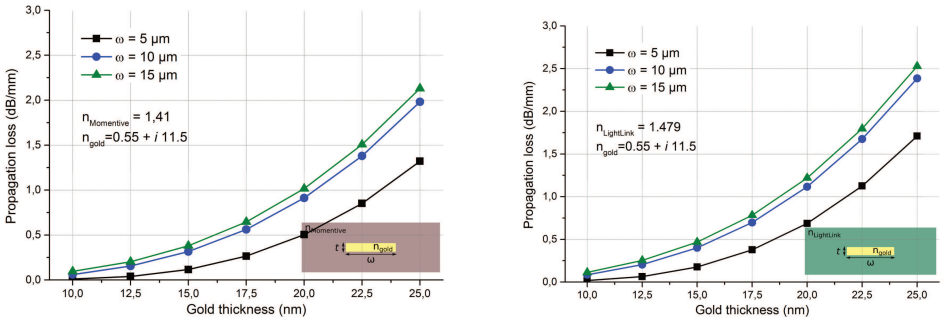

(a) for Momentive polymer. *(b) for LightLink polymer.*

Figure II.7 *– Simulation of propagation losses for varied width and thickness*

width (μm)	Au (nm)	n_{eff}	k_{eff}	L_{spp} (mm)
5	15	1,473195	4,84E-06	25,476
7,5	15	1,473481	8,95E-06	13,776
10	15	1,473710	1,12E-05	11,054
12,5	15	1,473873	1,24E-05	9,983
15	15	1,473988	1,30E-05	9,454
5	20	1,473627	1,90E-05	6,503
7,5	20	1,474163	2,74E-05	4,505
10	20	1,474514	3,12E-05	3,956
12,5	20	1,474740	3,31E-05	3,730
15	20	1,474891	3,42E-05	3,609

Table II.3 *– Effective index and propagation lengths for Lightlink resin with* $n_{(\lambda\ =\ 1550\ nm)}\ =\ 1.473$ *and k=0.*

determine the effective index for each layer and refractive index of the photoresist. The effective index solutions are then calculated by FEM, in order to estimate the mode size.

The study will be focused on a 80 μm × 60 μm field with an automatic meshing control for extra fine elements of the structure. (Figure II.8(a))

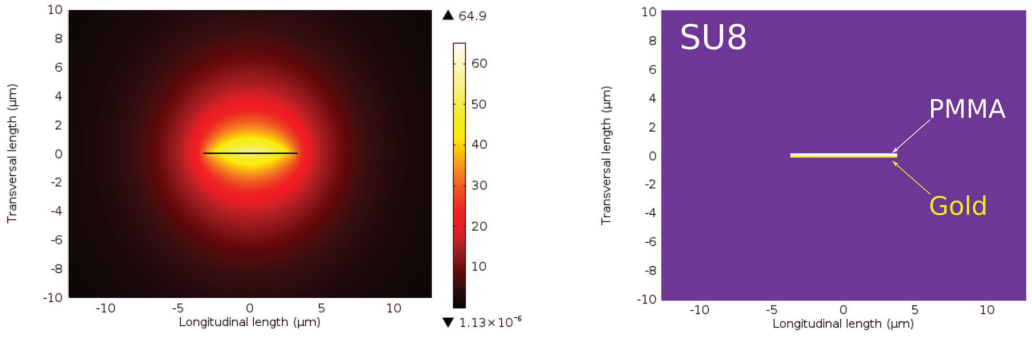

(a) front view mode *(b) Sketch of structure.*

Figure II.8 *– FEM on the ULR-SPP configuration. (20 nm-thick and 7.5 µm-wide gold waveguide covered with 30 nm of PMMA)*

3.b Propagation loss simulation.

The propagation loss simulation is used to determine the best compromise between the gold thickness, photoresist thickness and refractive index. The first step is to determine the best gold thickness to propagate as far as possible. Figure II.9 shows the propagation length for a set of five waveguide widths (5.0 μm; 7.5 μm; 10.0 μm; 12.5 μm; 15.0 μm) embedded into two SU8 cladding with the same refractive index. In this figure, the propagation length decreases as the gold thickness increases. The five widths show the same decay curve, and therefore the best thickness value will be the the lowest one. However we are limited by the fabrication process. If the thickness is lower than 15 nm, the percolation limit is not reached because there is no uniform layer. If the thickness is too high, the propagation length is drastically reduced because it cannot maintain plasmon containment along the metal waveguide. (Figure II.9)

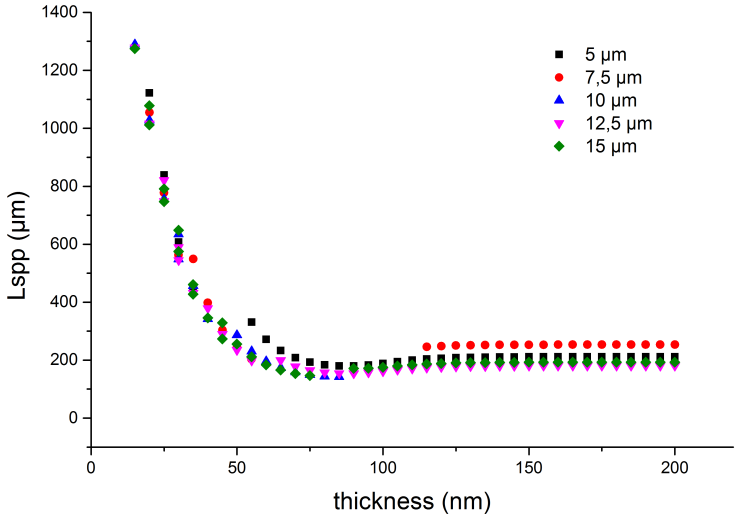

Figure II.9 – *Propagation length of the zero order mode for a gold layer embedded in SU8 cladding*

The Figure II.10 shows a variation map of the propagation length according to both polymer refractive index in X and polymer thickness in Y. (with the darker colors showing the higher propagations and the lighter colors the shorter ones). On this map, two main regions can be distinguished. First a plateau region of high propagation length which is covering higher $n_{polymer}$ and lower thicknesses. On the contrary a dip of propagation length is observed in a smaller region where both the resist thickness is high and the $n_{polymer}$ is low.

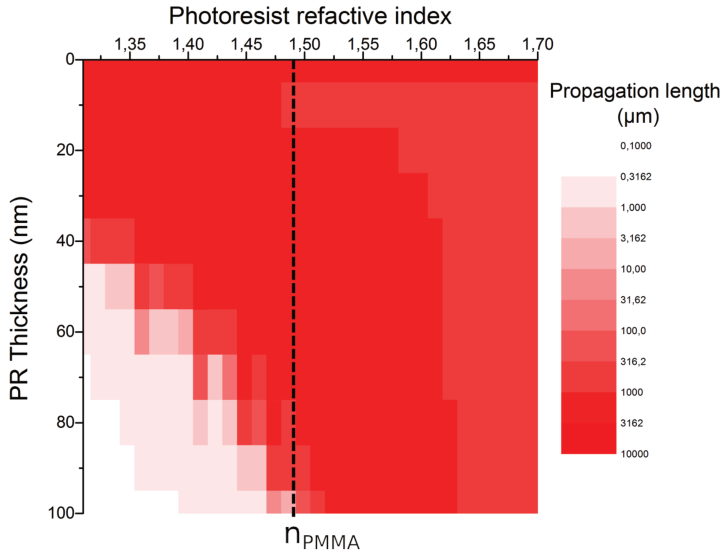

Figure II.10 – *Propagation length mapping of propagation length according to polymer refractive index on abscissa axis and polymer thickness on ordinate for a gold thickness of 20 nm covered by a variable layer of photoresist.*

In Figure II.11, the three colors represent three different behaviors. The high refractive indexes are represented by blue dots and blue lines, the propagation lengths decrease with increase of photoresist thickness. To obtain a ultra long range, the refractive index should not be higher than the cladding index.

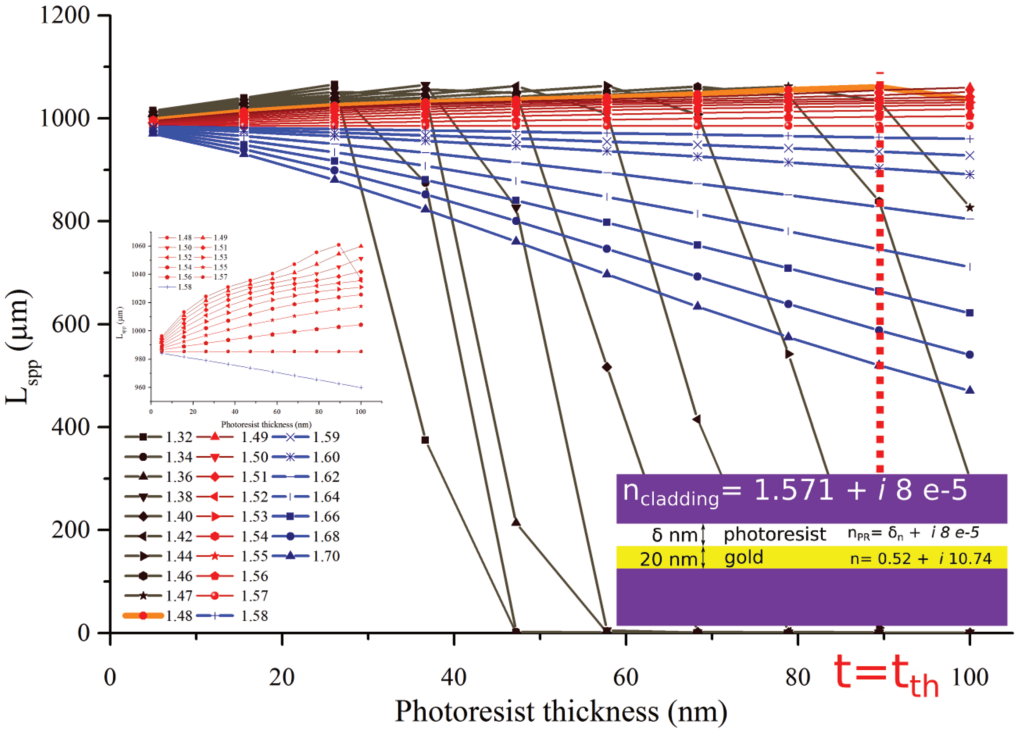

Figure II.11 *– Propagation length of ULR-SPP waveguide obtained by EIM method for different refractive index of polymer and polymer thicknesses and for a gold thickness of 20 nm. Insert: zoom in the best performing region for refractive between 1.458 and 1.57*

On the graph, we observe a phenomenon of threshold thickness (t_{th}) for the photoresist layer from which the propagation length decreases drastically, for example for PMMA (n_{PMMA}=1.48), the threshold thickness is about 90 nm. Above this threshold, the propagation length will start decreasing rapidly. In practice, the resist layer on top of gold is not useful for increasing L_{spp}, at least not in large proportions. However, in the etching step, this layer is used as an etch mask and can be difficult to remove, therefore the fabrication process is eased if this layer is left on top of the gold slab ($t < t_{th}$).

4 Simulation of the "gap" problem.

During the experimental sample characterization a problem of adherence of gold on polymer appeared. That is why, we studied the consequence of an air gap on the propagation length. The ULR-SPP consists of a 20 nm thick gold layer (n_{Au}=0.52 + i 10.81) covered by a 30 nm thick PMMA layer (n_{PMMA}=1.47). These two layers are embedded in two claddings considered as infinite half areas ($n_{cladding}$=1.571). So, in this structure, an air gap was introduced between the lower cladding and the gold layer. Its thickness was varied from 0 nm (no gap configuration) to 500 nm. (Figure II.12)

Figure II.12 indicates that an air gap of a few nm is sufficient to drastically reduce L_{spp}. This effect is already noticeable for a small air thickness in the ULR-SPP structure. For a good propagation length inside the ULR-SPP waveguide, there should be absolutely no gap to obtain an important length of surface plasmon.

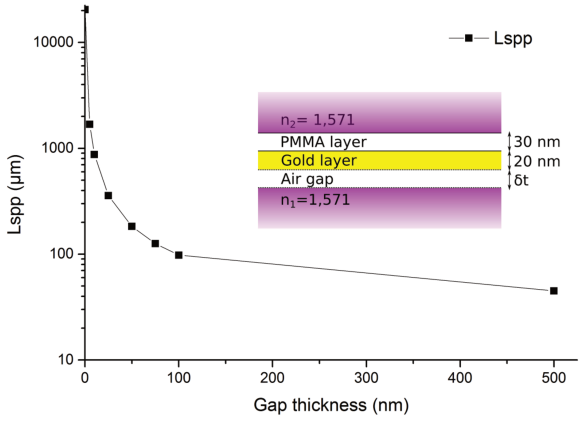

Figure II.12 *– Reduction of SPP propagation length with the extension of the air gap with logarithmic scale.*

Gap thickness (nm)	0	5	10	25	50	75	100	500
L_{spp} (μm)	20468	1686	874	358	183	126	98	45

Table II.4 *– Variation of SPP length according to the air gap thickness above gold waveguide.*

5 Conclusion of Chapter II

- The resolution by numerical method has been tested by two techniques : E.I.M. and F.E.M.
- The E.I.M. allows to discriminate the better condition of waveguide for optimizing the propagation losses
- These methods have been applied on 5 resins : FOWG-115, FOWG-116, Momentive, LIGHTLINK, PMMA
- We have shown the effect of an air gap inside our ULR-SPP structure. It appears that a very small thickness of air (∼5 nm) decreases the propagation length by 90%

Chapter III

Ultra Long-Range plasmonic (ULR-SPP) waveguides.

Contents

Introduction

Integrating a plasmon waveguide in a single component enabling light redirection with minimum loss represents a great challenge [76]. This work on LR-SPP waveguide benefits from long years of a great scientific effort [77, 78]. The characteristics of the ultra-long range mode can also be applied to the surface plasmon waveguides with finite width metal strips. The finite width plasmonic strip guides are known to support propagation distances longer than those of infinite width films. [41] There are two different ultra long-range structures: first a lower index dielectric layer embedded symmetrically on both metal sides : “s-ULR-SPP” or just the lower index layer on one side which gives an asymmetrical structure: “a-ULR-SPP” . During this work the a-ULR-SPP structure was studied because it is much easier to fabricate.

In the literature, there are various techniques to enable a bend configuration for long-range plasmon. These techniques are based either on an in-plane bend polymer waveguide [10] or on flexible characteristics which allow the bending of the waveguide out

of the waveguide plane. [54]

1 Concept of a SPP redirection waveguide component based on mirror integration

We propose a new plasmonic waveguide structure capable of redirecting light in a very low footprint compact but non-flexible chip. In this structure, light is guided and redirected in another fixed direction by specular reflection which is based on total internal reflection. This SPP mirror chip could be aligned and coupled with an optical PCB to redirect light towards an optochip. (represented in green in Figure III.1).

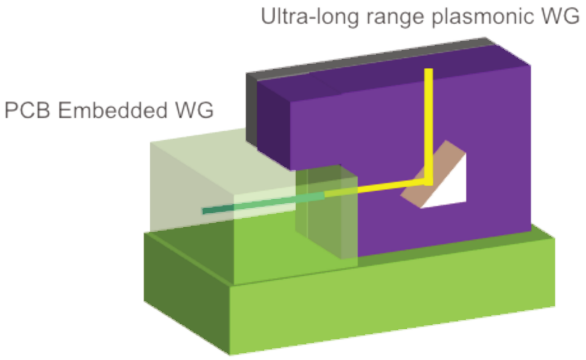

Figure III.1 *– 3D schematic of interconnection between plasmonic ULR-SPP and PCB embedded waveguides.*

Contrary to the plasmonic arc solution, the polymer/gold waveguide is rigid, residing on a silicon substrate. Light is guided via an Ultra-Long-Range Surface Plasmon Polariton mode (ULR-SPP) and reflected by a vertical polymer/air planar interface created by a prismatic cavity carved into the waveguide stack (illustrated in Figure III.2).

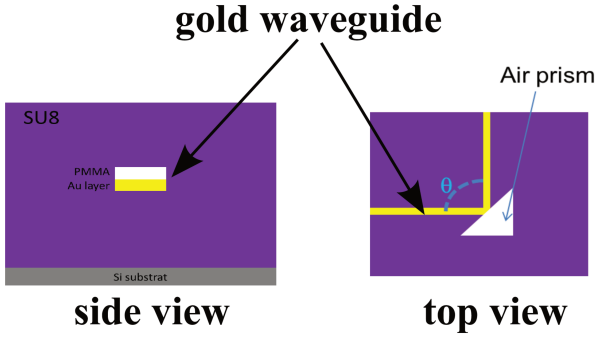

Figure III.2 *– Side view and top view of Ultra-Long range Surface Plasmon Polariton (ULR-SPP) rigid waveguide configuration*

In this chapter, the resin used as cladding resin is SU-8 polymer. The SU-8 is commer-

cialized by MicroChem Corp[1] [79]. It is a negative photo-sensitive resin known for the possibility of obtaining thick layers, it is easily processable by a UV-lithography and has a high stability, but it has a limited flexibility compared to polymers selected for plasmonic arcs (or flexible LR-SPPW). [80]

In practice the SPP mirror is obtained by carving a cavity in the whole layer stack of the LR-SPP or ULR-SPP structure, so that the refractive index of the air filled cavity is 1, allowing total internal reflection inside the layer. The SU-8 resist was chosen as dielectric cladding material because of its excellent properties and lithographic capabilities. In particular, obtaining a prismatic cavity of good quality, with nearly vertical developed walls is possible with this resist. This provides a good quality reflector for the SPP mode. Gold was used as the metal supporting the plasmon because it offers a good compromise between plasmonic properties and stability over time.

The proposed ULR-SPP waveguide structure consists of a silicon substrate, a lower polymer cladding layer, a thin gold strip covered with a PMMA strip made by UV lithography and etching, and an upper polymer cladding layer (shown in Figure III.2). The signal carried by the SPP along the waveguide can be reflected on-chip at any incident angle (chosen by design of the mask, and respecting the TIR angle condition) on the integrated air prismatic cavity.

2 Fabrication of SU-8 based ULR-SPP waveguides (without mirror)

In this section, the fabrication method for a straight waveguide without the mirror integration is presented. Both resists PMMA and AZ 701 MIR have been tested. At the beginning of our process, we deposited a 30 μm SU8-3035 resin film on a silicon wafer by spin coating at 3000 rpm, followed by a soft bake of 1 minute at 65 ^{o}C followed immediately by 9 minutes at 95 ^{o}C on a hot plate. This layer is exposed with a dose of 375 mJ/cm^2 in I-line configuration on SUSS MicroTec MJB4 lithography tool followed by a of hard bake of 5 minutes at 95 ^{o}C. (Figure III.3(a)). A 20 nm thick gold layer is thermally evaporated on this resin layer in Plassys MEB 400 evaporator with an evaporation rate less than 0.1 Å/s (Figure III.3(b)).

AZ 701 MIR is spun at 2000 rpm and baked at 100 ^{o}C on hot plate during 3 minutes. PMMA is spun at 7000 rpm and baked at 170 ^{o}C on hot plate during 5 minutes (Figure III.3(c)). The AZ 701 MIR layer is submitted to UV exposure performed at λ = 365 nm, with a dose of 95 mJ/cm^2. After a 70 second development in 726MIF solution, the AZ 701 MIR structure height is 100 nm as measured by profilometer. In this case of PMMA layer, the UV lithography is performed at λ = 250 nm, with an exposure dose of 1200 mJ/cm^2. After 45 second development in MIBK solution and 15 second in isopropanol solution, the developed structure has a height of 40 nm. (Figure III.3(d))

The gold layer is etched through the AZ 701 MIR mask (or PMMA mask) with a 20 sccm argon plasma sputter etch process performed on an Oxford Instruments Plasmalab 100 RIE-ICP 65 tool with 100 W RIE power and 250 W ICP power. (Figure III.3(e)). Then, the 30 μm-thick upper cladding polymer is spin-coated and exposed

[1] http://www.microchem.com/Prod-SU8_KMPR.htm

through the same mask with a 20 μm of lateral offset compared to the first SU8 layer. The lithography dose needed for cross-linking the 60 μm polymer thick layer is higher than the first exposure at 1200 mJ/cm^2 (Figure III.3(f)).

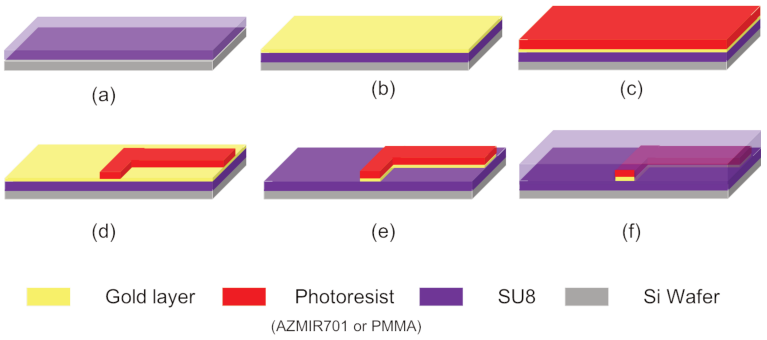

Figure III.3 *– Basic fabrication process of the SU8 ULR-SPP waveguides, without integrated SPP mirror.*

3 Integration of the prismatic cavity in ULR-SPP Redirected Waveguides (ULR-SPP-RW)

The integration of the prismatic cavity was the major hurdle of the fabrication process development. Two different approaches have been considered. The first one is to obtain the cavity by etching after the deposition of the top cladding. The second one consists in fabricating the cavity in two lithography steps, one for each cladding and correctly aligned together.

3.a SU-8 Deep RIE etching method

The problematic of the deep etch is to manage to etch down 60 μm of SU8 and obtain a vertical and smooth wall, which in RIE engineering terms translates into high selectivity (polymer to metal etch rate ratio) and high anisotropy. Many parameters are involved, including the metal chosen for the hard mask and all the RIE-ICP specific parameters of our Oxford Instruments tool (amongst them the nature of the etch gas mixture) having on selectivity, anisotropy and etch rate. From literature on this subject, which is not very extensive, we find that a mixture of oxygen and a fluorinated gas (SF_6 or CF_4) is recommended to etch SU8, sometimes additionally with argon.

In a preliminary study, the influence of the chosen metal (Ni, Cr Au and Ti were tested) and gas proportions (two mixtures CF_4/O_2 and SF_6/O_2 were tested) on the selectivity and SU8 etch rate has been observed.

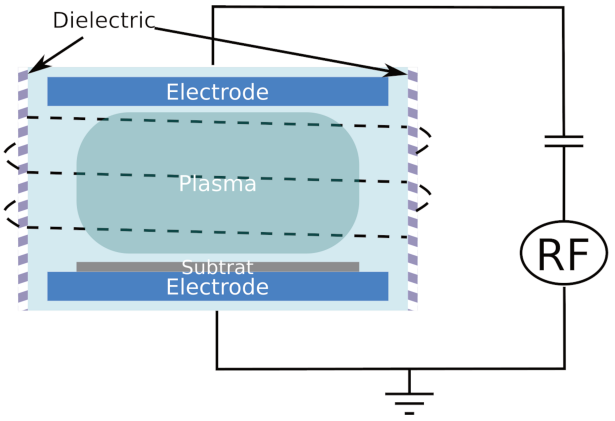

Figure III.4 – *Schematic representation of reactive-ion etching chamber.*

The temperature of the substrate was also varied between 0 and 20 ^{o}C, while all other parameters were fixed (RIE forward power = 200 W; pressure = 100 mTorr; ICP power = 0). The comparisons were made based on estimations of the SU8 etch rate and SU8/metal selectivity derived from profilometry measurements and SEM cross-section measurements. Out of 46 RIE runs the best process parameters were selected, being 1:10 SF_6/O_2 flow ratio and 4 ^{o}C temperature . This initial recipe was then used as basis for further optimization. The metal thickness will also have to be adjusted to reach 60 μm of SU8 etching, however it should be thin enough to limit surface tensions which could induce cracking, therefore a high selectivity between the metallic layer and the etched resin must be sought.

The list of parameters to be optimized is: SF_6 flow, O_2 flow, RIE power, ICP power, table temperature and chamber pressure. Other parameters, Helium backing pressure and flow are always fixed at the same values (Helium backing is used to improve thermal exchange between the temperature-regulated table and the sample).

The optimization is performed to obtain the following parameters: ∼100 nm nickel hard mask, O_2 flow = 22 sccm, SF_6 flow = 2 sccm, P_{RIE} = 20W, P_{ICP} = 400 W, pressure = 9.7 mTorr, table temperature = 10 ^{o}C. Figure III.5 shows typical results obtained after 20 min of etching.

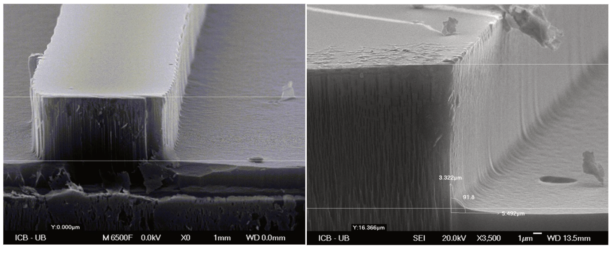

Figure III.5 – *Typical SEM images of the cleaved edge of RIE-etched samples. Etch time : 20 min, Etch depth : 3,3 µm. (test mask, the prism geometry will be used in fabricating the final device)*

We can observe that the anisotropy is very good, close to vertical, which is very promising. Some rugosity of the vertical surface is observed but its effect on the reflection efficiency of the SPP is unknown at this stage. Depending on the process parameters, some undercut

could be observed, up to 10 ^{o} difference with the vertical but most processes gave close to vertical profiles within a few degrees of angle. The absolute SU8 etch rate and the selectivity to nickel were found to vary significantly with the parametric changes.

Nevertheless the best run had a selectivity of about 400 and a SU8 etch rate of 700 nm/min which are promising values, implying that 150 to 200 nm of nickel thickness should be enough to etch the required 60 μm of SU8 in 1 to 2 hours etch time. With the employed nickel thickness, we have reached 19 μm etch depth. Another observed feature is some redeposition on the vertical walls as in the bottom image of Figure III.5, presenting some filamentous networks that often extend above the top of the layer, following the etching direction. This is an unexpected feature which has to be included in the parametric process optimization.

The RIE-ICP recipe might be further optimized by designing more advanced experiments. Also, in order to facilitate nickel deposition with a thickness between 150 and 200 nm, the change of e-beam evaporation process (by cathodic plasma PVD) could be envisaged. Nevertheless, confronted with the relatively poor quality of the surface that is supposed to act as a mirror in the redirection device, the double lithography method exposed in the next section was prioritized during the project.

3.b SU-8 Double lithography method

We developed the double lithography method to ensure perfect (error-free) alignement of the vertical planes of the two resist layers constituting the mirror face of the prism (its hypotenuse), and this is achieved without any mechanical alignment step, which would usually result in a $\sim \pm 0.5$ μm registration error between the two lithographies. (Figure III.7).

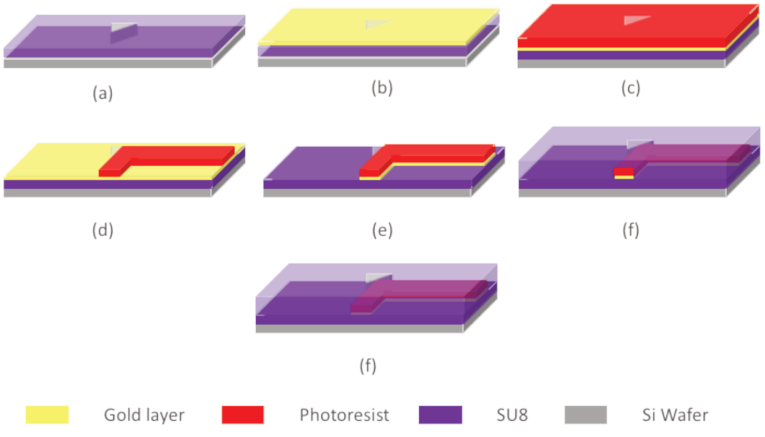

Figure III.6 – *Double lithography process applied for ULR-SPP*

In this double lithography process, each cladding receives a prism-shaped latent pattern which will be developed at the end of both lithography steps. This second process is easier to realize and has a reduced number of process steps compared to section 2. (shown in Figure III.6)

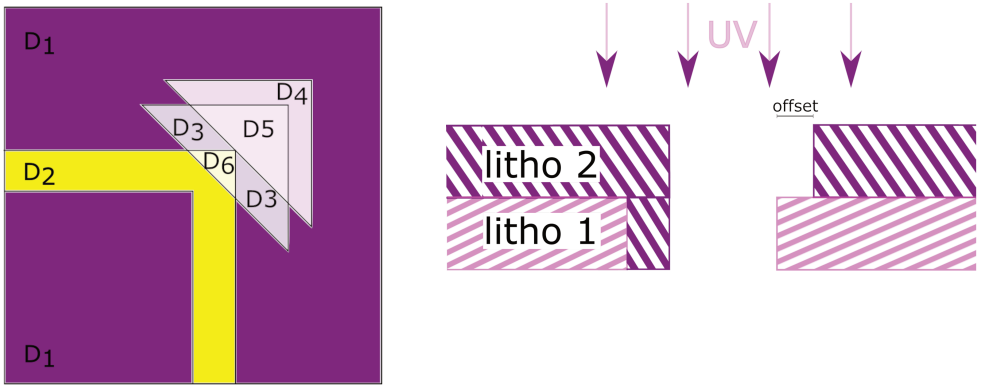

(a) Lithography dose received by each area

(b) Cross-section of the double lithography area after final development

Figure III.7 *– Cross linking on double resin layer*

The first layer of SU8 is exposed with a clear-field mask using a dose of 400 mJ/cm^2 to predefine the areas that will be crosslinked in this bottom layer and the areas that will need to be developed later (Zone D1 and D4 of Figure III.7). It is reminded here that SU8 is a negative tone resist and that development will remove the unexposed parts. Then a layer of gold is evaporated covering all areas. A layer of photoresist is then spin-coated and UV-exposed with a mask in which the guide structures (D2+D6) are slightly overlapping the prismatic area already defined (by approximately 10 μm => Area D6 in Figure III.7). Afterwards, a gold etch step is necessary to define the waveguides. Finally the second layer of SU8 is deposited. The lithography is done with the same mask as for the first layer of SU8 but now perfectly aligned with the corner of the gold waveguide turn. In this alignment step, attention is paid to the fact that the masking areas of the prisms must be exactly tangent at the corner of the turning waveguide. (shown in Figure III.8). This creates an overlap region (D3) of the two litho steps that will finally remain undissolved after development. In the end the areas developed will be D5 for both layers plus D4 for the top layer.

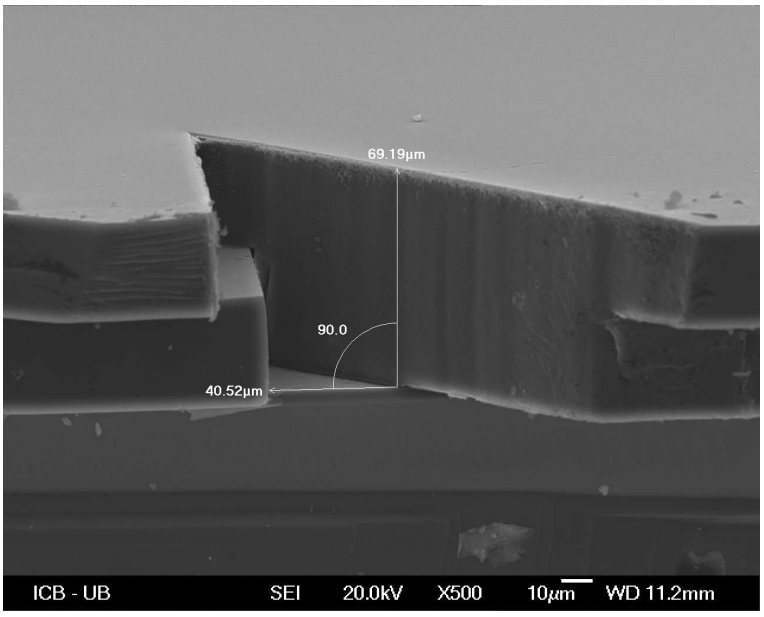

Figure III.8 *– Face of reflection by the corner of air after development*

3.b.1 Attempts with other resists (AZ40XT, BCB)

Other polymers (including AZ-40XT and Dow Cyclotene^{TM} 3022-35) have been considered as cladding polymers. For each polymer, the same fabrication process explained in Figure III.3 has been followed, but after the photoresist development step (Figure III.3 (d)), surface tensions appear in the photoresist layer, preventing the correct etching of the metal layer. Manufacturing tests with these two polymers weren't satisfactory, thus the use of SU8 was favored.

4 Optical characterization of ULR-SPPW in the straight configuration

In this part, we report on the optical characterization of the cleaved samples excited by end-fire coupling with a single-mode fiber. Two characterization methods are used : SPP imaging to measure the profile of the mode and the power attenuation measurements on waveguides of different lengths ($\sim$ cut-back method).

Our Optical setup is composed of an IR source (Anritsu, OSICSExternal-Cavity-Lasers emitting at 1550 nm) with fiber output, a 3-paddle polarization fiber controller, one single mode fiber (SMF 128), the sample and an IR Xenics camera, model Bobcat 320-Star (shown in Figure III.9). The waveguide samples were supported by silicon and cleaved to produce the facets for butt coupling. Characterization was done at 1550 nm wavelength with TM polarization control.

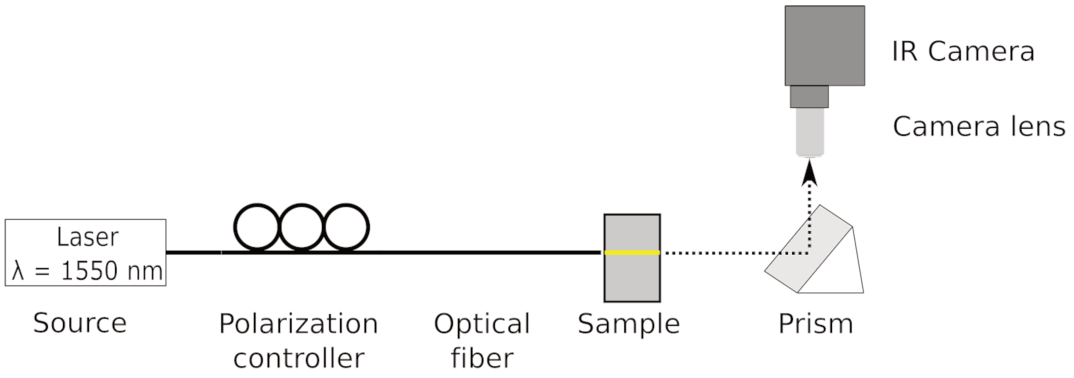

Figure III.9 *– Optical setup used to acquire the imaging mode.*

4.a SPP mode imaging

The width of the SPP mode was measured at the output of the waveguide by displacing the collecting fiber in both directions perpendicular to the waveguide. A Gaussian shape was observed with ∼10 μm mode width.

Figure III.10 shows the IR images of the ULR-SPPW FWHM plasmon mode using SU-8 polymer at the output of the waveguide for varied waveguide widths and simulations. This comparison shows that the obtained mode is less wide than in the numerical simulation.

Width (μm)	Long. Mode FWHM (theo)	Long. Mode FWHM (exp.)	Trans. Mode FWHM (theo)	Trans. mode FWHM (exp.)
5.0	5 μm	5.8 μm	4 μm	3.3 μm
7.5	7.3 μm	6 μm	3,6 μm	4.1 μm
10.0	8.1 μm	6.5 μm	3 μm	5 μm
12.5	8.5 μm	8.7 μm	4.2 μm	5,1 μm

Table III.1 *– Dimension of FWHM of output mode for Au-ULR-SPPW.*

4.b Loss measurements and cut-back method

The plasmonic mode losses in TM are plotted in Figure III.11 for varied waveguide widths. The propagation loss lies in the 0.6 to 1.2 dB/mm range and the coupling loss between 5 and 14 dB (for input + output facets). We obtain large coupling losses compared to the LR-SPP waveguides, where the coupling losses are estimated to be around 3 dB with the cleaving method.

Initial characterization of the propagation losses of the ULR-SPP waveguides has been performed by J.C. Weeber at ICB laboratory in the simpler straight waveguide configuration. The fabrication details of the tested samples are contained in the next section, limited to steps **(a)** to **(f)** of Figure III.3 and the stack is shown in Figure III.2. The total SU8 thickness was about 60 μm. Straight waveguides of various widths (2.5 to 12.5 μm by 2.5 μm steps) were tested.

By applying a cut-back measurement procedure, the measurements showed on Fig-

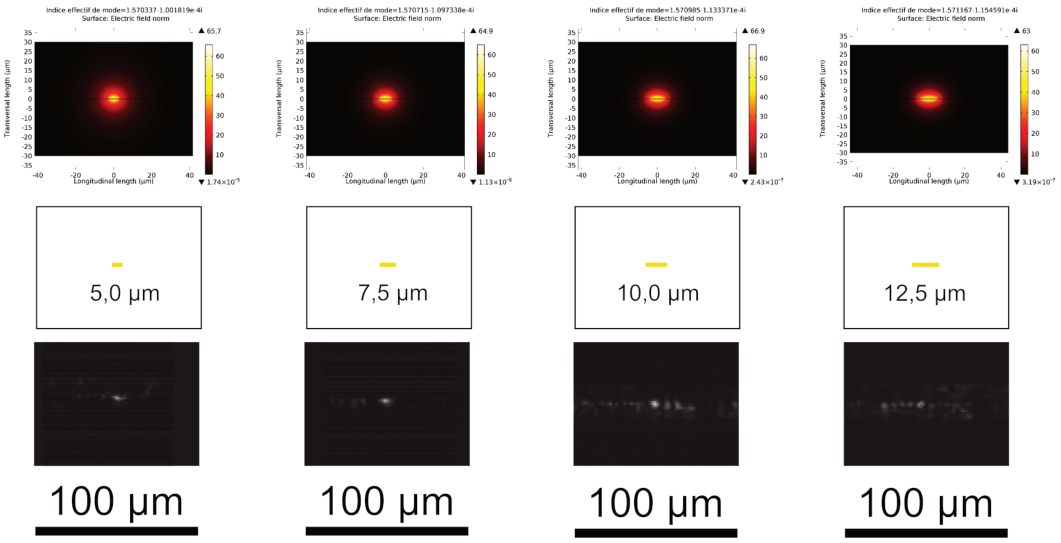

Figure III.10 *– Au-ULR-SPPW. 1.55 µm imaging of output mode of ∼1 cm long sample (**bottom :** experimental; **middle :** design; **top :** simulations).*

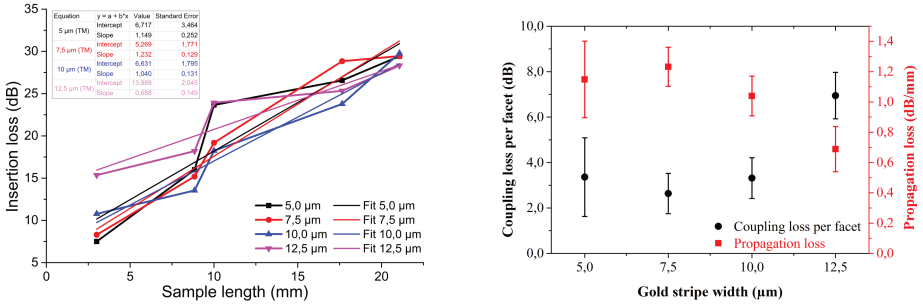

(a) *(b)*

Figure III.11 *– Au-ULR-SPPW : Cut-back method.*

ure III.11 that the loss was minimal for the 7.5 μm wide waveguides and gave a coupling loss of about 1.5 dB/facet, an insertion loss of ∼15 dB on 1 cm long waveguides and the propagation loss was about 1 dB/mm.

Figure III.11 (B) shows an important variation of the coupling loss measurements. The values vary between 2.5 and 7 dB. The best coupling loss value, 2.63 dB, appears to be for the 7.5 μm waveguide. The figure states also that there is a significant oscillation in propagation loss, between 0.6 and 1.2 dB. The best value of propagation loss, 0.69 dB/mm, would be for the 12.5 μm large waveguide.

We can compare our results to those reported by Huang & al. [81], where SU-8 LR-SPP waveguides have propagation loss in the range 1.9-3.9 dB/mm at 1550 nm, slightly higher values than ours.

5 Optical characterization of the SPP redirection waveguide component

In this section, we explore the possibility of observing the plasmonic mode after a reflection on the air prism. (Illustrated on Figure III.12)

we observe that the mode is splitted in the two resin layers. In

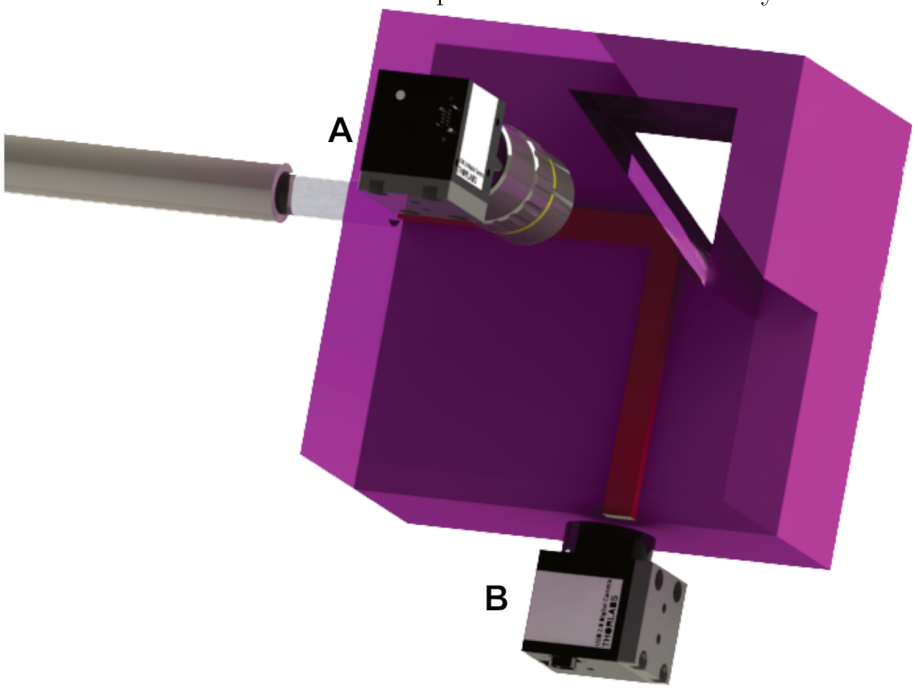

Figure III.12 *– Observation of reflection of the plasmonic mode on air prism.* ***A :*** *in top-view configuration,* ***B :*** *in output mode view.*

SPP mode imaging

We have tried to characterize our cleaved sample with the IR-camera placed in top viewing position above the waveguides, and two single mode fibers “SMF 28”, in butt coupling configuration. Before reflection on the air prism, we obtain 2 dB/mm of propagation loss in TM mode, obtained by cut-back method seen in the previous section. After reflection on the air prism the propagation loss is 2.9 dB/mm determined also by cut-back method (Figure III.13). In the absence of the air prism, we see that the SPP is not redirected. (Figure III.14)

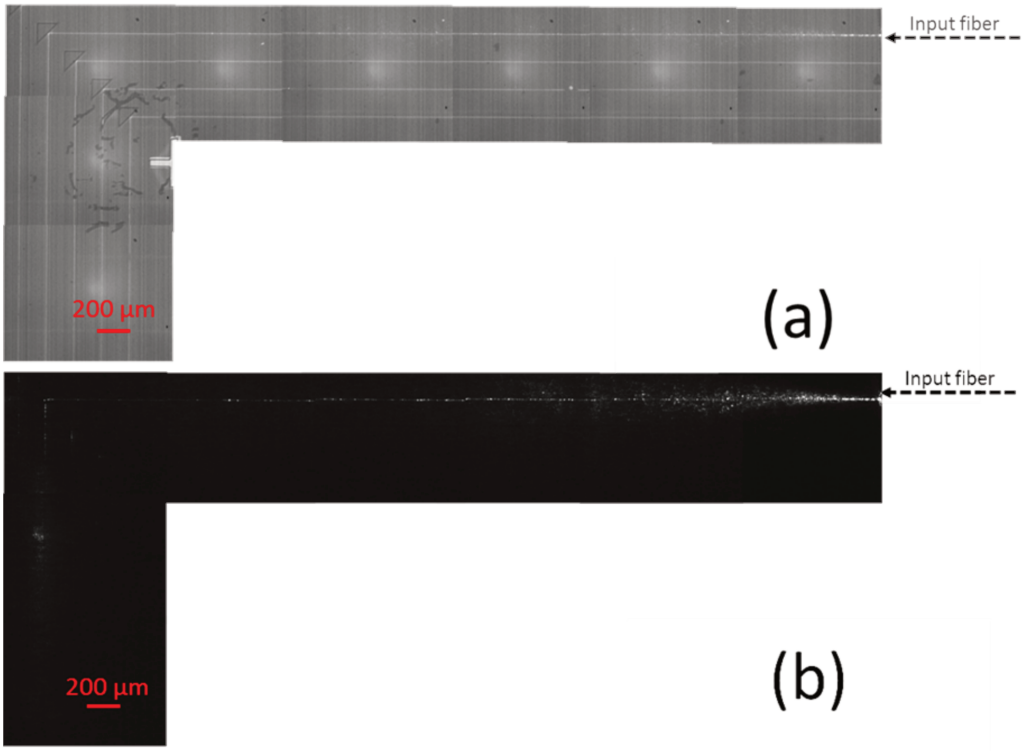

Figure III.13 *– IR image along a 5 µm-waveguide for a wavelength of 1550 nm with input power of 5 mW and camera integration time of 300µs (input edge) (magnification x5) with microscope light. (a) With diffuse light (b) With just IR detection.*

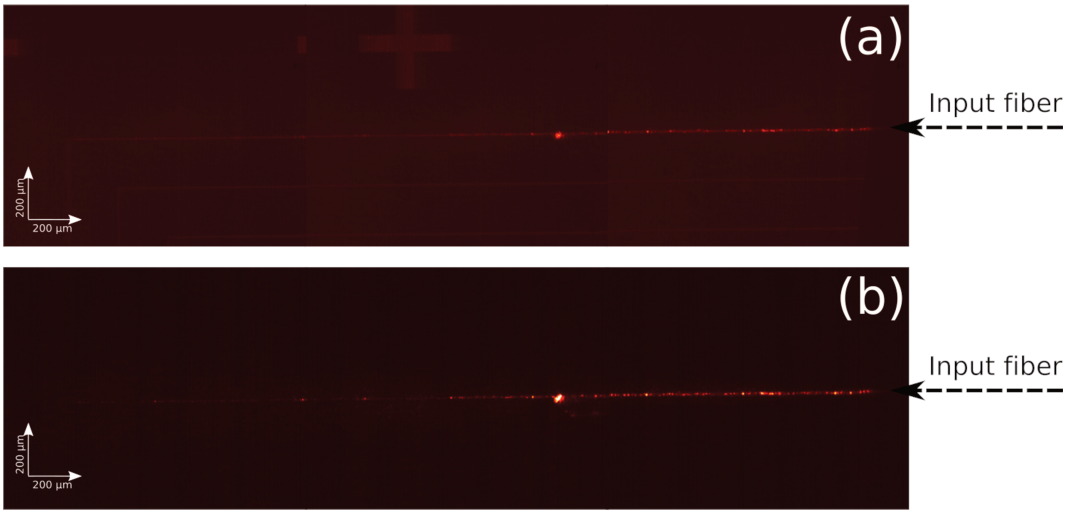

Figure III.14 *– IR image top view, without prism. (a) With diffuse light (b) With just IR detection.*

When the IR camera is placed in front of the waveguide end (output mode observation configuration) we observe that the mode is splitted in the two resin layers. In addition, the plasmon is not confined close to the gold waveguide but it is distributed along the sample facet. This disappointing result makes it difficult to further exploit this component. (Figure III.15)

Figure III.15 *– Mode observed after reflection on air prism with input power of 5 mW and camera integration time of 300 µs (input edge) (magnification x5).*

6 Conclusion of Chapter III

- We have successfully developed an UV-lithography based technique for obtaining a flat integrated SPP mirror based on a double lithography method. This technique allows creating a nicely smooth and vertical prismatic structure through the thick double SU8 resin layers.
- A sample was obtained and characterized. On this sample, the plasmon reflection on the air mirror has been observed but a poorly confined mode is observed at the output.
- The lack of good results from this study can be attributed to different fabrication components like the photoresist which is not perfectly resistant to the sputter etching step, it appeared that the plasmon was very diffusive on straight waveguides. The etching recipe should be revised for this reason. In view of these unsatisfactory results and time constraints, the development of the Ultra Long Range structures was halted to return to a less complex configuration, namely the plasmonic arc waveguides presented in the next chapter which were the main goal within PhoxTroT.

Chapter IV

Long-Range plasmonic (LR-SPP) waveguides.

Contents

Introduction

In this chapter, we first examine the characteristic properties of the polymers used for LR waveguide for out-of-plane bending configuration. We report on the identification of 3 different suitable polymer materials and the fabrication of the plasmonic arcs, which can be defined as free-standing mechanically flexible waveguides that support the long-range surface plasmon polariton mode (LR-SPP) and that are used as optical interconnect.

The optical characterization of the stand-alone LR-SPP waveguides in the straight (unbent) configuration is then presented. The bending of the waveguides and the associated bending losses are reported in sections 4 and 5. The bending losses characterization has been performed by our PhoxTroT partner SDU with the samples we have fabricated. In this chapter the coupling of LR-SPP waveguides with single mode glass waveguides is also reported in section 6. The optical Printed Circuit Board (oPCB) samples containing the glass waveguides were provided by our partner Fraunhofer IZM.

1 Polymer films for flexible LR-SPPW.

1.a Specifications and choice of the polymer materials

There are basic requirements for a polymer material to be used in a flexible LR-SPPW structure. It should easily form homogeneous films (using spin-coating); these films should be flexible; have good stability (mechanical and thermal); give the possibility to tune precisely the refractive index in order to fabricate the multiple-cladding structures; they should give low loss waveguides at 1550 nm Telecom wavelength even in the bent configuration and finally be compatible with the various fabrication process steps, and in particular provide good adhesion to gold both at the fabrication stage and later under bending stress. These requirements lead us to the following list of the main material's properties:

- Thermal and mechanical stability

  ⇒ cross-linkable polymer (cross-linking can be generated either by UV curing and/or thermal curing)

- Flexibility (bending radius down to 1 mm)

  ⇒ preferably elastomers

- Low loss at 1550 nm

  ⇒ low intrinsic absorption, preferably below 1 dB/cm

  ⇒ microscopic homogeneity in the films (no voids or varied density) especially in terms of refractive index

- Refractive index tunability

  ⇒ provider should propose various grades of materials with different refractive index

- Adhesion to gold (with or without bending stress)

  ⇒ losses could result from the presence of air gaps between polymer and gold in the waveguide. Adhesion should also be assured during bending of the waveguide

The stability, flexibility and low loss requirements make transparent elastomers like silicones (polysiloxanes) or other types of elastomers the materials with the best potential. Exguide FOWG is an ethylene-oxide-acrylate based elastomer including fluorinated styrene groups and it was initially identified before submitting the project. It is the most evident choice because of the good optical transmission [54] in the bent configuration showed in published results. Table IV.1 is listing some commercially available polymers

commonly used in photonics and an appreciation of their performances with respect to our main requirements.

Material	Polymer type	Thermal stability	Flexibility and integrity of ~20-40 μm film	n at 1.55 μm	Loss in dB/cm at λ=1.55µm	
					Single-mode polymer waveguide	LR-SPPW
PMMA	acrylate	85°C	low	1.49	0.6 [82]	-
SU-8	epoxy novolak	>200°C	high	1.57	0.48 [83]	5
BCB	benzocyclobutene	350°C	low	1.535	1.5 [84]	6 - 8 [58]
PDMS	siloxane	n.a.	high	1.396	-	-
ORMOCER	organic/inorganic hybrid silicone	270°C	medium	1.52—1.538 from [85]	0.75 – 0.8 [85, 86]	-
EPO CORE/CLAD	epoxy	230°C	-	1.575 / 1.563	2.23 [87]	-
Exguide ZPU / LFR	fluorinated acrylate	300°C [1]	-	1.43 / 1.46	0.35 [88]	1.4 [89]
Exguide FOWG	acrylate –co-ethylene oxide	280°C	high	1.506—1.547	-	32
LIGHTLINK	silsesquioxane	high	high	1.473	1.36 [87]	3 – 10
MPM526A&B	epoxy	200°C	high	1.41—1.47	-	5 – 12

Table IV.1 *– Possible commercial materials and important parameters for the flexible plasmonic Arc. Colored blocks refer to the results obtained in this work.*

Looking at table IV.1, standard PMMA has to be ruled out due to poor thermal resistance. SU8 and BCB have the disadvantage of having limited flexibility, with their elasticity modulus lying in the 2-4 GPa range (Table IV.2). In addition, their absorption loss is relatively high compared to other polymers. Ormocer could be an interesting alternative to FOWG. PDMS is also an option but problems of adhesion to gold have been reported [90, 91] and it possesses an absorption band at λ_{TC} [92]. MPM526A&B, LIGHTLINK are good polymers for a flexible waveguide, with a low absorption loss at 1550 nm.

Polymer material	Elastic Modulus (flexural; tensile)
PMMA	3 GPa ; 3 GPa
SU-8	n.a. ; 2-4 GPa
BCB	n.a. ; 2.9 GPa
PDMS	n.a. ; 0.3-0.9 MPa
ORMOCER	n.a. ; 70-4500 GPa
EPO CORE/CLAD	n.a. ; 2.4/2.2 GPa
Exguide ZPU / LFR	n.a. ; n.a.
Exguide FOWG	n.a. ; n.a.
LIGHTLINK	n.a. ; n.a.
MPM526A&B	n.a. ; n.a.

Table IV.2 *– Elastic Modulus of commercially available materials.*

Thus FOWG, MPM526A&B and LightLink were the 3 materials studied. We started with FOWG for the development of the LR-SPPWs because of its performances reported by the Korean group who used it in the long-range SPP waveguide configuration but also because it was commercially available at the beginning of this project.

The flexibility of FOWG waveguide is shown on Figure IV.1, where metal strips can be seen embedded in the flexible film.

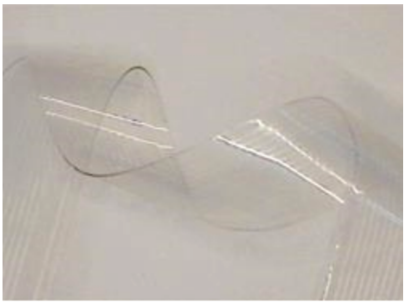

Figure IV.1 – *Illustration of the FOWG resin layer flexibility (reprint from [1])*

The Figure IV.2 shows the refractive index of various resins. The straight curve has been calculated from the Cauchy model, and the data points (dots) have been extracted from the data sheets of each resin.

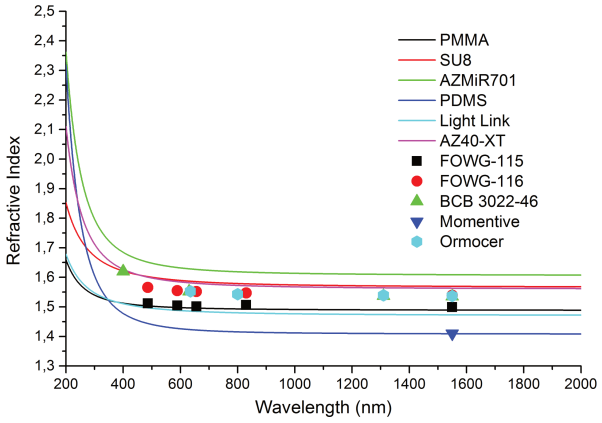

Figure IV.2 – *Refractive index of FOWG, SU8, PMMA, BCB, PDMS, AZ 701 MIR, LIGHTLINK, Momentive, AZ 40-XT and Ormocer resins.*

1.b Film fabrication

1.b.1 FOWG

FOWG was supplied by ChemOptics Inc. (Korea) in two different grades: FOWG-115 and FOWG-116. Each grade has a specific refractive index, as indicated in the table IV.3 [1]. Although results were published by the korean group on the fabrication and characterization of FOWG-gold LR-SPP waveguides, we realized that these articles did not contain the relevant data necessary for fabrication. They only gave a general overview of the processing with few details. The processing guidelines provided by the manufacturer are the following:

- Spin Coating $\longrightarrow$ UV Curing (2500mJ/cm^3) under N_2 $\longrightarrow$ Baking (160$\sim$200^{o}C/30 min).

- Use diffusive light from a broad-band UV source instead of collimated light to cross-link the film.

This limited information gives no indication for a precise thickness and the reason for the use of diffusive light is unclear. During this work, it was thus necessary to learn how to process the resin itself and how to fabricate the waveguides from the FOWG films. Table IV.3 regroups the characteristics of two FOWG-grades. For liquid and film states, the two grades have similar performances. Differences can be seen for refractive index and degradation temperature. Table IV.4 gives refractive index data provided by the manufacturer.

Exguide		FOWG-116	FOWG-115
Liquid	Viscosity(cps @ 25 ^{o}C)	$40 \sim 120$	
	UV-exposure(under N_2)	$> 1\ 400$ mJ/cm^2 (160^{o}C/30 min, post baking)	
Film	Propagation Loss$^+$(dB/cm)	<0.1 dB/cm @ 0.83 μm	
	Refractive Index @ 0.83 μm	1.547	1.506
	Birefringence(n_{TE} - n_{TM})	<0.0001	
	Linear shrinkage(solid to solid)	< 5 %	
	Glass Transition Temp.(Tg)	$30 \sim 50^o$C	
	Degradation Temp.(1 Wt%)	280 $\pm$ 20^{o}C	270 $\pm$ 20^{o}C

Table IV.3 *– Resin data given by ChemOptics*

λ (nm)	Optical index for FOWG-115	Optical index for FOWG-116
486	1.5116	1.5660
589	1.5047	1.5551
656	1.5014	1.5520
830	1.5064	1.5471
1550	1.4996	1.5390

Table IV.4 *– Refractive index of resins FOWG-115 and FOWG-116 at different wavelengths in films form provided by ChemOptics*

We first did spin-coating tests. Table IV.5 shows the FOWG thickness obtained for a range of speed. Afterwards, the spin speed is fixed at 700 rpm, which is a good compromise to get both a thickness of 30 μm and a homogeneous surface.

Spin coat speed (rpm)	700	800	900	1000	1500	2000
Polymer thickness (μm)	35	25	13	8	5	3

Table IV.5 *– Polymer thickness of FOWG-115 versus spin coat speed*

The cross-linking has to be performed in an inert atmosphere. Chemoptics does not provide chemical information on the resin but we can suppose that the reason for this important detail is the sensitivity to oxygen of the chemical groups formed under UV exposure. In air, a surface inhibition layer due to oxidation could be formed, leading to localized refractive index variations. This can be avoided by using an inert atmosphere.

Various conditions have been tested in order to obtain a resistant cross-linked FOWG film: exposure in normal atmosphere with a mask aligner (collimated light), with or without nitrogen blanket flow over the sample, versus exposure in an Argon glove box (O_2 < 1 ppm) with a portable diffusive UV light source; post-baking in normal atmosphere versus post-baking in the Argon glove box. To control the results of these series of tests, we have measured the resistance of the samples to process chemicals, e.g. solvents like N-methyl pyrrolidone (NMP), acetone (from ambient temperature to 60^{o}C on a hot plate), as well as Buffered Oxide Etchant (BOE) and photoresist developers, with the purpose to find the right chemical to get a film withstanding all the waveguide processing steps. These resistance tests simply consisted in dipping the sample in the solvent and watching its decomposition over time at fixed time intervals. The exposure and baking of FOWG in inert atmosphere was necessary to get a good quality fully cross-linked film with good resistance to solvents (see Figure IV.3). The effect of diffusive light (as recommended by chemoptics) versus collimated light (as produced in our mask aligner) remains unclear as it was not possible to use the mask aligner in the glove box and because the nitrogen flow in the mask aligner does not provide enough deprivation of oxygen (Figure IV.3).

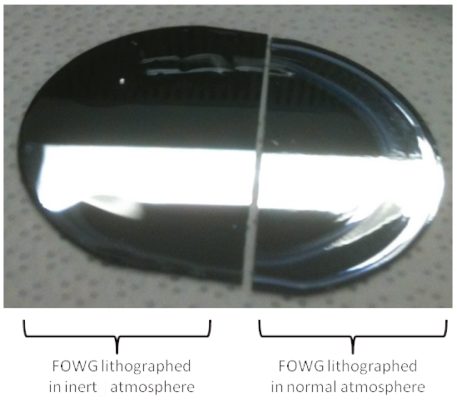

Figure IV.3 *– FOWG film processed in inert versus normal atmosphere.*

The chosen exposure conditions for FOWG-115 was an UV exposure with a UV dose of 6500 mJ/cm^2 using a diffusive UV gun and a hard bake, both steps performed under Argon atmosphere. The dose may differ from manufacturer's recommendations due to the difference of used detector. The tested hard bake temperatures were T=165 ^{o}C, 170 ^{o}C, 180 ^{o}C, 190 ^{o}C. The tests of resistance to solvents (NMP, acetone) were performed from ambient temperature to 60 ^{o}C. A much higher resistance was observed in the chosen conditions compared to the test with the mask aligner outside the glovebox. Moreover, the Argon-protected samples do not present surface irregularities at substrate peripheries.This confirms again the necessity of cross-linking under inert atmosphere. The FOWG films were then submitted to longer resistance tests. After 20min in acetone, the film starts to lift from the substrate. The chemical that did not affect FOWG films at longer times was diluted photoresist developer AZ 400K (a diluted KOH solution).

1.b.2 Momentive

Momentive Performance Materials GmbH kindly provided us with two research-grade epoxy-type materials having different refractive indices (MPM526A&B) allowing tuning

the refractive index by blending the two materials in different ratios. Both materials were of the UV+Thermal or thermal cure type and the company also provided us with the photoinitiators adapted to the 365 nm wavelength. The polymer and photoinitiator were mixed in the recommended proportions just before use (kept less than 48 hours in the clean room to avoid any evolution of the mixture) in the clean room away from sunlight. The mixtures were spin-coated on silicon wafers that were covered with an adhesion promoter beforehand. Two different polymerization conditions have been tested, only thermal or UV+thermal. We found out that the best conditions to obtain a hard and smooth coating was a 30 s UV flood exposure in our MJB4 mask aligner, immediately followed by a 120^{o}C baking for 5 min. Nice homogeneous and resistant flexible films were obtained. The thickness ranges were different for the prepared material compositions. To obtain the desired thicknesses, the spin -coating spin speed was adjusted and in the cases where a single coating was too thin, double layers of the same were realized.

1.b.3 Lightlink

We chose to use the grade "XH-100145" because of its simpler thermal cure process. Lightlink films are easily formed on the Si wafers by spin coating (1500 rpm $\longrightarrow$ 5 μm thickness) followed by a first baking step at 90^{o}C for 5 min and a second bake at 160^{o}C for 15 min. Multiple layers can be topped up onto each other following the same process in order to reach the desired cladding thickness.

1.b.4 Conclusion on polymer choice

To conclude on the fabrication of the polymer films, FOWG suffers from a more complex fabrication procedure than the other polymers, because of the difficult and time-consuming constraint of UV-exposing and baking under inert atmosphere, inside a glove box. This makes its use difficult in practice in comparison with Momentive and Lightlink polymers which are easier to process and were preferred for the production of the LR-SPPW waveguides towards the end of the project.

1.c Film peeling and flexibility

Polymer films are deposited on a silicon substrate. In order to obtain the final flexible waveguide structure, it is necessary to peel off the waveguide from the silicon substrate. As shown in Figure IV.4, a 30 nm gold layer was deposited on the substrate prior to resin coating (Figure IV.4(a)) to facilitate the separation of the resin from the substrate without damaging the film. The peeling off can be realized successfully (Figure IV.4(b)), due to the expected flexibility of the film but the film is fragile and can be easily torn during peeling. A successful peeling depends on the thickness of the gold underlayer.

An alternative solution we found is to deposit FOWG on a silicon wafer coated with TI-prime adhesion promoter (in place of gold) and peel off the film using hot isopropanol. Momentive films also peel off easily in the same conditions as those described for FOWG.

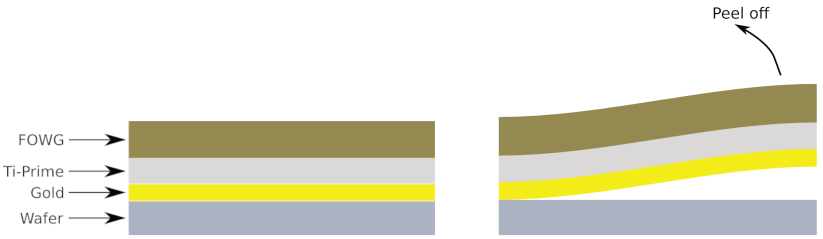

(a) polymer on original substrate *(b) peeling of polymer layer*

Figure IV.4 *– Stack for FOWG film peeling test.*

2 LR-SPPW fabrication method development

Figure IV.5 shows a general sketch of the LR-SPP design studied during this thesis. The pitch was fixed to 100 μm and different values of width and thickness of the metal strip were tested.

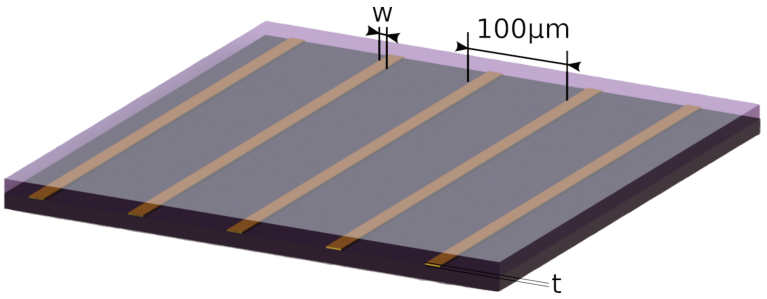

Figure IV.5 *– Scheme of long range surface plasmon sample in straight configuration.*

Several fabrication methods have been tested. Firstly, a stacking up method was used, where all layers were added on top of the previous ones and secondly a top and bottom cladding assembly method where the top and bottom polymer cladding are assembled after the fabrication of the gold waveguide. The different methods tested for the FOWG polymer are presented in sections 2.b to 2.d.

For the fabrication of the gold waveguide situated between the two polymer claddings, two different approaches have been considered: a lift-off process or a plasma etching process. Even though the etching option has a lower number of process steps, the lift-off process has been favored initially because it gave better results on claddings made of the first 2 polymer materials tested in this project, FOWG and BCB. The retained lift-off approach used for FOWG is presented in subsection 2.b. The methods presented in the following subsections 2.c and 2.d were developed only to try and address the mitigated waveguide loss performances of the LR-SPPW fabricated with this polymer.

The influence of metal thickness "t" was not experimentally studied in this work. Based on simulations, we know that decreasing the thickness is very effective in reducing the propagation losses. However, there is a limit to that decrease, which is called percolation limit. It is represented by the value, below which the metal layer would not be homogeneous and would induce additional scattering loss. The thickness was between

15 and 20 nm in all samples.

Finally the fabrication of the LR-SPPW based on the two new polymers Momentive and Lightlink is presented in section 2.e, the method that led to the best performing waveguides in this work.

2.a Stacking up method, Plasma etching option (FOWG)

The plasma etch process flow is described in Figure IV.6. After depositing the first cladding (FOWG or BCB), 15-20 nm gold was thermally evaporated. Photoresist PMMA was deposited on top and exposed through the mask in the UV mask aligner at 250 nm wavelength. After development, Argon plasma sputter etching was performed in the Oxford Plasmalab RIE etching system for 30 sec, with an etch speed of about 1 nm/s . Important surface modification of the FOWG polymer was observed as a result of the exposure to plasma (skin effect due to heating and ion bombardment). This prevented us from finalizing this procedure and we chose to concentrate on the lift-off process, a less aggressive process for the polymer cladding.

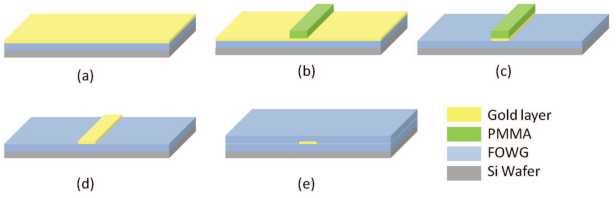

Figure IV.6 *– Fabrication process flow base on the plasma etching of gold.*

The same problem occurred when BCB resin is used as cladding polymer. During the photoresist lift-off step, cracks appear on the gold layer and a surface stresses are visible. (shown in Figure IV.7)

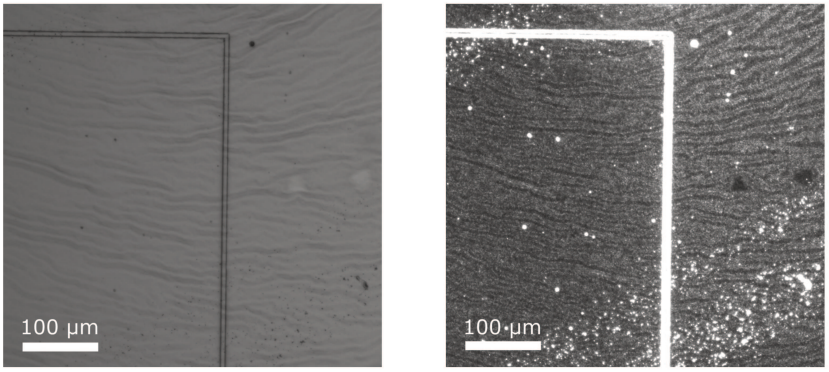

(a) *on bright field view* ***(b)*** *on dark field view*

Figure IV.7 *– Surface of BCB Sample after the photoresist lift-off*

2.b Stacking up method, Lift-off option (FOWG)

The simpler lift-off process flow is shown in Figure IV.8. Basically a photoresist mask is fabricated on top of the bottom polymer cladding, then the metal is deposited (by thermal evaporation) and lift-off is realized by dissolution of the photoresist mask in the appropriate solvent, before the final deposition of the top polymer cladding.

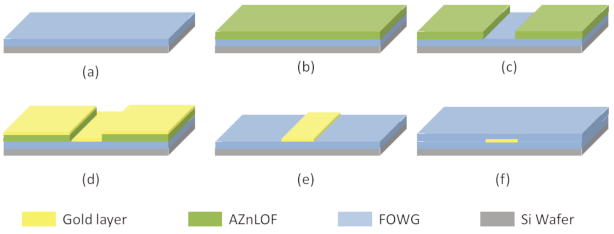

Figure IV.8 *– Basic Lift off process flow for the LR-SPP structure*

This process can be refined by the addition of a protection layer on top of the polymer (between steps a and b), a sacrificial layer which protects the polymer cladding during the following steps but that is finally removed in part before the deposition of the metal and in part after the lift-off step (e). In a first attempt lift-off was done on FOWG without a sacrificial layer, as in Figure IV.8. The lift-off resist we have chosen was AZnLOF, a well-proven lift-off photoresist and we used an existing established procedure used in our lab. Unfortunately this attempt failed due to a poor lift-off performance, with the results after step (e) shown in Figure IV.9.

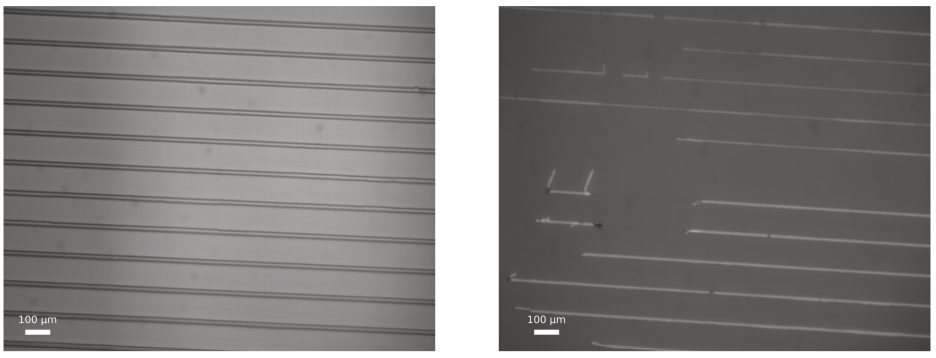

(a) *before Lift-Off* ***(b)*** *after Lift-Off*

Figure IV.9 *– Surface state obtained after a short exposition of solvent during lift off.*

To circumvent these lift-off difficulties, a very thin sacrificial layer, which can be either SiOx or SiNx, is added between the FOWG film and the photoresist. Lift-off with a SiNx sacrificial layer was the method used by the Korean group to fabricate their flexible LR-SPP waveguides based on FOWG polymer. The fabrication process flow we have developed is schematized in Figure IV.10 and was initially inspired from Jin Tae Kim's paper [93] which was referring to ZPU450 coatings, and not FOWG. However they mentioned that a similar process could be employed for FOWG [88]. Throughout this work AZnLOF was used as photoresist was and SiOx as sacrificial layer.

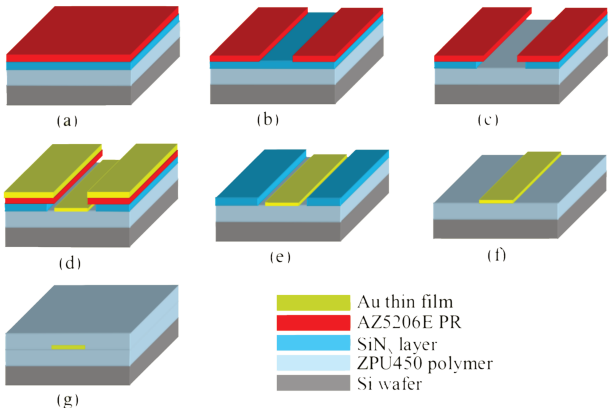

Figure IV.10 *– Schematic process of the waveguide based on lift-off for ZPU450 polymer. (Extracted from [93])*

The FOWG resin is first spin-coated on a silicon wafer and UV cured according to the process described in section 1.b. It is possible to add an "adhesion promoter" step (like e.g. Ti-prime) to attenuate the surface dewetting of the resin on silicon. Also, a dehydration of the silicon substrate is possible, to reduce the water layer at the surface. The wafer is placed on hot plate followed by a few minutes in an oxygen plasma. Optionally, a 20-30 nm thick gold layer can be evaporated before resin deposition to facilitate the later removal of the waveguide from the substrate. The measured polymer film thickness is 30 μm. Before coating AZnLOF photoresist on the lower cladding layer, a 20 nm thick SiOx layer is deposited by thermal evaporation. Then AZnLOF is spin-coated on the SiOx layer (Figure IV.10(a)) and patterned through the mask by UV lithography (Figure IV.10(b)). The SiOx is then etched in buffered oxide etchant (BOE) through the resist mask (Figure IV.10(c)) according to the following reaction [94]:

$$SiO_{2_{(s)}} + 6HF_{(l)} \rightarrow H_2SiF_6 + 2H_2O \tag{IV.1}$$

Thickness measurements performed before and after etch tend to indicate that BOE also etches the photoresist (2 μm reduced to 300 nm after etch). This wet etching step may advantageously be replaced by an RIE etch of SiO_x. Afterwards a 15 to 20 nm gold film is deposited by thermal evaporation (Figure IV.10(d)). For the lift-off (Figure IV.10(e)) a suitable chemical had to be found because usual solvents like N-methyl pyrrolidone failed resulting in the disintegration of the FOWG film. Other solvents like acetone also failed because they partially attacked the FOWG. The lift-off worked well only with a basic solution (AZ 400K diluted 1:5 in DI water) which is usually employed as a photoresist developer. Afterwards, the remaining SiO_2 is removed by a second BOE attack (Figure IV.10(f)). Finally the samples are covered with the top FOWG cladding by spin coating and baked in the glove box (Figure IV.10(g)).

A possibility to resolve lift off difficulties is to improve the adhesion between the gold layer and the polymer cladding using plasma treatment [95–97]. We observed that adding oxygen plasma treatment of the wafer surface before and after the evaporation of gold lead to the reduction of air gaps at the gold/polymer interfaces, as shown in Figure IV.11.

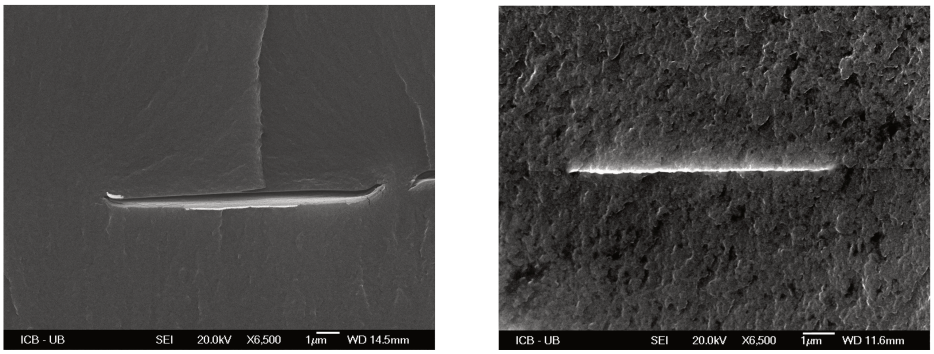

(a) *(b)*

Figure IV.11 *– Effect of Surface treatment on the adhesion between gold waveguide and polymer cladding.* ***(a)*** *without treatment ;* ***(b)*** *with oxygen plasma treatment*

At the end of fabrication the coupling facets (for end-fire coupling) were generated by a manual cutting using a fresh scalpel blade. Optical and electron-beam microscopy microscopy images of the facets generated are shown in Figure IV.12. With this method, no air gaps could be observed between gold and polymer as seen on the SEM micrographs in the bottom right image of Figure IV.12.

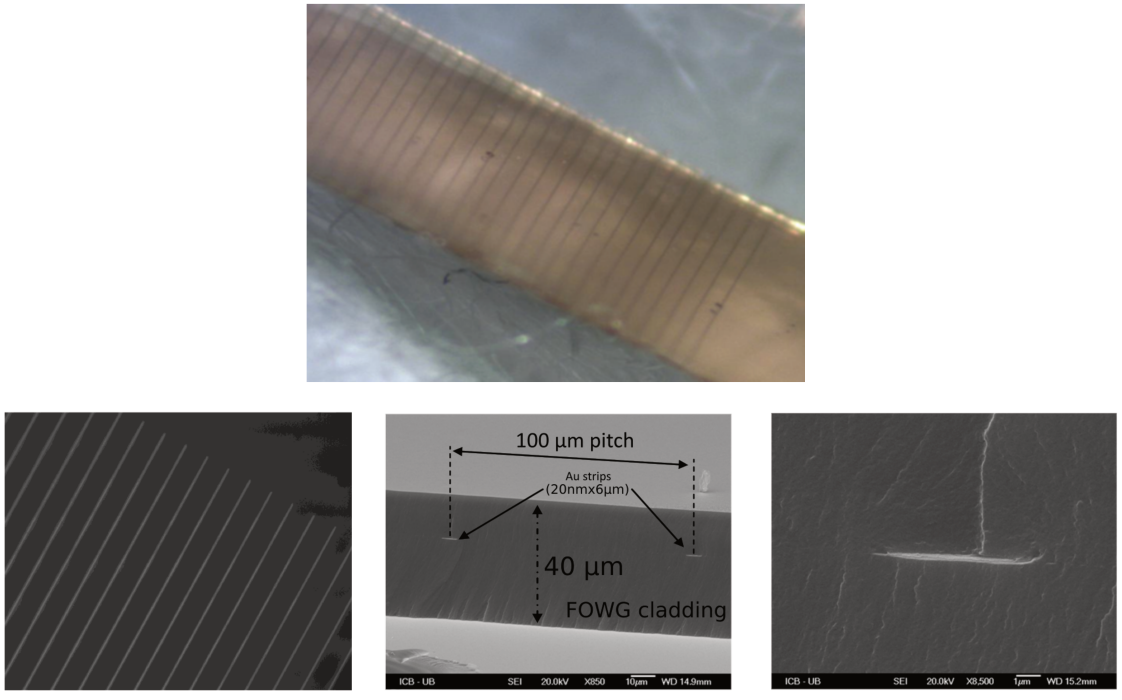

Figure IV.12 *– LR-SPP waveguides with FOWG.* ***Top:*** *final sample cut.* ***Left:*** *Optical Microscopy after lift-off.* ***Center:*** *SEM of sample edge showing 2 Au strips, distant by 100 μm;* ***Right:*** *Zoom in the Au strip (20 nm thick x 6 μm wide)*

The reported method was our best process flow that allowed to reduce the air gaps. However, even after this, the performances of the FOWG waveguides remained unsatisfactory in terms of losses (characterization in section 3.e). Our main hypothesis is

that the process induces some asymmetry of the refractive index between the top and bottom cladding around gold, affecting the propagation of the LR-SPP mode. Because refractive index is modified according to the degree of cross-linking, we identified the asymmetry problem in the fact that the bottom cladding is deposited and cross-linked (UV + heat) first and then submitted to a second UV exposure necessary to cross-link the top cladding deposited later. While the top cladding has only one cross-linking step the bottom cladding has two of them. The assembly method presented in section 2.d. has been developed to attempt resolving this asymmetry issue. Note that it is only after these further developments that we abandoned the exploitation of FOWG to the profit of other polymers Momentive and Lightlink (section 2.e).

2.c Flipping over method (FOWG)

A different fabrication procedure of the FOWG-based plasmonic waveguides was attempted by reversing the stacking procedure. This method was investigated also because it simplifies the time-consuming procedure presented in the previous section. The processing steps are shown in Figure IV.13. The first step consists in a standard UV lithography process using AZnLOF (Figure IV.13(a) and (b)). The gold layer is then evaporated on top (Figure IV.13(c)) followed by a lift-off step lift-off (Figure IV.13(d)). A FOWG resin layer is deposited on the gold waveguide and cross linked (Figure IV.13(e)). The next step is essential, because the stacked structure must be detached from the original silicon wafer, flipped over and stuck on a new silicon substrate (Figure IV.13(f)). The inverted structure will be regarded as the lower cladding. In the final step the upper cladding polymer is spin-coated and UV-cured (Figure IV.13(g)). The flipping step consisted in peeling the gold slab out of the initial substrate. This was easily done due to the poor natural adhesion of gold to silicon.

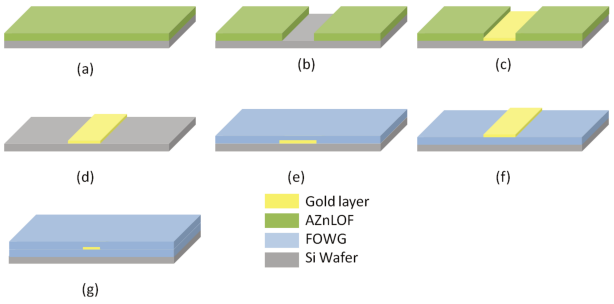

Figure IV.13 – *Process flow for the "Flipping over" method (FOWG)*

However, during this flipping step, a micro stress appears inside the gold waveguide due to the deformation of the film during peeling (Figure IV.14(a) and (b)). This effect reduces drastically the plasmon propagation, making this method unfortunately useless.

2.d Top and bottom claddings assembly method (FOWG)

We have been confronted with disappointing SPP propagation performances of the samples fabricated using the normal procedure presented in the previous sections. The chosen research direction was to make the structure more symmetric to improve the

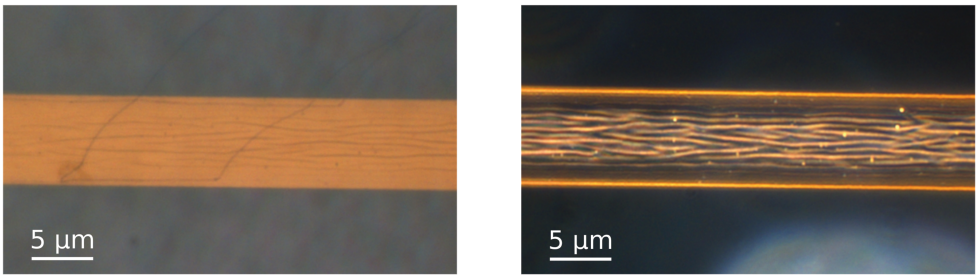

(a) *(b)*

Figure IV.14 *– FOWG / Gold waveguide (7.5 µm width) after the "Flipping over" method.* ***(a)*** *bright field microscopy image ;* ***(b)*** *Dark field microscopy image*

LR-SPP propagation length. A better cladding symmetrization is crucial to obtain the same refractive index between the upper and lower claddings. For this purpose a process of assembly of 2 identical polymer claddings has been developed for FOWG, in opposition to the normal process where the various layers are piled up from the bottom to the top. In this method both claddings are originally from the same substrate and are therefore submitted to exactly the same initial process. The substrate is divided into the two pieces, one for each cladding.

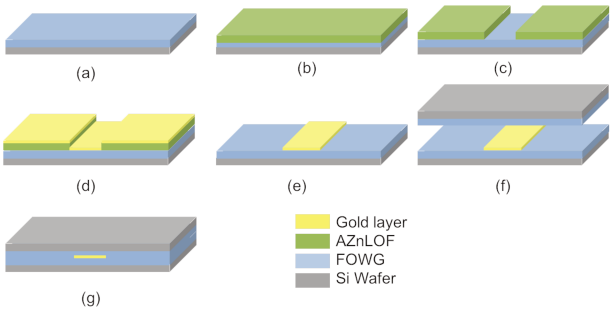

Figure IV.15 *– Top and bottom cladding assembly process - Initial approach*

The initial process flow of the developed assembly method is presented in Figure IV.16. In the beginning of the process flow, the gold waveguide with its SiOx sacrificial layer is fabricated on one of the two claddings by UV lithography with AZnLOF and Lift-off using the process already presented in section 2.b. It could be argued that the symmetry of the process is broken due to this lithography step on only one of the two claddings. However, a UV exposure equivalent to the dose received by photoresist AZnLOF was not applied on the other cladding because we considered that the UV dose employed in this step (55 mJ/cm^2) was negligible compared to the dose already received in step (a) 6500 mJ/cm^2 required to cure the FOWG layer. In addition, the majority of the energy is absorbed by this absorbant photoresist, and the UV energy actually reaching FOWG is even lower than 55 mJ/cm^2.

In order to obtain a good bonding of the two claddings at the final assembly step, we have chosen to cross-link a thin FOWG layer acting as glue between them, and for that purpose it is necessary to expose the entire stack to UV. This is why we replaced silicon by a transparent BK7 glass substrate. This additional UV exposure step is

realized in the mask aligner under mechanical pressure. FOWG resin was chosen rather than another resist in order avoid inducing new refractive index asymmetries and any chemical compatibility problems with the cross-linked FOWG of the cladding. For this purpose FOWG diluted with thinner solvent PGMEA (∼1:20) is spin-coated to produce a ∼100 nm thick interlayer. The difficulty of this bonding process is having a sufficiently flat and smooth polymer surface for a good final assembly with a perfect contact between both claddings without trapping any air bubbles.

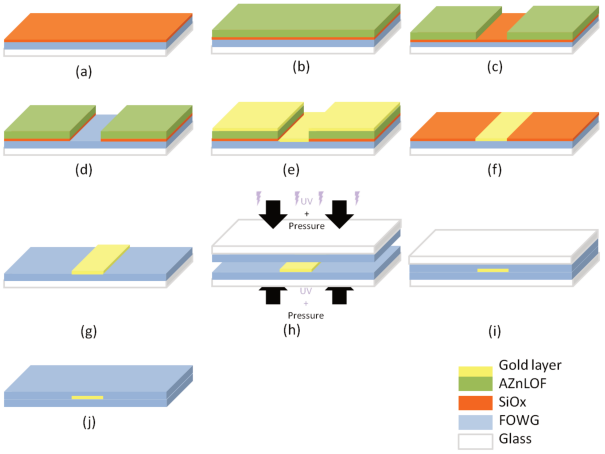

Figure IV.16 – *Top and bottom cladding assembly method with transparent substrate (FOWG)*

A crucial step is step (j) where the substrate has to be removed to obtain a flexible waveguide. A diamond mark is made on the backside of the substrate, and a mechanical pressure is applied to obtain a cleavage of the substrate. Too many difficulties were encountered when removing the top substrate without damaging the waveguides. This is why we had to test various assembly methods.

A variation of the process (described in Figure IV.17) was found to facilitate the final assembly. It consisted in peeling off the bottom cladding from its substrate prior to assembly (Figure IV.17(j')). Peeling is eased due to the presence of a 30 nm thick gold film deposited on the substrate in step (a'). In the assembly step (k) a cylinder is first rolled over the assembly with a constant force in order to remove air bubbles which may be trapped at the interface. The final UV curing of a thin FOWG layer which was coated in step (j) is realized in the mask aligner to assure the bonding step (l). For this purpose the substrate removed previously is placed again on top of the assembly and a load is applied during the UV curing. The gluing FOWG interlayer was cross-linked by a double-sided flood UV-exposure (same UV dose from both sides of the stack) in order to respect the symmetry throughout the process.

Other methods have been tested where the glue interlayer was replaced with other interlayers, but they failed to produce a correctly adhering laminate. The last steps (m) would be the detachment from the substrate but this step was omitted in a first instance to characterize the flat, un-bent samples.

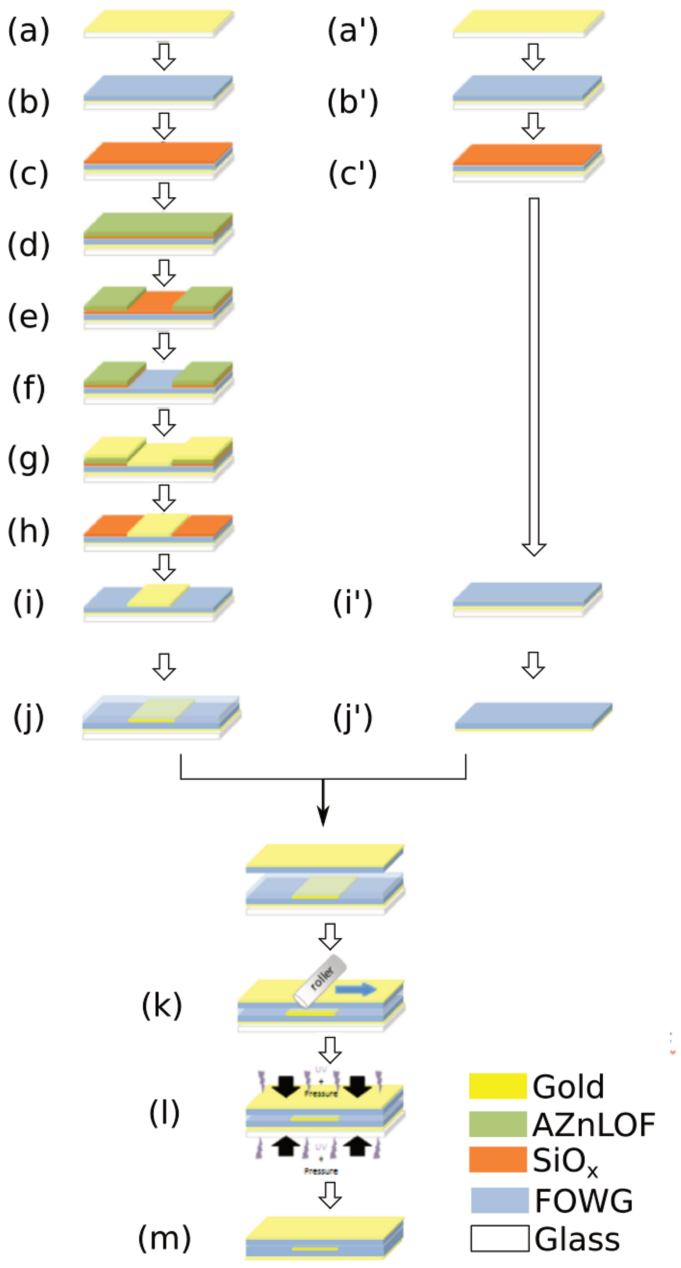

Figure IV.17 – *Top and bottom cladding assembly method with peeled-off top cladding (FOWG).*

In Figure IV.17, the final cutting generating the cleaved facets ready for fiber end-fire coupling is not represented. This is realized by cutting the film with a scalpel blade perpendicularly to the waveguides and then cutting the substrate near the previous waveguide cutting line.

Unfortunately this fabrication method was not reproducible enough. We could not avoid the trapping of bubbles at the interfaces, as shown in Figure IV.18, and the plasmon propagation length was not improved in comparison to the standard stacking up method. This method was abandoned because of its complexity and time-consumption.

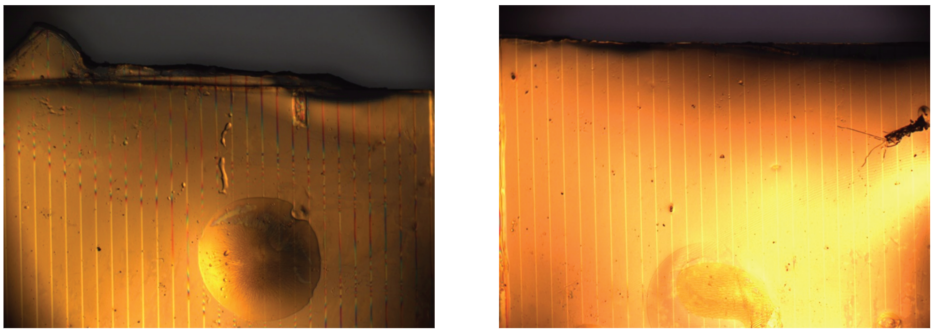

(a) *(b)*

Figure IV.18 *– Bubbles trapped at the interface of the 2 claddings during the assembly process.*

2.e LR-SPPW fabrication with LightLink and Momentive polymers

For Lightlink and Momentive polymers, the approach based on the plasma etching of gold was reconsidered and contrary to FOWG, the films made with either Lightlink or Momentive polymers were able to withstand etching without being affected too much. The siloxane nature (with the heavier Si atoms in the polymer) of those materials compared to FOWG which is ethylene-oxide - acrylate polymer platform (without Si) might be an explanation of this difference of behavior. The lift-off approach is still possible for these siloxane polymers but during our studies we realized the advantages of the etching process over the lift-off to fabricate this type of structures.

Figure IV.19 summarizes the process flow. After coating the bottom polymer cladding, gold is deposited by thermal evaporation. A photoresist (AZ 701 MIR was chosen) is then coated on top of gold and structured by UV lithography through the waveguide mask. The etching of gold is then realized in our Reactive Ion Etching (RIE) tool with a pure Argon sputter etch recipe. During the next step, the remains from the photoresist mask are removed by a combination of dissolution in a solvent and oxygen plasma treatment. During the final step the wafer is covered with the top polymer cladding in a process identical to the bottom one. At step (h), in theory there should be no photoresist left. However, occasionally we have observed some resist residues persistent even after prolonged stripping treatments. These treatments may also affect the polymer cladding, therefore to avoid this, the stripping treatment duration was limited. We consider that a few residues should not be too detrimental to the performances of the waveguide.

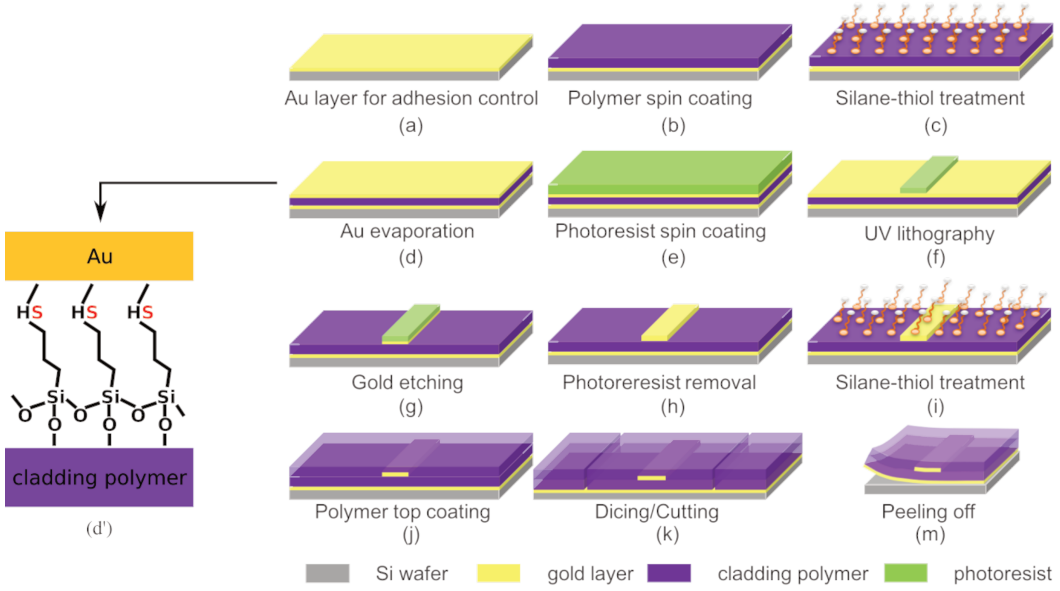

Figure IV.19 – *Fabrication process flow based on gold etching.*

In the first sample batches produced without silane treatment, plasmon propagation was not as good as expected and not very reproducible. We attributed this problem to the creation of air gaps at the gold/polymer interfaces due to poor natural adherence between these two materials. These gaps induce a loss of refractive index symmetry around the gold strip that greatly reduces plasmon propagation. In order to obtain a better adherence we introduced the two additional surface functionalization steps, one immediately prior to Au evaporation (Figure IV.19(d)) and the other one immediately before coating the top polymer cladding (Figure IV.19(j)). The Figure IV.19(d') shows an ideal chemical representation which does not totally reflect the chemical bonds existing between the gold layer and the polymer. The developed functionalization process consists of, firstly, a surface activation step and secondly the deposition of a specially designed bifunctional molecular linker. This linker will consist of a silane group, which will have a silane group to anchor polymer chains on one side and a thiol group to bond with gold atoms on the other side, well-known for the capacity to bond with gold atoms. The used linker was 3-mercaptopropyltrimethoxysilane. This chemical functionalization thus creates solid nearly covalent Au-S bonds between the linker and gold surface atoms. The samples with chemical functionalization were much better for the shape of the plasmon mode, had lower optical losses and were more reproducible.

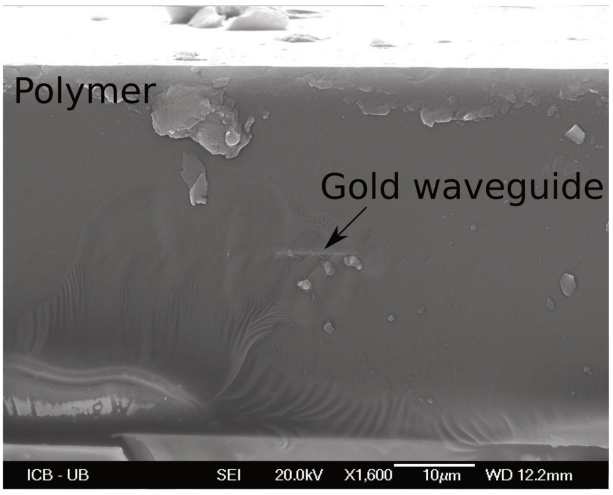

Figure IV.20 – *Momentive LR-SPPW : SEM image of the facet after cleaving the wafer.*

The molecular linker approach (silanization), successfull for both Momentive and LightLink polymers (both silicone-base polymers), was also studied in the case of FOWG but did not succeed. This is due to the fact that the silane process is not compatible with the lift-off process which is the only appropriate one for FOWG. The silanization is much more adapted to our fabrication method based on etching.

2.f Generation of the waveguide coupling facets.

When the wafer fabrication process is finished, the coupling facets perpendicular to the waveguides axis are generated and waveguides have to be cut to the desired length. Several methods have been tested with the objective to minimize the coupling losses. The simplest methods are by cleaving the silicon wafer or by using a scalpel to cut the polymer layer. The cleaving method proved to be generally efficient for the purpose of this study although the polymer facet could have an irregular shape, resulting in waveguide-to-waveguide coupling loss discrepancies. Cutting with a scalpel was also used but seemed to result in slightly higher losses.

Laser-cutting was also attempted in UB with an 800 nm wavelength Ti-sapphire laser delivering 100 fs pulses at 1 kHz with an estimated energy of 75 $\mu J/cm^2$/pulse and a linear speed of 320 μm/s over the sample. In these conditions the waveguide end got damaged probably due to high local temperatures, as shown in Figure IV.21. The losses were found to be much higher in this case.

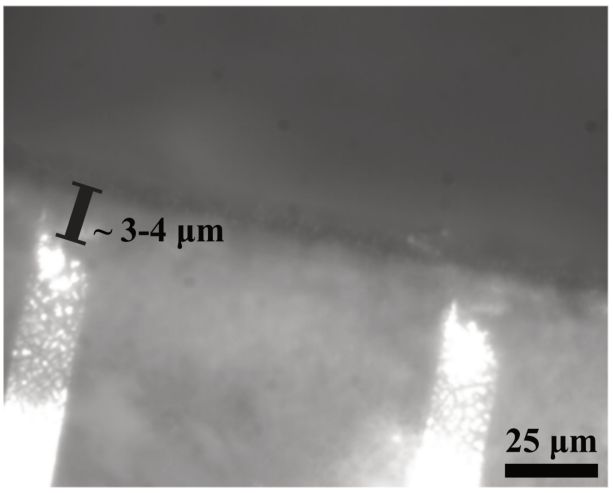

Figure IV.21 – *Microscopy image of the edge of the waveguides after laser cutting.*

Due to difficulty of access to other laser cutting tools in other institutes and the related larger delays, we could not continue with laser cutting. However, this type of method should be reconsidered for producing more advanced LR-SPPW components in the future.

For the best wafers, fabricated at the end of the project, dicing with a diamond saw was used. Dicing was performed by our PhoxTroT partner TE Connectivity. This method resulted in samples that were sometimes a bit smeared with particles and tiny scratches but with slightly lower coupling losses than using standard cleaving. Moreover, when observing the plots of cut-back method, the dicing clearly reduced the standard deviation of the coupling loss values. The detailed results of this study can be found in section 7. The slight surface damage that we mentioned did not affect the waveguides performance because the waveguide core is protected by a 10 μm thick polymer. This dicing method could not be used for all wafers due to various practical constraints, so in most cases simple cleaving was preferred, giving reasonably good results.

3 Optical characterization of the stand-alone LR-SPPW.

3.a Experimental setup and methodology.

During this work, characterization was only performed in a straight configuration in UB, the sample still being attached to the silicon substrate. The bending configuration setup was developed by Yiting Chen in SDU and he measured bending losses in our samples. We used three complementary methods: imaging of the SPP intensity, where the decay is detected directly from the camera situated over the sample (Figure IV.22), imaging of the mode profile at the output facet of the sample (Figure IV.23) and finally fiber-to-fiber insertion loss measurement (Figure IV.24). The cut-back method is employed using these insertion loss measurements on samples of different lengths cut out from the same wafer.

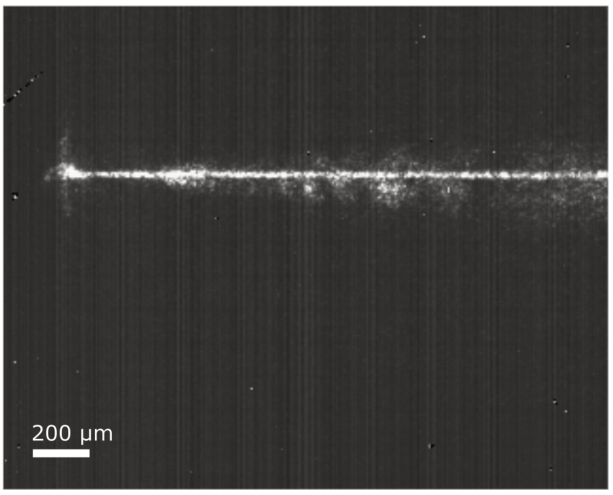

Figure IV.22 – *Imaging of the SPP intensity decay detected by camera directly from above the sample („top view“).*

Figure IV.23 – *Imaging of the SPP mode profile at the output facet of the sample („side view“).*

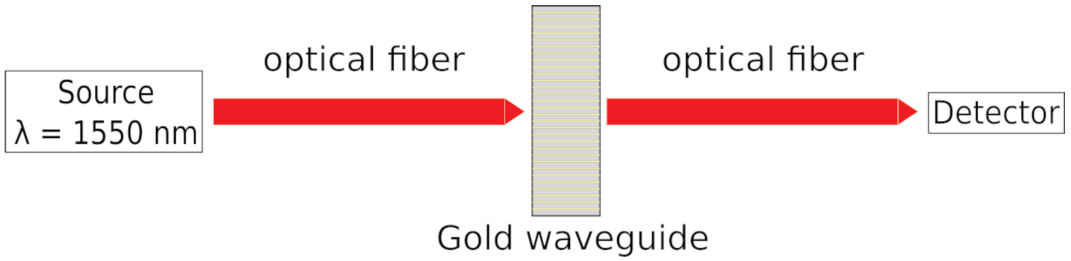

Figure IV.24 – *Optical insertion loss measurements.*

All the presented results were realized on a home-made bench which was modified according to the needed measurements. It is composed of an IR source (Anritsu, OSICS-**E**xternal-**C**avity-**L**asers) with fiber output, a 3-paddle polarization fiber controller, two single mode fibers (SMF 128), and a power-meter. The fiber end was stripped so that only the core of the fiber was coupled to the waveguides in end-fire configuration as shown in Figure IV.25. In all the experiments the polarization was varied between TM and TE to check the SPP mode being switched on (TM) and off (TE). The IR camera (Xenics,

Bobcat) was mounted on a binocular microscope equipped with 2 objectives x5 and x20.

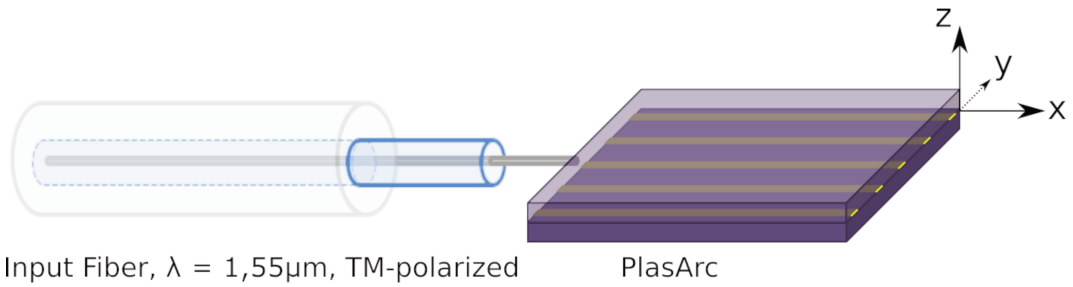

Figure IV.25 *– 3D view of the fiber-to-sample end-fire coupling.*

For each sample the experimental protocol consists of the following steps: The reference intensity I_0 is measured by coupling the in and out fiber beforehand. For an input power of 1 mW, I_0 was generally about 0.6 mW. In order to align properly the input fiber with the waveguide (in this setup there are 5 freedom degrees comprising 3 translations and 2 rotations), the long-range plasmon propagation is imaged with the IR camera placed above the waveguides (configuration of Figure IV.22). A typical image of the plasmon is given in Figure IV.26.

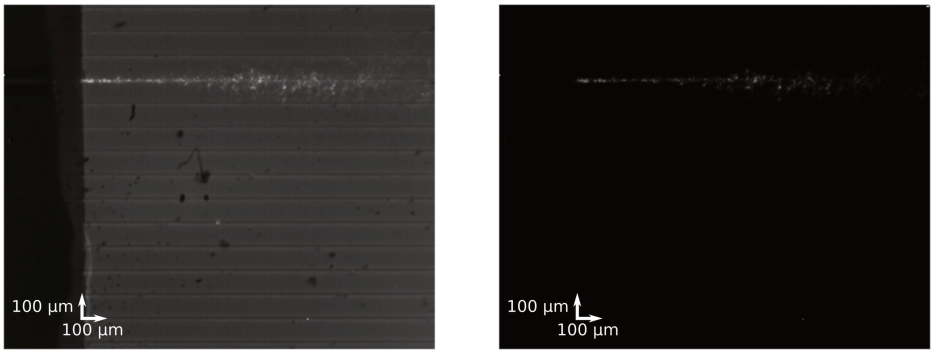

(a) *IR + white light illumination.* ***(b)*** *IR image only*

Figure IV.26 *– Typical far-field IR image of the LR-SPPW propagating plasmon.*

The decaying energy of the plasmon along the waveguide can be observed due to the radiative losses of the plasmon. This allows to find an estimation of the propagation length directly by fitting with an exponential decay along the waveguide (Figure IV.27).

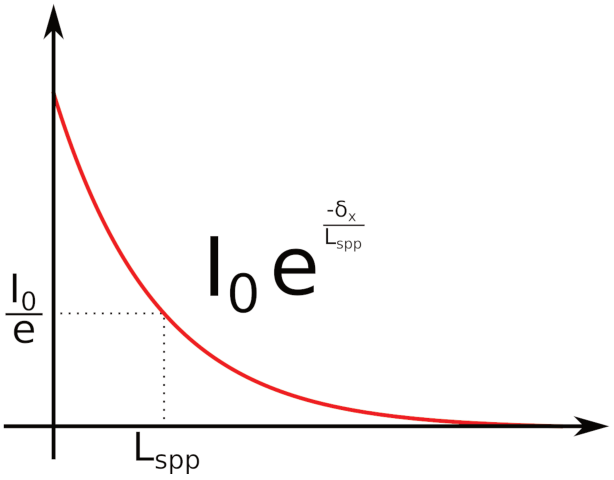

Figure IV.27 – *Exponential decay of the intensity along a plasmonic waveguide.*

During the next step the camera viewing angle is rotated by 90^o and is positioned in front of the waveguide output (configuration of Figure IV.23) to record the image of the mode leading to measurements of the mode size in the longitudinal direction (along the y axis) and in the transversal direction (along the z axis) and both in TE or TM polarization. An example of SPP mode image is shown in Figure IV.28. The measured modal size can be compared to theory and simulations.

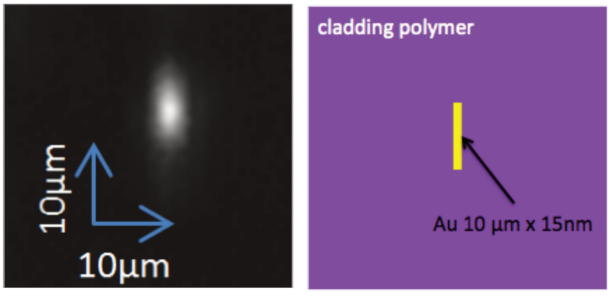

Figure IV.28 – *Output LR-SPP mode imaged at 1.55 µm (**left**) ; corresponding structure (**right**).*

During the final step a SM-fiber is coupled at the output end of the waveguides in place of the IR camera and insertion losses are measured with a power-meter placed at the other end of the fiber. The sample is translated along the y-axis using a micrometer displacement screw in order to scan the different waveguides which are organized according to the design of Figure IV.29. The design contains a series of 5 arrays, each of them having 30 or 60 identical waveguides. The waveguide width is varied from array to array: 5, 7.5, 10, 12.5 and 15 μm. Each array is separated by a larger space to be easily visualized. For each value of w, all the intensity measurements are averaged over a set of at least 5 identical waveguides. Then the measurements are done on samples of different lengths and this cut-back method allows us to estimate the propagation and coupling losses out of the data.

In the end the estimations of propagation losses obtained by the two different methods (SPP decay fitting and fiber-to-fiber intensity measurements) can also be compared.

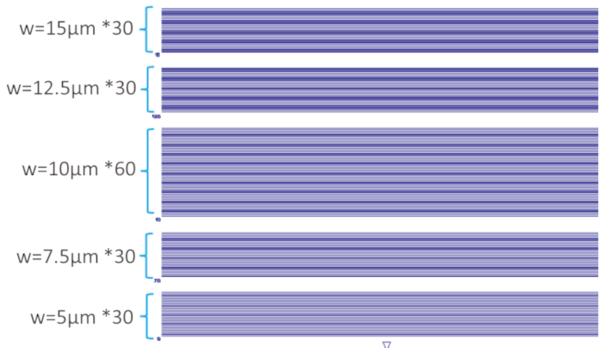

Figure IV.29 *– LR-SPPW waveguide mask design containing 5 arrays of straight waveguides of varied width.*

3.b LR-SPP mode imaging results.

Figures IV.30 and IV.31 shows the IR images of the LR-SPPW plasmon mode respectively using Momentive and LightLink polymer at the output of the waveguide for varied waveguide widths compared to simulations. The results are in good agreement.

Width (μm)	n_{eff}	k_{eff}	L_{spp} (mm)	Long. Mode FWHM (theo.)	Long. Mode FWHM (exp.)	Trans. Mode FWHM (theo.)	Trans. mode FWHM (exp.)
5.0	1.410131	3.30E-06	37.384	8 μm	8.7 μm	7 μm	5.8 μm
7.5	1.410360	6.89E-06	17.897	9 μm	9.7 μm	6 μm	5.1 μm
10.0	1.410560	8.97E-06	13.754	10 μm	11.6 μm	6 μm	4.8 μm

Table IV.6 *– Comparison of mode sizes between simulations and experiments for Momentive polymer.*

For widths between 5 and 10 μm, simulations find only one first order mode. For 12.5 μm and 15 μm modes of higher order are found.

Width (μm)	Long. Mode FWHM (theo)	Long. Mode FWHM (exp.)	Trans. Mode FWHM (theo)	Trans. mode FWHM (exp.)
5.0	8 μm	8.7 μm	7 μm	5.8 μm
7.5	9 μm	9.7 μm	6 μm	5.1 μm
10.0	10 μm	11.6 μm	6 μm	4.8 μm
12.5	12 μm	12,8 μm	6 μm	4,7 μm
15.0	14 μm	15,6 μm	6 μm	4,9 μm

Table IV.7 *– Dimension of FWHM of output mode for Momentive polymer.*

The Summary of Plasmon Mode size results show an overall correct agreement between simulations and experiments. (Table IV.9)

3.c Fiber-to-fiber Insertion losses and cut-back method results.

The insertion losses results and the cut-back plots are now presented. Figure IV.33 reveals a typical TM/TE polarization extinction ratio of about 25 dB in the case of Lightlink polymer, which is pretty satisfactory. Similar polarization ratios are obtained with Momentive.

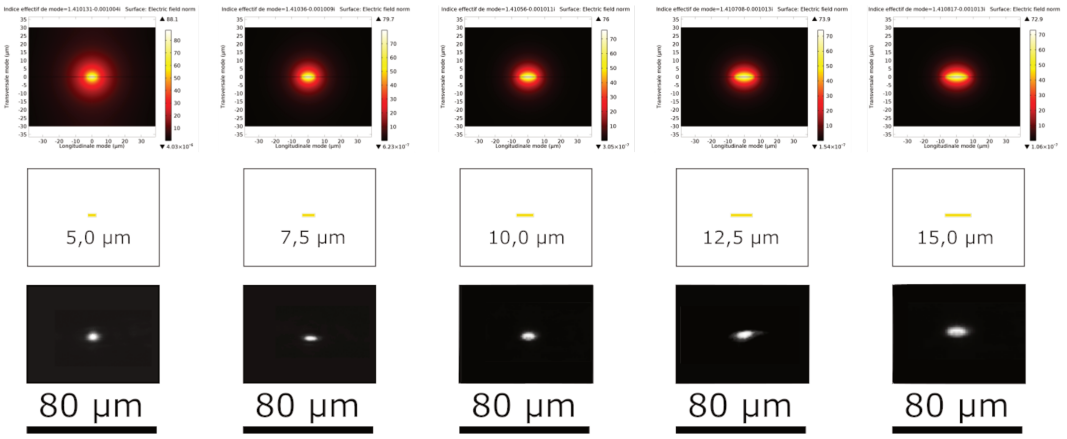

Figure IV.30 *– Au-Momentive LR-SPPW. 1.55 µm imaging of output mode of ∼1 cm long sample (**bottom :** experimental; **middle :** design; **top :** simulations).*

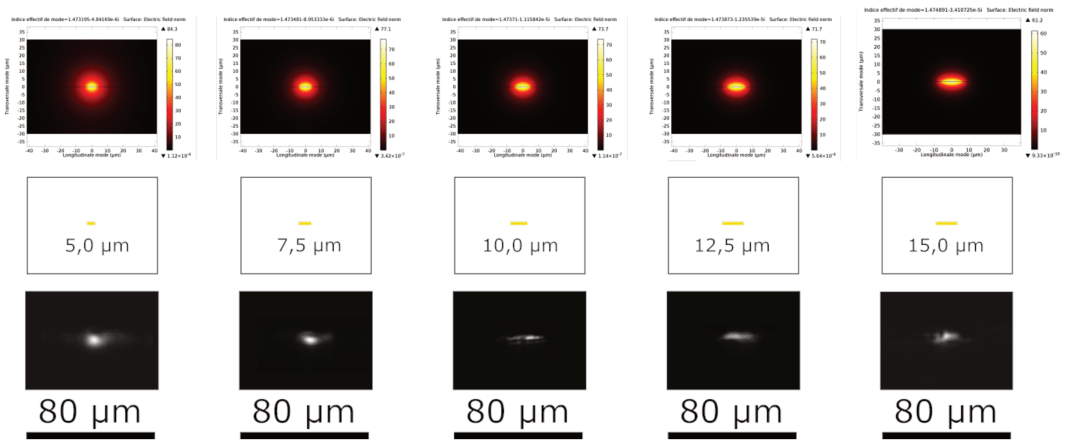

Figure IV.31 *– Au-LightLink LR-SPPW. 1.55 µm imaging of output mode of ∼1 cm long sample (**bottom :** experimental; **middle :** design; **top :** simulations).*

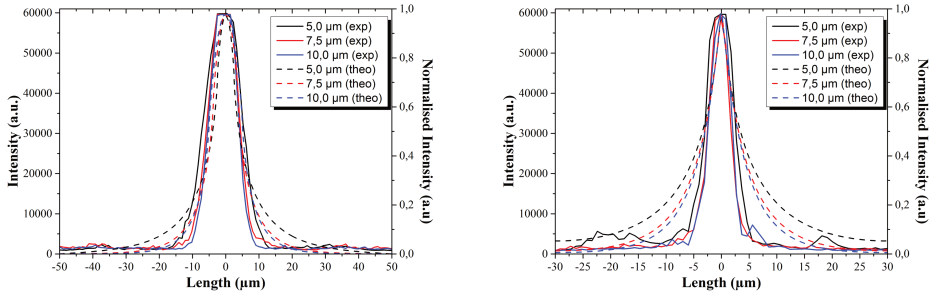

(a) *Output longitudinal mode* ***(b)*** *Output transversal mode*

Figure IV.32 *– Longitudinal and transversal output mode and comparison with simulation for three waveguides (5, 7.5, 10 µm) for Momentive polymer*

The plasmonic mode losses in TM are plotted in Figure IV.34 (for Momentive) and Figure IV.35 (for Lightlink) for varied waveguide widths. In both cases the propagation loss lies in the 0.3 to 1.2 dB/mm range and the coupling loss between 3 and 10 dB (for

Width (μm)	Long. Mode FWHM (theo)	Long. Mode FWHM (exp.)	Trans. Mode FWHM (theo)	Trans. mode FWHM (exp.)
5.0	6.1 μm	5.6 μm	4.5 μm	4.8 μm
7.5	7.7 μm	5.7 μm	4.3 μm	4.8 μm
10.0	9.5 μm	7.2 μm	4.3 μm	4.8 μm
12.5	11.3 μm	8.7 μm	4.3 μm	4,8 μm
15.0	13.1 μm	9.1 μm	4.3 μm	4,8 μm

Table IV.8 – *Dimension of FWHM of output mode for LightLink polymer.*

	Waveguide width	5 μm	7.5 μm	10 μm	12.5 μm	15 μm
Momentive	Longitudinal FWHM	8.7	9.7	11.6	12.8	15.6
	Transversal FWHM	5.8	5.1	4.8	4.7	4.9
LightLink	Longitudinal FWHM	5.6	5.7	7.2	8.7	9.1
	Transversal FWHM	4.8	4.8	4.8	4.8	4.8

Table IV.9 – *Summary of Plasmon Mode size (FWHM) at waveguide output (experimental).*

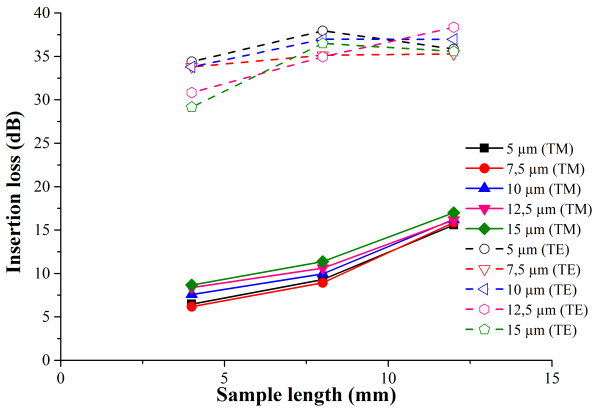

Figure IV.33 – *Au-Lightlink LR-SPPW : loss measurements in TM and TE polarization.*

input + output facets) when normal wafer cleaving is used. The dip at about 10 μm in the propagation length plot (Figure IV.34b) might be explained by the occurrence of additional modes above this threshold. In the case of Lightlink material the behavior was different with little loss variation in function of waveguide width (Figure IV.35b).

The employed cutting method to make the perpendicular facets for end-fire fiber coupling was generally a basic mechanical cleavage of the Si wafer, which does not always result in a regular and perpendicular facet but is a quick and easy method for the LR-SPPW development stage. This cutting method usually resulted in a variable coupling loss between 3 and 10 dB depending on the waveguide, as can be seen in Figure IV.34. In order to improve this, test wafers were cut with a dicing saw by TE connectivity. As a result, the coupling was slightly decreased to the 3-6 dB range, thus not in a significant manner but with less variability than before, as can be seen in Figure IV.35.

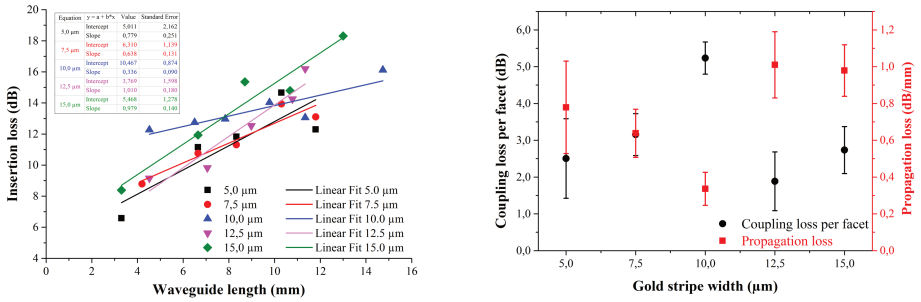

(a) *(b)*

Figure IV.34 – *Au-Momentive LR-SPPW (cleaved): Cut-back method.*

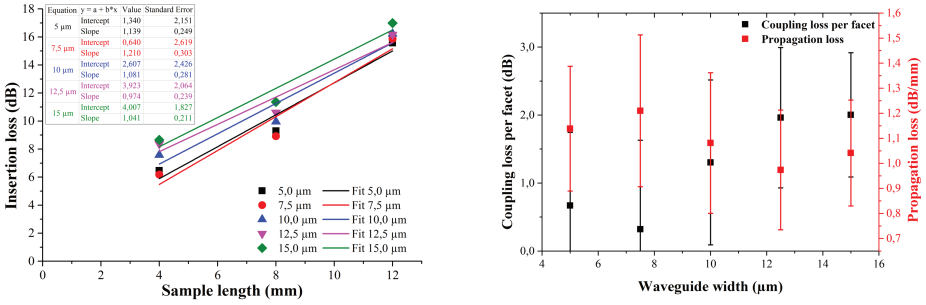

(a) *(b)*

Figure IV.35 – *Au-Lightlink LR-SPPW (diced) cut-back method.*

3.d LR-SPPW with Silver metal.

Silver was tried as a replacement for gold. Based on simulations, silver is supposed to increase propagation length by a factor of about ∼2.5, corresponding to ∼0.5 dB/mm loss and this is due to intrinsically better plasmonic properties of silver. The experimental result was disappointing because of a poor TM/TE polarization ratio of only a few dB in favor of TM which led us to use gold in the PhoxTroT project (see Figure IV.36).

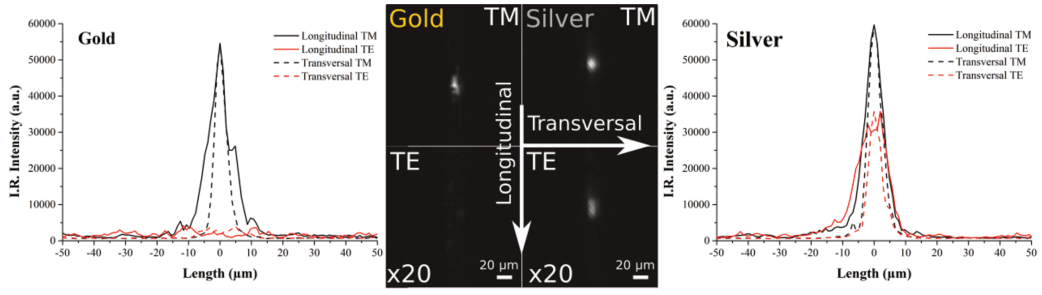

Figure IV.36 – *Comparison of Au and Ag LR-SPPWs : TM and TE mode imaging (strip width of 15 µm).*

The only explanation we could give is that the thin silver layer is qualitatively worse than gold, with probably higher roughness and more light scattering. Nevertheless in TM polarization we do observe a propagation loss 0.3 to 0.4 dB/cm lower than with

gold, corresponding to an increase in propagation length of a factor ranging between 1.5 and 1.9, not too far from simulation prediction. A deep study of the conditions of evaporation might be a way of improving the poor polarization ratio. The loss results for silver LR-SPPW are shown in Figure IV.37.

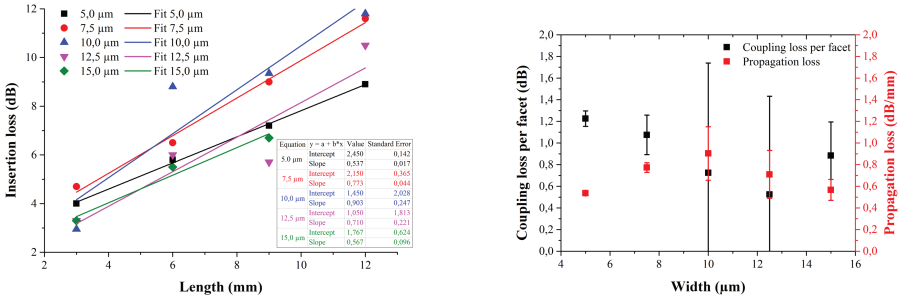

(a) *(b)*

Figure IV.37 *– Ag-Lightlink LR-SPPW (diced) cut-back method.*

3.e LR-SPPW with FOWG polymer.

In the case of FOWG, a large number of samples were fabricated without even getting a plasmonic mode propagating to the end of the sample and we found that this was due to the presence of air gaps between gold and polymer, as illustrated in Figure IV.38. It is only after solving this problem (see in section 2.b) that better performing FOWG-based LR-SPPW could be fabricated.

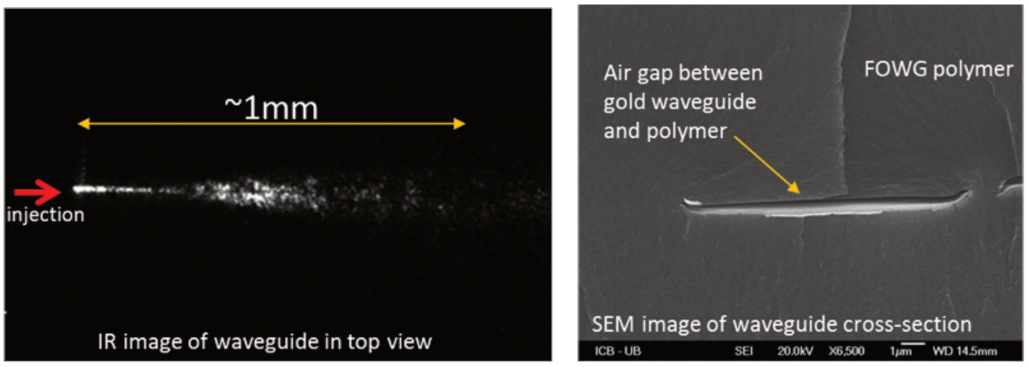

Figure IV.38 *– Au-FOWG LR-SPPW having air gaps at the Au / FOWG interface.*

Even with the best FOWG sample, it was difficult to obtain a sharp LR-SPP spot at the waveguide end. In Figure IV.39 we can see that the plasmon propagates over a fraction of millimeters but the intensity quickly gets diluted into a halo in the surroundings of the waveguide, making it difficult to obtain a clear concentrated spot at the output. The exponential fit of the decay gives an $L_{SPP} \approx$ 1.4 mm, corresponding to $\approx$ 3.2 dB/mm propagation loss, which is too high compared to samples fabricated with other polymers.

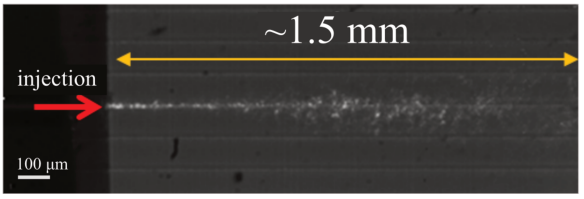

Figure IV.39 *– Au-FOWG LR-SPPW, best sample. IR image from the top of the waveguide.*

4 Bending loss measurement of single cladding plasmonic arcs.

We present the characterization results of the curved single-cladding plasmonic arcs fabricated with Lightlink material (n =1.476). The plasmonic arcs are peeled off from the silicon wafer to measure the bending loss. Two experimental setups were used: firstly a single S-bend with fixed bending radius and secondly a double S-bend configuration where both ends of the samples were fixed to movable stages, with the middle part of the waveguide suspended in air. In the latter case different curvature radii has improved much compared could be reached by decreasing the distance between the two stages. Both methods gave similar results: the bending loss of plasmonic arc with 7.5- μm-wide gold stripe is about 2.2-2.8 dB/90^o, and the polarization ratio is 15-20 dB for a bending radius r of 2.5 mm. The double-bend and the corresponding loss plot are shown in Figure IV.40. After the LR-SPP mode is excited by an SM fiber from one end, the maximum output intensity is obtained from the other end. The stage with the output end of the sample is moved towards the input end to bend the middle part of the waveguide. In this case, the fluctuation of the coupling efficiency in the input end is minimized. In order to obtain the bending radius value, we assume the bending part of the waveguide is composed of four identical arc parts, with the same radius r and bending angle θ, as shown in Figure IV.40(b). The length of the bending part of the waveguide is l, and the decreased length d. The bending radius can be determined easily from the two equations 4rθ=l and 4r.sinθ=l-d.

The total length of the flexible arc is 12 mm and l is 8 mm. By moving the two stages, the bending radius decreases from 16.3 to 2.2 mm. The measured bending loss and polarization ratio for the 7.5- μm-wide gold strip are shown in Figure IV.40(c). A high polarization ratio (from 25 to 16 dB) is maintained even when r decreases to 2.2 mm. The bending loss is slowly increasing when r drops from 16.3 to 5 mm (from 0.2 to 1.1 dB/90 μ), and then fast with further decreased bending radius (4 dB/90 μ at r=2.2 mm). The bending loss and polarization ratio are 2.8 dB/90^o and 20 dB at r=2.5 mm, which is pretty close to the counterpart result (2.2 dB/90^o and 15 dB) of S-bend configuration with the same radius. The slightly increasing bending loss indicates that the sample suffers little deterioration even after it has been curved in the S-bend configuration, underlining the flexibility and stability of the waveguide.

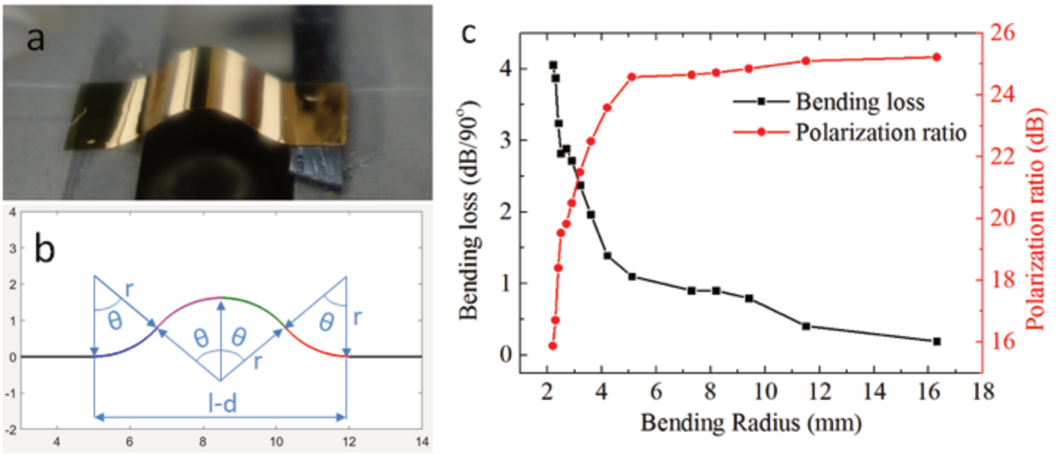

Figure IV.40 *– (a) Photograph of the bended plasmonic arc with both ends attached to narrow silicon stripes. (b) Curve model for the calculation of the bending radius. (c) Measured bending loss and polarization ratio versus bending radius for W_{strip}=7.5 µm.*

5 Bending loss measurement of double-cladding plasmonic arcs.

The multiple cladding fabrication method was developed only with Momentive polymers, which were provided in two grades of indices n=1.41 and n=1.468 that can be mixed in any ratio to obtain a polymer mixture with the wanted refractive index between these two values. Double-cladding plasmonic arcs show reduced bending loss compared to the single-cladding ones. The studied structure is illustrated in Figure IV.41(a). Two blends I and II were made from the provided MPM526A&B materials in different proportions to generate both inner and outer claddings with refractive indices of 1.468 and 1.458, respectively. The thicknesses of the inner and outer claddings are 4-6 and 10-20 µm, respectively. The electric field of the LR-SPP mode is mainly confined in the inner cladding layers around the gold stripe, as shown in Figure IV.41(b), obtained by a finite-element numerical method.

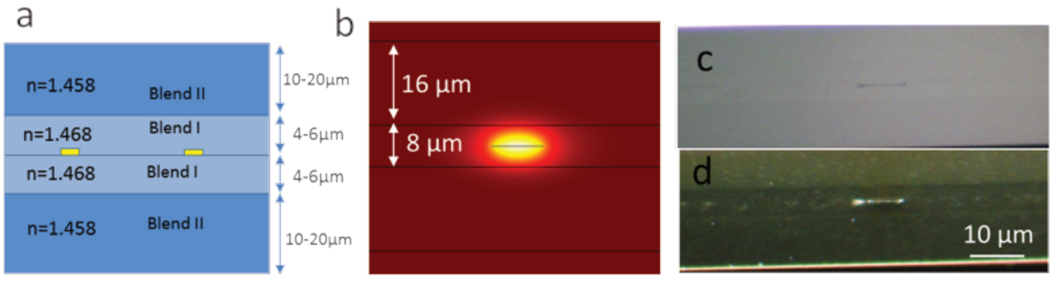

Figure IV.41 *– (a) Structure layout of the double-cladding plasmonic arc. (b) Calculated electric field distribution of the fundamental TM mode with gold w=10 µm and t=15 nm. Optical microscope images from side view in bright (b) and dark (c) field.*

The insertion loss and polarization ratio of the straight plasmonic arc are measured both before and after separation from the substrate. The results in Table IV.10 show that the

damage is avoided pretty well with a careful peeling process even though the gold underlayer is only 4 nm thick in this sample: the insertion loss of the 11 mm long arc has been increased by 0-2 dB, and the polarization ratio is also still larger than 20 dB. Since the coupling loss is always 1-2 dB/facet, the propagation loss of the straight plasmonic arc is about 1.2-1.5 dB/mm, which is close to the values obtained in other plasmonic arc samples.

	Insertion loss (dB) / Polarization ratio (dB)		
Gold strip width	7.5 μm	10 μm	12.5 μm
Before peeling off	17/21	17/26	16/24
After peeling off	19/20	17/23	17/24

Table IV.10 – *Comparison of insertion loss and polarization ratio of the straight double-cladding plasmonic arc of different gold strip widths before and after being peeled off from the silicon wafer.*

Bending loss was measured in the varying bending radius configuration as presented in the previous section. When the incident light is TE polarized or the light is coupled to the polymer layers above or below the gold strip, the incident light will not be coupled into well-confined mode, it will only diffuse and dissipate into the polymer. The length of the cleaved sample is 11 mm, but the length of the bendable part of the flexible waveguide is between 5, 7 and 8 mm. Generally speaking, the performance of this double-cladding sample presented in Figure IV.42 has improved much compared to that of the single-cladding one. The bending losses at r = 2.5 mm for 5, 10 and 12 μm gold stripes are 1.5, 1.7 and 0.7 (and 1.2 for 12.5 μm B) dB/90^o, compared to 2.2-2.8 dB/90^o for the single cladding case. The bending loss increases much for bending radii smaller than 2 mm (3 mm for the case of 10 μm-wide strip). Similarly, the polarization ratio is maintained above 10 dB for bending radii larger than ∼2 mm (Figure IV.42(c)). The observed fluctuations of the polarization ratio may relate to the instability of the polarization controller. Therefore, the low polarization ratio of the incident wave could lead to degraded performance of the plasmonic arc.

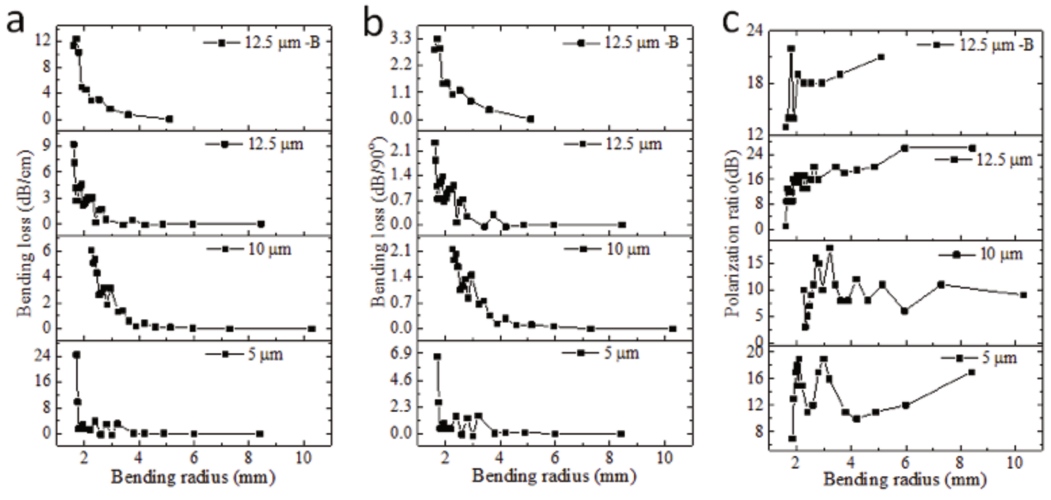

Figure IV.42 – *Double-cladding plasmonic arc: measured bending loss of the LR-SPP mode by dB/cm. (a) by dB/90^o, (b) and polarization ratio (c) versus bending radius of arc with the gold strip width of 5, 10, and 12.5 μm respectively. "12.5 μm B" indicates another waveguide with gold stripe width of 12.5 μm but different length in the same sample.*

The double-cladding structures therefore experiences very low bending loss when r>2 mm (<2 dB/90^o at r=2.5 mm), which is slightly better than the single-cladding one. We did additional tests to study the ability of the samples to recover their original state after bending. The free-standing plasmonic arcs were wrapped the used glass waveguides180^o around some cylindrical pillars with radius between 0.5 and 3 mm. We observe that, even when the bending radius reaches 1.5 mm, the samples relax to their original state without residual damage. Only after the bending radius is smaller than 1.5 mm, some extra small cracks of the gold strip can be detected under optical microscope but the polymer is still intact. The waveguides do not break even when the bending radius reaches 0.5 mm. The results demonstrate that plasmonic arcs have excellent flexibility and stability under bending circumstances.

6 Interfacing LR-SPPWs with single-mode ion-exchanged glass waveguides.

This section deals with the coupling of the LR-SPPWs we have fabricated with Phox-TroT's optical PCBs. Samples provided by Fraunhofer IZM contained low-loss single-mode glass waveguides a few centimeters long. These waveguides were fabricated by an ion exchange process leading to graded index waveguides with their insertion loss (mostly coupling loss) expected to be below 2-3 dB an the propagation loss below 0.015 dB/mm. The core of the waveguide is situated approximately 5 μm below the surface of the sample.

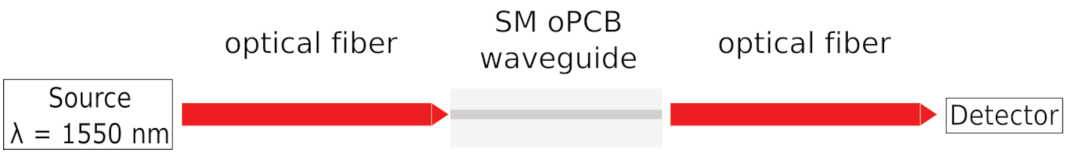

Figure IV.43 – *SM-oPCB glass waveguides.*

Our working bench was modified for this study which needed the careful alignment of the various individual elements. Firstly the oPCB was studied in stand-alone before realizing the coupling [98]. The alignment with the input fiber was controlled using the IR camera and objective observing the output facet of the waveguide, to see the output mode. After this control, the fiber out and the power-meter were positioned at the output facet of the waveguide. We finally report the optical coupling of the plasmonic arcs with single-mode glass waveguides, which can be used as optical Printed Circuit Board (oPCB). This is the first step towards the commercial application of plasmonic arcs as interconnects. The fabrication process and performances of the glass waveguides have been described elsewhere [99, 100]. The used glass waveguide samples show very low propagation loss, below 0.015 dB/mm. The Measurement Identification Code of our interfacing experiment according to IEC 62496-2 standard was MIC 141-011-011-011-011. Using SM fibers and a 1.55 μm source, the insertion loss is 2.2 dB for a 31 mm long sample. The used glass waveguides were in an early production stage, thus showing varying propagation losses of 0.005-0.015 dB/mm and fiber coupling losses of 0.6-1.6 dB/facet. These measurements were performed by an additional cutback measurement.

The 31 mm long glass waveguide and input fiber were aligned first by observing

the output mode on the IR camera placed in the axis of propagation. The FWHMs of the mode were measured to be 11.5 μm in both longitudinal and transversal directions. Then an 8 mm long plasmonic arc sample was aligned with the glass waveguide output by optimizing the output mode imaged at the ending facet. Finally the output fiber was aligned by optimizing the readout of a power-meter. While the standalone plasmonic arc and the glass waveguide feature an insertion loss of ∼12 dB (+/-0.5 dB depending on strip width) and 2.2 dB respectively, the insertion losses measured for the glass plus plasmonic arc couple are ranging between 13-16 dB for TM polarization (see Table IV.11) and 35-37 dB in TE, depending on the plasmonic strip width W_{strip}. It was also checked that the values were the same when the two samples were inverted with respect to the propagation direction.

	PlasArc strip width	5 μm	7.5 μm	10 μm	12.5 μm	15 μm
Insertion Loss in TM (dB)	Standalone PlasArc	12.6	12.6	12.2	11.8	11.5
	Standalone oPCB	2.2				
	oPCB ⟶ PlasArc	16.0	13.6	13.3	13.1	12.8

Table IV.11 – *Coupled oPCB / Plasmonic Arc insertion losses (TM polarization).*

The plasmonic arc to glass waveguide coupling loss $C_{Arc-oPCB}$ was deduced by the following calculation where we define $C_{fiber-Arc}$ and $C_{fiber-oPCB}$ as the fiber coupling losses involved, P_{Arc} and P_{oPCB} as the propagation losses obtained from the cutback studies and L_{Arc} and L_{oPCB} the lengths of the samples. Equation IV.2 gives the total insertion loss of the oPCB-arc assembly:

$$\begin{aligned} Loss &= C_{fiber-Arc}(W_{strip}) + L_{arc}P_{arc}(W_{strip}) + C_{arc-oPCB}(W_{strip}) \\ &\quad + L_{oPCB}P_{oPCB} + C_{fiber-oPCB} \end{aligned} \tag{IV.2}$$

where $L_{oPCB}P_{oPCB}$ = 0.015x31 dB and L_{arc}=8 mm. $C_{fiber-oPCB}$ is deduced from the insertion loss I_{oPCB} = 2.2 dB of the standalone oPCB waveguide and P_{oPCB} by the following equation:

$$C_{fiber-oPCB} = (I_{oPCB} - L_{oPCB}P_{oPCB})/2 \tag{IV.3}$$

The results are presented in Figure IV.44. We observe that the insertion loss tend to decrease as a function of W_{strip}. The 10 μm width seems to be the optimum for the coupling at the interface between the two elements but 12.5 and 15 μm are pretty close and the relatively small difference between the 3 values of W_{strip} could be due to the local variations of the coupling loss $C_{fiber-Arc}$ linked with the quality of the cleaving. The noticeable decreasing trend between 5 and 10 μm is more important and is certainly due to increased mode size mismatch. The coupling loss of 1.7-2.3 dB/interface with the gold strip widths equal to or larger than 10 μm is decent performance for plasmonic arc interconnects.

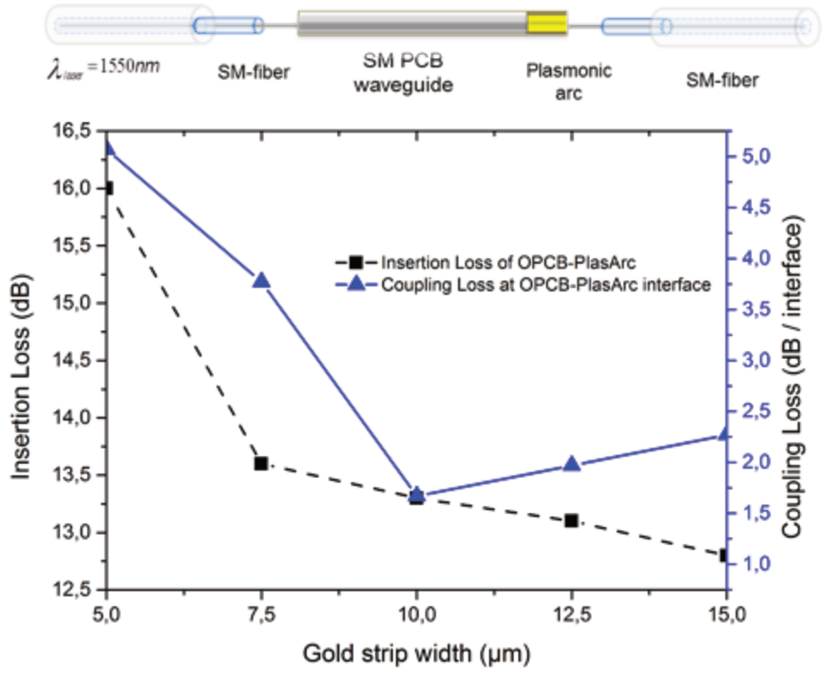

Figure IV.44 *– Optical losses of the oPCB-Plasmonic Arc assembly. The lengths of the oPCB waveguide and plasmonic waveguide are 61 mm and 8 mm, respectively.*

7 Summary and conclusion of Chapter IV

LR-SPPW samples have been fabricated, characterized in an end-fire fiber-to-fiber experiment and the coupling with single-mode glass waveguide (optical PCB) has been studied, for the use of the plasmonic arcs as single-mode interconnects.

LR-SPPW fabrication methods have been developed for 3 different polymers. FOWG polymers suffer from a more complex fabrication procedure than the other polymers, partly because of the need of working under inert atmosphere but also due to the sensitivity of the polymer to some fabrication process steps. This makes its use difficult in practice. Momentive and Lightlink polymers are much handier and were preferred for the production of the LR-SPPW waveguides. Contrary to FOWG, these two polymers are siloxanes. This allowed the use of a silane-thiol molecular bonder which was proved very useful in order to optimize the quality of the waveguide stack.

Both Momentive and LightLink polymers gave LR-SPPWs with similar optical performances, below 1 dB/mm propagation loss, with probably a slightly lower loss for Momentive (dependent on waveguide width). Polymer FOWG did not show the expected performances. Dicing was better than cleaving at reducing end-fire coupling losses, down to about 1 dB per facet. The observed difference in the coupling losses are attributed to differences in the cutting method and not to the polymer itself. By using the best fabrication conditions we think that insertion losses as low as a few dB can be obtained reproducibly.

Silver based LR-SPPW showed a poor polarization ratio which led us to favor gold. Nevertheless a propagation loss of 0.3 to 0.4 dB/cm, which is lower than that

with gold, was found, close to simulation's prediction. A deep study of the conditions of evaporation might be a way of improving the polarization ratio.

LR-SPPW Type	Au Momentive cleaved	Au LightLink cleaved	Au LightLink diced	Ag LightLink diced
Polarization ratio TM/TE (dB)	20—30	10—20	20—30	1—10
Coupling Loss (dB/facet)	2.4—5.5	∼3.8	0.8—1.3	0.6—1.2
Propagation Loss (dB/mm)	0.33—1	∼1	0.95—1.2	0.54—0.9
Propagation Loss exponential fit from decay image (dB/mm)		0.5-0.7	0.26—0.73	∼1

Table IV.12 – *Summary of single-cladding LR-SPPW performances in the straight (horizontal) configuration.*

The coupling of LR-SPPWs with single-mode glass waveguide oPCB allowed us to estimate the coupling loss at the interface ranging between 1.7 and 2.3 dB/interface for waveguide widths between 10 and 15 μm.

General conclusion

In this manuscript, we have reported the fabrication and characterization of long-range plasmonic waveguides at the telecom frequency.

The first studied waveguide type is based on the Ultra-Long-Range Surface-Plasmon-Polariton, which has an asymmetric structure consisting of a stack of metal and polymer, the whole being embedded into a cladding polymer. The optical loss measurements performed on the straight waveguides yielded promising results with average propagation losses of 1 dB/mm. We have designed and fabricated a non-flexible component with an array of ultra-long waveguides integrating an SPP total internal reflection mirror allowing light redirection. The performance of this light-redirecting structure allowing plasmonic interconnection has proved to be worse than expected with respect to the straight waveguides. Nevertheless, this allowed developing a process based on a 60 μm thick deep etching with an angle close to 90^o at the end of etching. In addition, a double lithography process was also developed to homogenize the optical index of the different layers and to obtain a nice vertical wall for the interface constituting the SPP mirror.

The second studied guide type is based on the "Long-Range Surface-Plasmon-Polariton ", having a symmetric structure which at first sight seems simpler but which is in fact more complex to fabricate partly because the withdrawal of the photoresist used to define the metal waveguide is delicate and partly because of the incompatibility of some polymer materials with some of the fabrication steps (lithography; plasma etching). The development of a polymer-based LR-SPP flexible arc waveguide yielded waveguides with moderate loss. The propagation loss of 3.2 dB/mm obtained in the uncorrected FOWG configuration is relatively high. The reason for the losses may be due to imperfect symmetry of the manufactured waveguide. We suspect that during the assembly process of the two claddings, a gap (air) is left between the lower and upper layers, inducing an asymmetry in proximity of the gold strip that is detrimental to the propagation length of the plasmon mode.

We also used Momentive and LightLink materials as cladding materials for LRSPP (plasmonic arc) flexible waveguides with gold as the plasmonic metal. Both materials yielded plasmonic arcs with optical performance similar to the telecom frequency, with propagation loss most often less than 1 dB/mm in TM polarization. Performance is slightly better for Momentive materials with a minimum of $\sim$0.3 dB/mm for a 10 μm gold bandwidth. The coupling losses reached about 1 dB/facet. In the self-supporting S-curve configuration, the loss of curvature of the plasmonic arc was 2.2-2.8 dB/90^o at a radius of curvature of 2.5 mm. The coupling of oPCB and plasmonic arc has shown an optimum width at 10 μm to minimize the interface loss between these elements. We have therefore developed a manufacturing process based on gold etching and the use of a covalent surface modification of gold to promote adhesion to the polymer, a condition

which is necessary to ensure a good propagation length.

These promising results paves the way towards the integration of plasmonic arcs as interconnectors in more advanced devices. The next step in the future developments would be to study their performance when in real modulator frequencies conditions. For future research, it would also be interesting to use other metals frequently used in plasmon technology. Aluminum seems to be a potential candidate for this type of application. However, the optical index homogenization aspects of the cladding polymers must be improved and better understood to result in lower losses.

Appendices

Appendix A

Mode profile

To find the best configuration with the lowest propagation loss a structure of two 30 μm-thick polymer claddings and a width of 100 μm with a gold waveguide placed in the middle of the structure. Three gold thickness has been chosen for a great interest to find the lowest propagation loss a structure but realistic by experimental deposition. These thicknesses are 10, 15 and 20 nm.

1 for FOWG-115-LR-SPP waveguide

The three modes are been calculated with a polymer index : $n_{FOWG-115}(\lambda_{TC}) = 1.506 + i\,0$ and gold complex refractive index of $n_{Au}(\lambda_{TC}) = 0.52 + i\ 10.81$

Gold thickness (nm)	$\Re e(n_{eff})$	$\Im m(n_{eff})$	Propagation length (mm)	FWHM longitudinal (μm)	FWHM transversal (μm)	Mode profile
10	1.5060	$5.77 \cdot 10^{-7}$	213.8	9	9	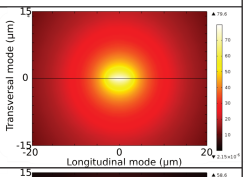
15	1.5062	$5.84 \cdot 10^{-6}$	21.1	7	6	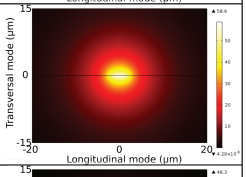
20	1.5067	$2.23 \cdot 10^{-5}$	5.5	6	4	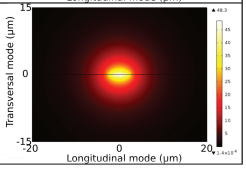

Table A.1 *– Mode profile for FOWG-115-LR-SPP waveguide of with 5 μm of width for different thickness of gold strip*

2 for FOWG-116-LR-SPP waveguide

The three modes are been calculated with a polymer index : $n_{FOWG-116}(\lambda_{TC}) = 1.547 + i\,0$ and gold complex refractive index of $n_{Au}(\lambda_{TC}) = 0.52 + i\ 10.81$

Gold thickness (nm)	$\Re e(n_{eff})$	$\Im m(n_{eff})$	Propagation length (mm)	FWHM longitudinal (μm)	FWHM transversal (μm)	Mode profile
10	1.5062	$2.66 \cdot 10^{-6}$	46.4	11	8	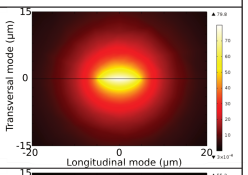
15	1.5068	$1.26 \cdot 10^{-5}$	9.8	10	5	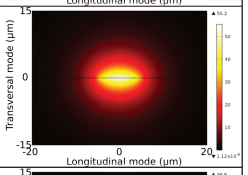
20	1.5076	$3.54 \cdot 10^{-5}$	3.5	9	4	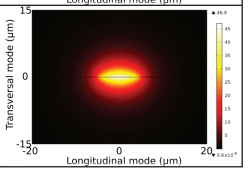

Table A.2 *– Mode profile for FOWG-115-LR-SPP waveguide of with 10 μm of width for different thickness of gold strip*

Gold thickness (nm)	$\Re e(n_{eff})$	$\Im m(n_{eff})$	Propagation length (mm)	FWHM longitudinal (μm)	FWHM transversal (μm)	Mode profile
10	1.5064	$3.67 \cdot 10^{-6}$	33.6	15	8	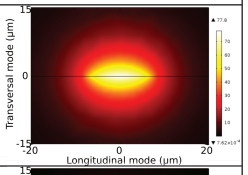
15	1.5071	$1.46 \cdot 10^{-5}$	8.4	14	5	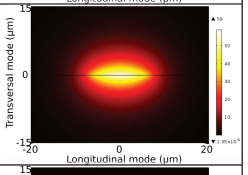
20	1.5080	$3.85 \cdot 10^{-5}$	3.2	13	4	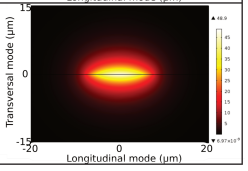

Table A.3 *– Mode profile for FOWG-115-LR-SPP waveguide of with 15 μm of width for different thickness of gold strip*

Gold thickness (nm)	$\Re e(n_{eff})$	$\Im m(n_{eff})$	Propagation length (mm)	FWHM longitudinal (μm)	FWHM transversal (μm)	Mode profile
10	1.5470	$7.54 \cdot 10^{-7}$	163.7	9	8	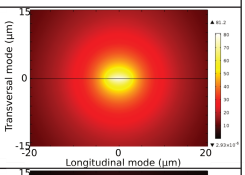
15	1.5473	$7.17 \cdot 10^{-6}$	17.2	7	5	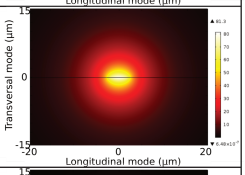
20	1.5478	$2.60 \cdot 10^{-5}$	4.7	5	4	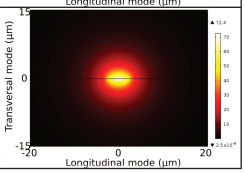

Table A.4 *– Mode profile for FOWG-116-LR-SPP waveguide of with 5 μm of width for different thickness of gold strip*

Gold thickness (nm)	$\Re e(n_{eff})$	$\Im m(n_{eff})$	Propagation length (mm)	FWHM longitudinal (μm)	FWHM transversal (μm)	Mode profile
10	1.5473	$3.15 \cdot 10^{-6}$	39.1	11	8	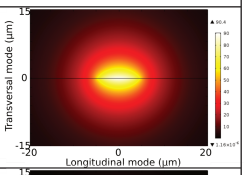
15	1.5479	$1.43 \cdot 10^{-5}$	8.6	10	5	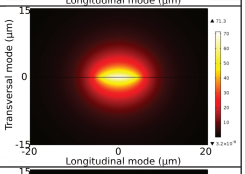
20	1.5488	$3.95 \cdot 10^{-5}$	3.1	10	4	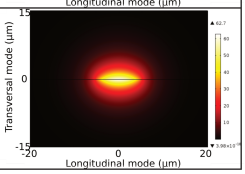

Table A.5 *– Mode profile for FOWG-116-LR-SPP waveguide of with 10 μm of width for different thickness of gold strip*

Gold thickness (nm)	$\Re e(n_{eff})$	$\Im m(n_{eff})$	Propagation length (mm)	FWHM longitudinal (μm)	FWHM transversal (μm)	Mode profile
10	1.5474	$4.20 \cdot 10^{-6}$	29.4	15	7	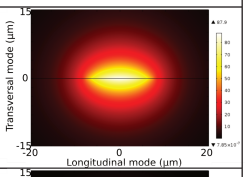
15	1.5482	$1.63 \cdot 10^{-5}$	7.6	13	5	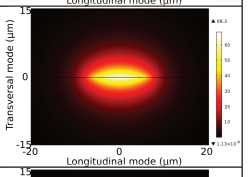
20	1.5492	$4.25 \cdot 10^{-5}$	2.9	13	4	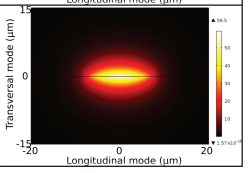

Table A.6 *– Mode profile for FOWG-116-LR-SPP waveguide of with 15 μm of width for different thickness of gold strip*

Bibliography

[1] ChemOptics Inc, 2010. Daejeon, Republic of Korea.

[2] FP7-ICT. Phoxtrot project : Photonics for high-performance, low-cost and low-energy data centers and high performance computing systems: Terabit/s optical interconnect technologies for on-board, board-to-board and rack- to-rack data links, Oct. 2012-2016.

[3] Rashid Zia, Jon A. Schuller, Anu Chandran, and Mark L. Brongersma. Plasmonics: the next chip-scale technology. *Materials Today*, 9(7-8):20–27, 2006.

[4] Corrado Sciancalepore, Karim Hassan, Thomas Ferrotti, Julie Harduin, Hélène Duprez, Sylvie Menezo, and Badhise Ben Bakir. Low-loss adiabatically-tapered high-contrast gratings for slow-wave modulators on soi. In *Photonic West*, volume 9372, page 93720G, February 2015.

[5] Wei Bing Lu, Wei Zhu, Hong Ju Xu, Zhen Hua Ni, Zheng Gao Dong, and Tie Jun Cui. Flexible transformation plasmonics using graphene. *Optics express*, 21(9):10475–82, 2013.

[6] Jin Tae Kim, Jaehyeon Kim, Hongkyw Choi, Choon-Gi Choi, and Sung-Yool Choi. Graphene-based photonic devices for soft hybrid optoelectronic systems. *Nanotechnology*, 23(34):344005, August 2012.

[7] Alexandra Boltasseva and Harry A. Atwater. Low-loss plasmonic metamaterials. *Science*, 331(6015):290–291, jan 2011.

[8] Steffen Uhlig. *Micro-Processing Applied to Optical Interconnects and High-Frequency Packaging*. PhD thesis, Linköping University, Sweden, 2006.

[9] N. Lindenmann, G. Balthasar, D. Hillerkuss, R. Schmogrow, M. Jordan, J. Leuthold, W. Freude, and C. Koos. Photonic wire bonding: a novel concept for chip-scale interconnects. *Optics Express*, 20(16):17667, 2012.

[10] Aloyse Degiron, Pierre Berini, and David R. Smith. Guiding light with long-range plasmons. *Optics and Photonics News*, 19(7):28, jul 2008.

[11] Heinz Raether. *Surface Plasmons on Smooth and Rough Surfaces and on Gratings*, volume 111 of *Springer Tracts in Modern Physics*. Springer Berlin Heidelberg, 1988.

[12] William L Barnes, Alain Dereux, and Thomas W Ebbesen. Surface plasmon subwavelength optics. *Nature*, 424(6950):824–830, 2003.

[13] Anatoly V. Zayats and Igor I. Smolyaninov. Near-field photonics: surface plasmon polaritons and localized surface plasmons. *Journal of Optics A: Pure and Applied Optics*, 5(4):S16–S50, 2003.

[14] Anatoly V. Zayats, Igor I. Smolyaninov, and Alexei A. Maradudin. Nano-optics of surface plasmon polaritons. *Physics Reports*, 408(3-4):131–314, 2005.

[15] Stefan A. Maier and Harry A. Atwater. Plasmonics: Localization and guiding of electromagnetic energy in metal/dielectric structures. *Journal of Applied Physics*, 98(1):1–10, 2005.

[16] Ruoxi Yang and Zhaolin Lu. Subwavelength plasmonic waveguides and plasmonic materials. *International Journal of Optics*, 2012, 2012.

[17] Zhanghua Han and Sergey I Bozhevolnyi. Radiation guiding with surface plasmon polaritons. *Reports on progress in physics. Physical Society (Great Britain)*, 76(1):016402, 2013.

[18] Suntak Park, Jung Jin Ju, Jin Tae Kim, Min-Su Kim, Seung Koo Park, Jong-Moo Lee, Wook-Jae Lee, and Myung-Hyun Lee. Sub-db/cm propagation loss in silver stripe waveguides. *Optics express*, 17(2):697–702, jan 2009.

[19] Sergey I. Bozhevolnyi, Thomas Nikolajsen, and Kristjan Leosson. Integrated power monitor for long-range surface plasmon polaritons. *Optics Communications*, 255(1-3):51–56, 2005.

[20] Thomas Nikolajsen, Kristjan Leosson, and Sergey I. Bozhevolnyi. In-line extinction modulator based on long-range surface plasmon polaritons. *Optics Communications*, 244(1-6):455–459, January 2005.

[21] Jaime Cardenas, Lixia Li, Seunghyun Kim, and Gregory P. Nordin. Compact low loss single air interface bends in polymer waveguides. *Optics Express*, 12(22):5314, 2004.

[22] Claudio Dellagiacoma, Theo Lasser, Olivier J. F. Martin, Aloyse Degiron, Jack J. Mock, and David R. Smith. Simulation of complex plasmonic circuits including bends. *Optics Express*, 19(20):18979, sep 2011.

[23] Jeroen Missinne, Sandeep Kalathimekkad, Bram Van Hoe, Erwin Bosman, Jan Vanfleteren, and Geert Van Steenberge. Stretchable optical waveguides. *Optics Express*, 22(4):4168, feb 2014.

[24] Ioannis Papakonstantinou, Kai Wang, David R. Selviah, and F. Aníbal Fernández. Transition, radiation and propagation loss in polymer multimode waveguide bends. *Optics Express*, 15(2):669, jan 2007.

[25] Dou Xinyuan, Xiaolong Wang, Xiaohui Lin, Duo Ding, David Pan, and Ray Chen. Highly flexible polymeric optical waveguide for out-of-plane optical interconnects. *Optics Express*, 18(15):16227, jul 2010.

[26] Paul Drude. Zur elektronentheorie der metalle. *Annalen der Physik*, 306(3):566–613, 1900.

[27] E. N. Economou. Surface plasmons in thin films. *Phys. Rev.*, 182:539–554, Jun 1969.

[28] Lucas Novotny and Bert Hecht. *Principles of Nano-Optics*. Press, Cambridge University, Cambridge, second edition, 2006.

[29] J. R. Sambles, G. W. Bradbery, and Fuzi Yang. Optical excitation of surface plasmons: An introduction. *Contemporary Physics*, 32(3):173–183, may 1991.

[30] Laszlo Solymar and Ekaterina Shamonina. *Waves in Metamaterials*. Oxford University Press, Oxford, 2009.

[31] Andreas Otto. Excitation of nonradiative surface plasma waves in silver by the method of frustrated total reflection. *Zeitschrift für Physik*, 216(4):398–410, aug 1968.

[32] J Schoenwald, E Burstein, and J.M. Elson. Propagation of surface polaritons over macroscopic distances at optical frequencies. *Solid State Communications*, 12(3):185–189, feb 1973.

[33] S Glasberg, A Sharon, D Rosenblatt, and A A Friesem. Long-range surface plasmon resonances in grating-waveguide structures. *Applied Physics Letters*, 70(10):1210, 1997.

[34] Pierre Berini. Plasmon polariton modes guided by a metal film of finite width. *Optics Letters*, 24(15):1011, aug 1999.

[35] Rashid Zia, Jon A. Schuller, and Mark L. Brongersma. Near-field characterization of guided polariton propagation and cutoff in surface plasmon waveguides. *Physical Review B - Condensed Matter and Materials Physics*, 74(16):1–12, 2006.

[36] Pierre Berini. Plasmon-polariton waves guided by thin lossy metal films of finite width: Bound modes of symmetric structures. *Physical Review B*, 61(15):10484–10503, apr 2000.

[37] Junghyun Park, Kyoung-Youm Kim, Il-Min Lee, Hyunmin Na, Seung-Yeol Lee, and Byoungho Lee. Trapping light in plasmonic waveguides. *Optics Express*, 18(2):598, jan 2010.

[38] E. Kretschmann and H. Raether. Notizen: Radiative Decay of Non Radiative Surface Plasmons Excited by Light. *Zeitschrift für Naturforschung A*, 23(12):2135–2136, jan 1968.

[39] Jonathan J. Foley IV, Hayk Harutyunyan, Daniel Rosenmann, Ralu Divan, Gary P. Wiederrecht, and Stephen K. Gray. When are Surface Plasmon Polaritons Excited in the Kretschmann-Raether Configuration? *Scientific Reports*, 5:9929, apr 2015.

[40] Sergey I. Bozhevolnyi. *Plasmonic: Nanoguides and Circuits*. Distributed by World Scientific Pub, 2009.

[41] Ronen Adato and Junpeng Guo. Characteristics of ultra-long range surface plasmon waves at optical frequencies. *Optics express*, 15(8):5008–17, apr 2007.

[42] Ronen Adato and Junpeng Guo. Novel metal-dielectric structures for guiding ultra-long range surface plasmon-polaritons at optical frequencies. In Mark I. Stockman, editor, *Proceedings of SPIE*, volume 6641, pages 66410G–66410G–8, sep 2007.

[43] Junpeng Guo and Ronen Adato. Extended long range plasmon waves in finite thickness metal film and layered dielectric materials. *Optics express*, 14(25):12409–18, dec 2006.

[44] Charles G. Durfee, Thomas E. Furtak, Reuben T. Collins, and Russell E. Hollingsworth. Metal-oxide-semiconductor-compatible ultra-long-range surface plasmon modes. *Journal of Applied Physics*, 103(11):113106, 2008.

[45] MG Saber, RH Sagor, and AA Noor. Analysis of propagation loss of highly confined spp mode in mim waveguide with additional thin metallic film. *International Journal of Computer Applications*, 65(2):41–45, 2013.

[46] Pierre Berini. Plasmon-polariton waves guided by thin lossy metal films of finite width: Bound modes of asymmetric structures. *Physical Review B*, 63(12):125417, mar 2001.

[47] Jean-claude Weeber, Joachim R. Krenn, Alain Dereux, B. Lamprecht, Yvon Lacroute, and Jean-Pierre Goudonnet. Near-field observation of surface plasmon polariton propagation on thin metal stripes. *Physical Review B*, 64(4):045411, jul 2001.

[48] Jacek Gosciniak and Sergey I Bozhevolnyi. Performance of thermo-optic components based on dielectric-loaded surface plasmon polariton waveguides. *Scientific Reports*, 3:1803, may 2013.

[49] A. V. Krasavin and A. V. Zayats. Electro-optic switching element for dielectric-loaded surface plasmon polariton waveguides. *Applied Physics Letters*, 97(4):041107, 2010.

[50] Martti Kauranen and Anatoly V. Zayats. Nonlinear plasmonics. *Nature Photonics*, 6(11):737–748, nov 2012.

[51] Tobias Holmgaard, Jacek Gosciniak, and Sergey I Bozhevolnyi. Long-range dielectric-loaded surface plasmon-polariton waveguides. *Optics Express*, 18(22):23009, oct 2010.

[52] Karim Hassan. *Fabrication and characterization of Thermo-Plasmonic routers for Telecom Applications*. PhD thesis, Université de Bourgogne, 2013.

[53] Karim Hassan, Jean-Claude Weeber, Laurent Markey, Alain Dereux, A. Pitilakis, O. Tsilipakos, and E. E. Kriezis. Thermo-optic plasmo-photonic mode interference switches based on dielectric loaded waveguides. *Applied Physics Letters*, 99(24):1–4, 2011.

[54] Jong-Moo Lee, Suntak Park, Min-su Kim, Seung Koo Park, Jin Tae Kim, Joong-Seon Choe, Wook-Jae Lee, Myung-Hyun Lee, and Jung Jin Ju. Low bending loss metal waveguide embedded in a free-standing multilayered polymer film. *Optics express*, 17(1):228–34, January 2009.

[55] Jin Tae Kim, Suntak Park, Jung Jin Ju, Sangjun Lee, and Sangin Kim. Low bending loss characteristics of hybrid plasmonic waveguide for flexible optical interconnect. *Optics express*, 18(23):24213–20, November 2010.

[56] Jin Tae Kim, Jung Jin Ju, Suntak Park, Min-su Kim, Seung Koo Park, and Sang-Yung Shin. Hybrid plasmonic waveguide for low-loss lightwave guiding. *Opt. Express*, 18(3):2808–2813, Feb 2010.

[57] Ilya Slovinsky, Gudmundur K. Stefansson, Anna Kossoy, and Kristjan Leosson. Propagation loss of long-range surface plasmon polariton gold stripe waveguides in the thin-film limit. *Plasmonics*, 8(4):1613–1619, June 2013.

[58] Thomas Nikolajsen, Kristjan Leosson, Ildar Salakhutdinov, and Sergey I. Bozhevolnyi. Polymer-based surface-plasmon-polariton stripe waveguides at telecommunication wavelengths. *Applied Physics Letters*, 82(5):668, 2003.

[59] Shankar Kumar Selvaraja and Purnima Sethi. Review on optical waveguides. In Kok Yeow You, editor, *Emerging Waveguide Technology*, chapter 6. IntechOpen, 2018.

[60] Robert G Hunsperger. Waveguide loss - bend loss. *Integrated Optics*, 22:84–87, 2009.

[61] Peter Bienstman, E. Six, M. Roelens, M. Vanwolleghem, and Roel Baets. Calculation of bending losses in dielectric waveguides using eigenmode expansion and perfectly matched layers. *IEEE Photonics Technology Letters*, 14(2):164–166, 2002.

[62] B.S. Bae, W.S. Kim, and K.B. Yoon. Fabrication of zero bending loss flexible film optical waveguide by uv moulding of sol-gel hybrid materials. *Integrated Photonics Research and Applications*, pages 60–62, 2005.

[63] Pierre Berini and Junjie Lu. Curved long-range surface plasmon-polariton waveguides. *Optics express*, 14:2365–2371, 2006.

[64] Denis Lauvernier, S Garidel, M Zegaoui, Jean-Pierre Vilcot, J Harari, V Magnin, and Didier Decoster. Optical devices for ultra-compact photonic integrated circuits based on iii-v/polymer nanowires. *Optics express*, 15(9):5333–41, April 2007.

[65] Sangjun Lee, Sangin Kim, and Hanjo Lim. Improved bending loss characteristics of asymmetric surface plasmonic waveguides for flexible optical wiring. *Optics express*, 17(22):19435–43, October 2009.

[66] Wenhui Wang, Qing Yang, Fengru Fan, Hongxing Xu, and Zhong Lin Wang. Light propagation in curved silver nanowire plasmonic waveguides. *Nano letters*, 11(4):1603–8, April 2011.

[67] Tie Jun Cui and Xiaopeng Shen. Thz and microwave surface plasmon polaritons on ultrathin corrugated metallic strips. *Terahertz Science and Technology*, 6(2):147–164, 2013.

[68] Nikolaos Bamiedakis, Richard V. Penty, and Ian H. White. Compact multimode polymer waveguide bends for board-level optical interconnects. *Journal of Lightwave Technology*, 31(14):2370–2375, 2013.

[69] Pierre Berini. Long-range surface plasmon polaritons. *Advances in Optics and Photonics*, 1(3):484, sep 2009.

[70] Victoria Astley, Julianna Scheiman, Rajind Mendis, and Daniel M. Mittleman. Bending and coupling losses in terahertz wire waveguides. *Optics Letters*, 35(4):553–555, feb 2010.

[71] William L Barnes. Surface plasmon–polariton length scales: a route to subwavelength optics. *Journal of Optics A: Pure and Applied Optics*, 8:S87–S93, 2006.

[72] Tobias Holmgaard and Sergey I. Bozhevolnyi. Theoretical analysis of dielectric-loaded surface plasmon-polariton waveguides. *Physical Review B - Condensed Matter and Materials Physics*, 75(24):1–12, 2007.

[73] Masashi Eguchi. Multilayered effective-index analysis of dielectric waveguides with complicated microstructures. *Journal of the Optical Society of America B*, 28(10):2478, 2011.

[74] Olek C. Zienkiewicz, Robert L. Taylor, and J.Z. Zhu. *The Finite Element Method: Its Basis and Fundamentals*. Elsevier Science, 6th edition, 2005.

[75] O. S. Wolfbeis and Jiří Homola. *Surface Plasmon Resonance Based Sensors*, volume 4 of *Springer Series on Chemical Sensors and Biosensors*. Springer Berlin Heidelberg, Berlin, Heidelberg, 2006.

[76] Y. Enami, D. Mathine, C. T. DeRose, R. a. Norwood, J. Luo, A. K-Y. Jen, and N. Peyghambarian. Hybrid electro-optic polymer/sol-gel waveguide directional coupler switches. *Applied Physics Letters*, 94(21):213513, 2009.

[77] Sergey I. Bozhevolnyi, Valentyn S Volkov, Kristjan Leosson, and Alexandra Boltasseva. Surface plasmon polariton waveguiding in random surface nanostructures. *Journal of microscopy*, 209(Pt 3):209–13, mar 2003.

[78] Shih-Hsiang Hsu, Chih-Yuan Tsou, Chih-Ming Wang, and Sheng-Chieh Tseng. 10 gb/s optical interconnection on flexible optical waveguide in electronic printed circuit board. *Optics and Photonics Journal*, 03(02):252–255, 2013.

[79] Albert Borreman, Sami Musa, A A M Kok, Mart B J Diemeer, and Alfred Driessen. Fabrication of polymeric multimode waveguides and devices in su-8 photoresist using selective polymerization. In Taco Schouten, D. Visser F., Daan Lenstra, and Hugo, editors, *Proceedings Symposium IEEE/LEOS*, pages 83–86, Amsterdam, the Netherlands, 2002. Vrije Universiteit Amsterdam.

[80] J. Liu, B. Cai, J. Zhu, G. Ding, X. Zhao, C. Yang, and D. Chen. Process research of high aspect ratio microstructure using SU-8 resist. *Microsystem Technologies*, 10(4):265–268, May 2004.

[81] Sheng Ting Huang, Chien Chih Lai, Fang Wen Sheu, and Wan Shao Tsai. Characterization of long-range plasmonic waveguides at visible to near-infrared regime. *AIP Advances*, 7(12), 2017.

[82] Bruce L. Booth, Joseph E. Marchegiano, Catherine T. Chang, Robert J. Furmanak, Douglas M. Graham, and Richard G. Wagner. Polyguide polymeric technology for optical interconnect circuits and components. In Ray T. Chen and Peter S. Guilfoyle, editors, *Proceedings of SPIE*, volume 3005, pages 238–251, apr 1997.

[83] W. H. Wong, J. Zhou, and E. Y. B. Pun. Low-loss polymeric optical waveguides using electron-beam direct writing. *Applied Physics Letters*, 78(15):2110–2112, apr 2001.

[84] H. Ma, A.K.-Y. Jen, and L.R. Dalton. Polymer-Based Optical Waveguides: Materials, Processing, and Devices. *Advanced Materials*, 14(19):1339–1365, oct 2002.

[85] R Buestrich, F Kahlenberg, M Popall, P Dannberg, R Müller-Fiedler, and O Rösch. ORMOCER®s for Optical Interconnection Technology. *Journal of Sol-Gel Science and Technology*, 20(2):181–186, 2001.

[86] Muhammad Umar Khan, John Justice, Jarno Petäjä, Tia Korhonen, Arjen Boersma, Sjoukje Wiegersma, Mikko Karppinen, and Brian Corbett. Multi-level single mode 2D polymer waveguide optical interconnects using nano-imprint lithography. *Optics Express*, 23(11):14630, jun 2015.

[87] Ahmed Elmogi, Erwin Bosman, Jeroen Missinne, and Geert Van Steenberge. Comparison of epoxy- and siloxane-based single-mode optical waveguides defined by direct-write lithography. *Optical Materials*, 52:26–31, feb 2016.

[88] Jin Tae Kim, Suntak Park, Jung Jin Ju, Seung Koo Park, Min-Su Kim, and Myung-Hyun Lee. Low-Loss Polymer-Based Long-Range Surface Plasmon-Polariton Waveguide. *IEEE Photonics Technology Letters*, 19(18):1374–1376, sep 2007.

[89] Suntak Park, Min-Su Kim, Jin Tae Kim, Seung Koo Park, Jung Jin Ju, and Myung-Hyun Lee. Long range surface plasmon polariton waveguides at 1.31 and 1.55 μm wavelengths. *Optics Communications*, 281(8):2057–2061, apr 2008.

[90] Maziar P. Nezhad, Steve Zamek, Lin Pang, and Yeshaiahu Fainman. Fabrication approaches for metallo-dielectric plasmonic waveguides. In Thomas J. Suleski, Winston V. Schoenfeld, and Jian J. Wang, editors, *Advanced Fabrication Technologies for Micro/Nano Optics and Photonics*, volume 6883, pages 68830S–68830S–9, feb 2008.

[91] Irving Skeist and Jerry (auth.) Miron. *Handbook of Adhesives*. Springer US, Boston, MA, 3 edition, 1990.

[92] Christian Vernoux, Yiting Chen, Laurent Markey, Cosmin Spârchez, Juan Arocas, Thorsten Felder, Marcel Neitz, Lars Brusberg, Jean-Claude Weeber, Sergey I. Bozhevolnyi, and Alain Dereux. Flexible long-range surface plasmon polariton single-mode waveguide for optical interconnects. *Optical Materials Express*, 8(2):469 – 484, 2018.

[93] Jin Tae Kim, Suntak Park, Seung Goo Park, Min su Kim, Myung-Hyun Lee, and Jung Jin Ju. Gold stripe optical waveguides fabricated by a novel double-layered liftoff process. *ETRI Journal*, 31:778–783, 2009.

[94] Milind S. Kulkarni and Henry F. Erk. Acid-based etching of silicon wafers: Mass-transfer and kinetic effects. *Journal of The Electrochemical Society*, 147(1):176–188, 2000.

[95] W.T Li, R.B Charters, B Luther-Davies, and L Mar. Significant improvement of adhesion between gold thin films and a polymer. *Applied Surface Science*, 233(1-4):227–233, June 2004.

[96] P. Slepička, N. Slepčková Kasálková, E. Stránská, L. Bačáková, and V. Švorčík. Surface characterization of plasma treated polymers for applications as biocompatible carriers. *Express Polymer Letters*, 7(6):535–545, apr 2013.

[97] D M Svirachev and N a Tabaliov. Plasma Treatment of Polymer Surfaces in Different Gases. *Bulgarian Journal of Physics*, 32:22–33, 2005.

[98] Robert G Hunsperger. *Integrated Optics : Theory and Technology*. Springer-Verlag New York, New-York, sixth edition, 2009.

[99] Lars Brusberg, Henning Schroder, Marco Queisser, and Klaus-Dieter Lang. Single-mode glass waveguide platform for DWDM chip-to-chip interconnects. In *2012 IEEE 62nd Electronic Components and Technology Conference*, pages 1532–1539. IEEE, may 2012.

[100] Lars Brusberg, Marcel Neitz, and Henning Schröder. Single-mode glass waveguide technology for optical interchip communication on board level. In Alexei L. Glebov and Ray T. Chen, editors, *Proc. SPIE 8267, Optoelectronic Interconnects XII*, volume 8267, page 82670M, feb 2012.

Publications associated with this work

Conference Talk

1. Y. Chen, L. Markey, C. Vernoux, A. Dereux, S. I. Bozhevolnyi, "Characterization of a low-loss flexible long-range surface-plasmon-polariton waveguide," in *Danish Optical Society Annual Meeting (**DOPS**)*, Odense (Denmark), November 19^{th}-$20th$ 2015

Journal Publication

1. C. Vernoux, Y. Chen, L. Markey, C. Spârchez, J. Arocas, T. Felder, M. Neitz, L. Brusberg, J.C. Weeber, S. I. Bozhevolnyi, A. Dereux,"Flexible long-range surface plasmon polariton single-mode waveguide for optical interconnects," Opt. Mater. Express **8**(2), 469-484 (2018)

Conference Posters

1. C.Vernoux, L. Markey, Y. Chen, S. Bozhevolnyi, T. Felder, A. Dereux, "Flexible Long-range plasmonic waveguide for optical interconnect application" in *7th International Conference on Surface Plasmon Photonics (**SPP7**)* - Jerusalem (Israel), May, $31st$-June 5^{th} 2015

2. C.Vernoux, L. Markey, Y. Chen, S. Bozhevolnyi, T. Felder, A. Dereux, "Flexible Long-range plasmonic waveguide for optical interconnect" during the *PhD days, Carnot **PhD School***, Dijon(France), May 21^{st}-22^{nd} 2015

3. C.Vernoux, L. Markey, J.C. Weeber, A. Dereux, "Long-range plasmonic waveguide for Tb/s optical interconnect application" during the *PhD days, Carnot **PhD School***, Dijon (France), May 30^{th}-31^{st} 2013

Résumé : Les guides d'ondes plasmoniques à longue distance (LR-SPP) sont récemment apparus comme une des solutions possibles pour le transport de signaux optiques entre puce au sein de « l'ordinateur optique », au sein duquel les signaux électriques seraient remplacés par des signaux lumineux. Cette thèse traite plus précisément le cas de l'interconnexion optique entre composants électroniques nécessitant une redirection de l'information à angle quelconque, afin de remplacer les interconnections électroniques actuelles très consommatrices en énergie et génératrices de chaleur par des guides d'ondes composés de polymères qui se trouve être très peu énergivores. Au travers d'un chapitre de simulation numérique, nous déterminerons les caractéristiques dimensionnelles afin de minimiser les pertes d'énergies par propagations de nos guides d'ondes. Par la suite, nous démontrons la faisabilité expérimentale des résultats obtenus dans la partie théorique au sein de deux types de structures, une première structure d'un seul bloc solide où l'onde d'information est réfléchie sur un prisme d'air, et une seconde structure basée sur une interconnexion flexible où l'information circule le longue d'un guide souple. Les mesures des composants sont effectuées grâce à un montage fibre-à-fibre créé spécialement pour observer les pertes par propagation de nos structures dans la gamme d'ondes des signaux télécoms.
Mots clés : plasmonique, polymere, metal, guide d'onde.

Resume : Long-range Plasmonic Waveguides (LR-SPP) have recently emerged as one of the possible solutions for optical signal transport between chips within the "optical computer", in which electrical signals would be replaced by light signals. More specifically, this thesis deals with the case of optical interconnection between electronic components requiring a redirection of the information at any angle, in order to replace the current electronic interconnections that consume a lot of energy and generate heat through polymer-composed waveguides. This was found to be very energy efficient. Through a numerical simulation chapter, we will determine the dimensional characteristics needed to minimize the energy losses by propagation of our waveguides. Subsequently, we demonstrate the experimental feasibility of the results obtained in the theoretical part in two types of structures. Firstly, a solid one-piece structure, where the information wave is reflected on an air prism will be described, and secondly, a structure based on a flexible interconnection where information flows along a flexible guide. The measurements of the components are done through a fiber-to-fiber arrangement created specifically to observe the propagation losses of our structures in the waveband of telecom signals.
Keywords : plasmonic, polymer, metal, waveguide.